# Localization of Gamma-Ray Bursts Using the Fermi Gamma-Ray Burst Monitor

— Source link ↗

Valerie Connaughton, Michael S. Briggs, Adam Goldstein, Charles A. Meegan ...+24 more authors

**Institutions:** University of Alabama in Huntsville, Marshall Space Flight Center, Universities Space Research Association, Jacobs Engineering Group ...+5 more institutions

**Topics:** Gamma-ray burst and Fermi Gamma-ray Space Telescope

Related papers:

- THE fermi gamma-ray burst monitor

- Gravitational Waves and Gamma-Rays from a Binary Neutron Star Merger: GW170817 and GRB 170817A

- BATSE observations of gamma-ray burst spectra. I: Spectral diversity

- The Fermi GBM Gamma-Ray Burst Spectral Catalog: Four Years of Data

- The burst alert telescope (BAT) on the Swift MIDEX mission

Share this paper: 🅕 🐦 in ✉

# UvA-DARE (Digital Academic Repository)

## Localization of Gamma-Ray Bursts Using the Fermi Gamma-Ray Burst Monitor

Connaughton, V.; Briggs, M.S.; Goldstein, A.; Meegan, C.A.; Paciesas, W.S.; Preece, R.D.; Wilson-Hodge, C.A.; Gibby, M.H.; Greiner, J.; Gruber, D.; Jenke, P.; Kippen, R.M.; Pelassa, V.; Xiong, S.; Yu, H-F.; Bhat, P.N.; Burgess, J.M.; Byrne, D.; Fitzpatrick, G.; Foley, S.; Giles, M.M.; Guiriec, S.; van der Horst, A.J.; von Kienlin, A.; McBreen, S.; McGlynn, S.; Tierney, D.; Zhang, B..B.

[Link to publication](Link to publication)

# LOCALIZATION OF GAMMA-RAY BURSTS USING THE *FERMI* GAMMA-RAY BURST MONITOR

V. Connaughton[1], M. S. Briggs[1], A. Goldstein[2], C. A. Meegan[3], W. S. Paciesas[4], R. D. Preece[5], C. A. Wilson-Hodge[2], M. H. Gibby[6], J. Greiner[7], D. Gruber[8], P. Jenke[3], R. M. Kippen[9], V. Pelassa[3], S. Xiong[3], H.-F. Yu[7,10], P. N. Bhat[3], J. M. Burgess[1], D. Byrne[11], G. Fitzpatrick[11], S. Foley[11], M. M. Giles[6], S. Guiriec[12], A. J. van der Horst[13], A. von Kienlin[7], S. McBreen[11], S. McGlynn[11], D. Tierney[11], and B.-B. Zhang[3]

[1] CSPAR and Physics Department, University of Alabama in Huntsville, 320 Sparkman Drive, Huntsville, AL 35899, USA; valerie@nasa.gov
[2] Astrophysics Office, ZP12, NASA/Marshall Space Flight Center, Huntsville, AL 35812, USA
[3] CSPAR, University of Alabama in Huntsville, 320 Sparkman Drive, Huntsville, AL 35899, USA
[4] Universities Space Research Association, Huntsville, AL, USA
[5] Department of Space Science, University of Alabama in Huntsville, 320 Sparkman Drive, Huntsville, AL 35899, USA
[6] Jacobs Technology, Inc., Huntsville, AL, USA
[7] Max-Planck-Institut für extraterrestrische Physik, Giessenbachstrasse 1, D-85748 Garching, Germany
[8] Planetarium Südtirol, Gummer 5, I-39053 Karneid, Italy
[9] Los Alamos National Laboratory, NM 87545, USA
[10] Excellence Cluster Universe, Technische Universität München, Boltzmannstrasse 2, D-85748 Garching, Germany
[11] School of Physics, University College Dublin, Belfield, Stillorgan Road, Dublin 4, Ireland
[12] NASA Goddard Space Flight Center, Greenbelt, MD 20771, USA
[13] Astronomical Institute, University of Amsterdam, Science Park 904, 1098 XH Amsterdam, The Netherlands

## ABSTRACT

The *Fermi* Gamma-ray Burst Monitor (GBM) has detected over 1400 gamma-ray bursts (GRBs) since it began science operations in 2008 July. We use a subset of over 300 GRBs localized by instruments such as *Swift*, the *Fermi* Large Area Telescope, *INTEGRAL*, and MAXI, or through triangulations from the InterPlanetary Network, to analyze the accuracy of GBM GRB localizations. We find that the reported statistical uncertainties on GBM localizations, which can be as small as $1°$, underestimate the distance of the GBM positions to the true GRB locations and we attribute this to systematic uncertainties. The distribution of systematic uncertainties is well represented (68% confidence level) by a $3°.7$ Gaussian with a non-Gaussian tail that contains about 10% of GBM-detected GRBs and extends to approximately $14°$. A more complex model suggests that there is a dependence of the systematic uncertainty on the position of the GRB in spacecraft coordinates, with GRBs in the quadrants on the *Y* axis better localized than those on the *X* axis.

*Key words:* gamma-ray burst: general – techniques: miscellaneous

*Supporting material:* machine-readable tables

## 1. INTRODUCTION

In four years of operation, the *Fermi Gamma-Ray Space Telescope* has opened a new window to the world of gamma-ray burst (GRB) spectroscopy. Observations by the gamma-ray burst monitor (GBM; Meegan et al. 2009) between 8 keV and 40 MeV and the Large Area Telescope (LAT; Atwood et al. 2009) from 20 MeV to hundreds of GeV have provided a high-energy view over an unprecedentedly broad energy baseline. Follow-up observations of LAT-detected GRBs have revealed the redshifts of about a dozen GRBs detected above 100 MeV (Ackermann et al. 2013 and references therein; Sánchez-Ramírez et al. 2013; Levan et al. 2013; Leloudas et al. 2013; de Ugarte Postigo et al. 2013). Determining the redshifts of GRBs enables the study of the energetics and rest-frame properties of these events. Owing to the localization limitations of the GBM experiment, follow-up observations of GRBs localized at trigger time only by GBM were rare until we disseminated the results of the work presented here, in which uncertainties in GRB localizations are characterized. GRB 090902B (Abdo et al. 2009) was observed by ROTSE (Pandey et al. 2010) an hour after the trigger, with ROTSE tiling the GBM error circle hours before the burst was better localized using LAT and *Swift* data. A source was subsequently found in the ROTSE data at the position of the burst, providing the earliest measurements of the GRB afterglow. GRB 130702A was observed by the intermediate Palomar Transient Factory (iPTF), with the telescope tiling 72 deg$^2$ in 10 separate pointings, and uncovering the afterglow of the GRB 4.2 hr after the GBM trigger (Singer et al. 2013). This was the first discovery of afterglow emission from observations that used only the GBM localization and did not require additional, more accurate, positions from the LAT or from *Swift* to find the source in the large observed sky region. Since then, regular observations by iPTF of GRBs localized by GBM revealed the afterglows for 8 more GRBs in 35 attempts (Singer et al. 2015). In general, however, the small fields-of-view (FoVs) of the most sensitive follow-up telescopes have deterred regular observations of the degrees-scale uncertainty regions resulting from GBM localizations. A further discouraging aspect of GBM localizations is that the total error is often larger than the reported statistical uncertainty. Using a Bayesian method similar to that reported here, Briggs et al. (2009) analyzed 36 GBM GRB localizations and found the 68% confidence level systematic uncertainty to be $3°.8 ± 0°.5$. Hurley et al. (2013) use a sample of 149 GRBs detected by GBM and by other instruments in the InterPlanetary Network (IPN) to infer a 90% confidence level systematic uncertainty of $6°$. We report here a study of systematic uncertainties using over 300 reference locations provided by other instruments and by the IPN. The technique we use is based on the work of Graziani & Lamb (1996) and Briggs et al. (1999), who developed a Bayesian approach to characterize systematic uncertainties for the GRBs detected by

the Burst And Transient Source Experiment (BATSE) on the Compton Gamma-Ray Observatory.

GBM detects about 240 GRBs per year (Paciesas et al. 2012; von Kienlin et al. 2014), providing real-time locations for the follow-up community. Approximately 17% of *Fermi* GBM-detected GRBs are short in duration (von Kienlin et al. 2014). Unlike the short GRB (SGRB) population detected by *Swift*, which may contain weak collapsar events (Bromberg et al. 2013), it is likely that most GBM-detected SGRBs are associated with the merger of compact binary systems. There are therefore 40 or so merger GRBs per year detected by GBM that could potentially be observed at other wavelengths. Mergers of compact binary systems are likely sources of gravitational waves (GW). No associations were found between 154 GRBs detected in 2009–2010 by various spacecraft, including GBM, and potential signals in the LIGO and Virgo GW experiments (Abadie et al. 2012). This was not unexpected given the detection horizon of about 20 Mpc for these experiments. Advanced configurations of both experiments will be deployed over the next few years, with horizons of 400 [1000] Mpc for NS–NS [NS–BH] mergers (Abadie et al. 2010). It is realistic to expect several joint detections of SGRBs by GBM and GW candidates by A-LIGO/Virgo per year (Connaughton et al. 2013). For the first years of A-LIGO/Virgo operation, localization uncertainties for GW candidates are estimated to be 1000 deg$^2$ or more (Aasi et al. 2013), larger than the GBM uncertainty regions, consisting of annuli segments that may encompass non-contiguous sky regions. It is especially important to enable the optical community to observe SGRBs while the afterglow is still bright enough to be detected above the background in a large error box. For GBM-detected SGRBs, this may imply covering only a small part of the error box.

In Section 2 we describe the detection and localization of GRBs by GBM and in Section 3 their dissemination to the public over the GRB Coordinates Network (GCN). The sample of reference locations from detections by other instruments or by the IPN is introduced in Section 4, where reference point locations are compared to the GBM localizations and their reported statistical uncertainties. In Section 5, we describe our method to assess the effect of systematic uncertainties on GRB localization. We report results for the models we tested. In Section 6 we summarize our results and describe new data products that use these results to facilitate follow-up observations of GRBs localized by GBM.

## 2. LOCALIZATION OF GRBs BY GBM

The GBM views the entire unocculted sky, over 7 sr, using 12 sodium iodide (NaI) detectors, 1.27 cm thick and 12.7 cm in diameter, covering an energy range from 8 keV to 1 MeV, and two bismuth germanate (BGO) scintillators, 12.7 cm in diameter and thickness, placed on opposite sides of the spacecraft, with energy coverage from 200 keV to 40 MeV (Meegan et al. 2009). In a coordinate system centered on the spacecraft, the Z axis is oriented along the boresight of the LAT, the X axis joins the two BGO detectors, and the Y axis joins the LAT radiators, as shown in Figure 1. The placement of the NaI detectors, which all have different orientations, in four clusters of three detectors gives maximum coverage along the positive Z axis. This means GRBs in the LAT FoV are seen by more GBM detectors than those outside. If *Fermi* were pointed at the local zenith, the Earth would occupy the region in spacecraft coordinates viewed by the fewest detectors, along the negative Z axis. In nominal sky-survey mode, *Fermi* views the whole sky every three hours (two
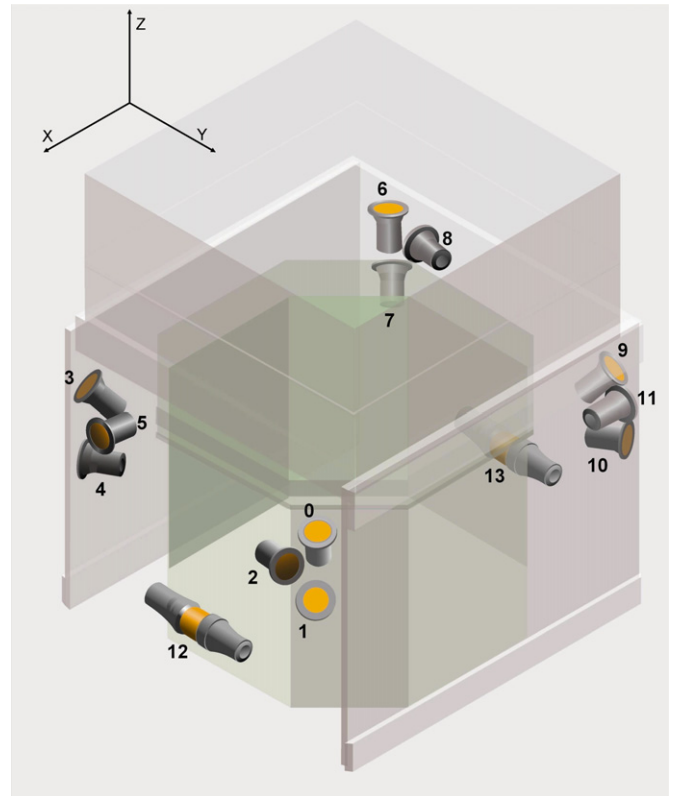


**Figure 1.** In the spacecraft coordinate system, the Z axis is aligned with the LAT pointing. The 14 NaI detectors and 2 BGO detectors are mounted on the +ve and −ve X axes. The NaI detectors are numbered 0–11 and the BGO detectors 0 and 1. The solar panels and LAT radiators are mounted on the +ve and −ve Y axes.

spacecraft orbits) by tilting alternately north and south of the zenith each orbit to obtain uniform sky survey coverage when the exposure is averaged over just a few orbits. The angle of the tilt, called the rocking angle, has changed from 35° at the start of the *Fermi* mission to 50° in 2009 October, the change being necessary to place *Fermi* in a rocking profile that keeps the spacecraft battery cool.

The energy information from the GBM detectors is binned in 128 channels constructed using the 4096 channels in the Data Processing Unit that result from the digitization of the analog output from the detector front-end electronics. Channel-to-energy conversion uses pre-launch exposures to radioactive sources between 14 keV and 4.4 MeV and a spline fit between and beyond the energies of the known sources covers the whole energy range. Details of the energy calibration are given in Bissaldi et al. (2009). The localization of sources is done with an 8 channel rebinning of the full-resolution 128 channel data into a quicklook data type that is downloaded in real-time when a trigger occurs.

Source localization uses the relative rates recorded in the 12 NaI detectors to estimate the most likely arrival direction given the angular and spectral response of the detectors. The detector response model was constructed from simulations incorporating the *Fermi* spacecraft mass model into GEANT4 (Kippen et al. 2007). Incident photons with energies between 5 keV and ∼50 MeV were injected from 272 directions in the spacecraft coordinate system to evaluate the geometry-dependent detector response.

A $\chi^2$ minimization process finds the direction on the sky from which the expected count rates from our detector response

model most closely match the observed detector count rates in all 12 NaI detectors. The observed counts include a background component that is subtracted before modeling the source. The observed source counts are compared to expectation from evenly distributed points on a $1°$ resolution grid in spacecraft coordinates that linearly interpolates among the three closest of the native 272 sky directions giving 41,168 grid points. The source rates contain three elements: direct flux from the source, flux scattered in the spacecraft, and flux scattered from the atmosphere. Contributions from each of these components depend on the observing geometry and on the spectrum of gamma rays from the source. We construct our instrument response matrices for a particular GRB by adding two model terms, the direct response, which depends only on the source-spacecraft geometry, and the atmospheric response, which depends on the source-spacecraft-Earth geometry. The direct response is calculated by interpolating among the three closest of 272 sky points in the native database compiled from the GEANT simulations. Our atmospheric response calculation is a simplification of the true geometry in which the Earth-spacecraft geometry has many solutions. We use the atmospheric response database established for BATSE (Pendleton et al. 1999). For each of the 41,168 grid points we calculate the rates normal to each detector for the Earth-spacecraft geometry at the time of a trigger.

We construct three tables with the model count rates between 50 and 300 keV for each detector at each point on this grid, using three source spectra representing spectrally soft, medium, and hard GRBs. The source spectra are modeled using the Band function parameterization (Band et al. 1993), two power-law components, $\alpha$ and $\beta$, that are smoothly joined, and a peak in the power per decade of energy, $E_{\rm peak}$:

$$F(E) = \begin{cases} \left(\frac{E}{100}\right)^{\alpha} \exp\left[-\frac{(\alpha+2)E}{E_{\rm peak}}\right] \\ \qquad E < [(\alpha-\beta)E_{\rm peak}]/(\alpha+2) \\ = \left(\frac{E}{100}\right)^{\beta} \exp(\beta-\alpha)\left[\frac{(\alpha-\beta)E_{\rm peak}}{100(\alpha+2)}\right]^{\alpha-\beta} \\ \qquad E \geqslant [(\alpha-\beta)E_{\rm peak}]/(\alpha+2) \end{cases}.$$

The Band function parameters for these three spectra are $\alpha$, $\beta$, $E_{\rm peak}$ = $(-1.9, -3.7, 70\ {\rm keV})$, $(-1, -2.3, 230\ {\rm keV})$, and $(0, -1.5, 1\ {\rm MeV})$. Thus, the direct response is fixed and depends only on the source position in spacecraft coordinates. To this we add an atmospheric component that is calculated during the execution of the localization code and that depends on the position of the Earth in spacecraft coordinates. A $\chi^2$ minimization of each of the three tables (soft, medium, hard) relative to the observed rates produces the most likely arrival direction in spacecraft coordinates for each of the three model spectra, and the lowest $\chi^2$ among the three minima is assumed to be from the spectrum that most closely resembles the burst. The position from the selected table is translated to equatorial coordinates using the spacecraft attitude at trigger time. The reported 68% statistical uncertainty is the average distance to the grid points that lie at $\Delta\chi^2 = 2.3$, assuming a circular uncertainty region. A lower limit to the reported statistical uncertainty of $1°$ is imposed to match the grid resolution, though in practice the $\chi^2$ contours can be very steep within the grid points. A discussion of the $\chi^2$ distributions and the selection of the best model based on $\chi^2$ is given in Appendix A.

## 3. GBM LOCALIZATION TYPES

It is desirable to generate GRB localizations as soon as possible after the trigger. An automated process requiring no human intervention produces initial localizations from the on board Flight Software (FSW) algorithms (locations) and on the ground (Ground-Auto locations), both within 10–30 s of the GRB trigger. Refined ground locations use more data and human judgment (Human in the Loop, or HitL locations) and are distributed on the order of an hour later.

When a GBM trigger occurs on board *Fermi*, the GBM FSW produces trigger data types that are downlinked to the ground upon summoning the Tracking and Data Relay Satellite System (TDRSS) link, a 5 s process. In addition to activating a TDRSS link, the GBM FSW communicates with the LAT via the spacecraft bus, informing the LAT FSW that a trigger has occurred, its nature (GRB, solar flare, etc.), and sends a localization produced by the FSW. Because of memory limitations on board, the FSW localization uses a coarser sky grid than previously described $(5°)$ and only one spectral model table, the Band function medium spectrum defined above, to which is added a pre-computed atmospheric scattering component that assumes the Earth is at the spacecraft nadir rather than calculating the atmospheric scattering component at trigger time. The first localization is produced by the FSW using the counts recorded in the most significant data accumulation on 17 timescales ranging from 16 ms to 4.096 s, using data in the time interval leading to the trigger and an additional 1.5 s of data accumulated following the trigger time, to find a $\chi^2$ minimum in the on board model rates table. The LAT uses this location as a seed to allow a less stringent on board trigger level than its usual all-sky on board science algorithm. The FSW produces further localizations if later data accumulations on timescales from 16 ms to 4.096 s are more significant relative to the background level than the initial accumulation at 1.5 s post-trigger, with these later localizations communicated both to the LAT and to the ground.

In addition to the localizations produced by the FSW, TDRSS is also used to transmit the most significant count rates above background on the 16 ms to 4.096 s accumulation intervals, called MAXRATES, with MAXRATES transmission occurring only if the rates are more significant relative to the background level than previous MAXRATES calculations on any timescale. Finally, a background count-rate record is transmitted that contains the average count rates in each detector over a 16 s period prior to the trigger time and separated from the trigger window by 3 s. After reception on the ground, MAXRATES and background packets, which also contain spacecraft position and attitude information, are ingested into the Burst Alert Processor (BAP) at NASA GSFC (or its backup at the GBM Instrument Operations Center in Hunstville). The FSW-determined background rates are subtracted from the MAXRATES to give source rates that are compared to the models. A Ground-Auto localization is generated using the full-resolution model rates tables including an atmospheric response component that uses the true Earth position rather than assuming a zenith-pointed *Fermi* spacecraft. Both FSW and Ground-Auto localizations are communicated as notices to the GCN if the statistical uncertainty is lower than previous FSW or Ground-Auto notices.

Over the next 10 minutes, the FSW transmits via TDRSS a count rate time history covering from 200 s prior to 450 s following the trigger time, and the BAP alerts the GBM

**Table 1**
Types of Localization Produced by GBM for GRB Triggers

| Notice Type | Latency | | Type | Error | | Number |
|---|---|---|---|---|---|---|
| | Minimum | Typical | | Minimum | Typical | |
| On board (FSW) | 4 s[a] | 15–30 s | Peak Flux | 3° | 8°–15° | 1–3 |
| Ground-Auto (GA) | 12 s | | | | | |
| GA 2008−2010 | | 30–60 s | Peak Flux | 1° | 5° | 1–5 |
| GA 2011−2012 | | 60–150 s | Peak Flux | 1° | 5° | 1–5 |
| GA current | | 30–40 s | Peak Flux | 1° | 5° | 1–3 |
| Human-processed (HitL) | 19 minutes | 30–60 minutes | Fluence | 1° | 3° | 0–1 |

**Notes.** Localization uncertainties are 68% CL statistical uncertainties. The Ground-Automated notice latency has varied throughout the mission as described in the text, and each configuration is listed separately. The Human-processed (HitL) notices are a new feature implemented in late 2011.

[a] This latency is lower than the time required to activate the TDRSS link, suggesting the link was already active at trigger time.

Burst Advocate (BA) to the presence of a trigger so that a HitL location can be generated when the real-time data set is complete. Both the FSW and the Ground-Auto locations use single accumulations in intervals from 16 ms to 4.096 s and can thus be considered peak-flux localizations. For the HitL localizations, the BA can select a source interval to produce a fluence localization that should in many cases yield a localization with a smaller statistical uncertainty. The BA selects time intervals before and after the burst emission to fit with a polynomial of the order of up to four as a background model that is subtracted from the observed counts in the source interval prior to the $\chi^2$ minimization.

The three types of localizations are distributed without delay via GCN notices using email and socket connections. FSW notices are sent out for all triggers and include a trigger classification (see Meegan et al. (2009) for a discussion of the FSW trigger classification procedure). Ground-Auto notices are distributed only if the FSW classified the trigger as a GRB at the time the MAXRATES packet was produced and the Ground-Auto localization passed an automated $\chi^2$ quality test (i.e., the localization appears consistent with a distant point source based on the relative rates in the detectors). HitL positions are sent as Final Position notices only if the BA classifies the event as a GRB and the GRB has not been localized more precisely by another instrument at the time of the HitL processing. Table 1 summarizes the types of locations, their reported statistical uncertainties, the typical latencies until the first GCN notice is issued, and the number of notices of each type issued for a trigger classified by the FSW as a GRB.

Latencies for the FSW notices have been stable since launch. An update to the ground localization software in 2011 resulted in longer latencies for the Ground-Auto notices owing to limitations of the BAP hardware and the processing in parallel of multiple MAXRATES packages. An upgrade of the BAP hardware occurred in 2012 and the BAP processing software was also modified to reduce latencies and send notices only if the reported localization uncertainty is smaller than previous notices for that trigger. These changes have resulted in fewer, but more useful, Ground-Auto notices that are distributed more quickly. In 2011, the BAs began distributing the HitL position as a GBM notice, with latencies depending on data availability and BA response time.

## 4. COMPARISON OF GBM LOCALIZATIONS WITH KNOWN GRB LOCATIONS

Between 2008 July and 2013 May, GBM triggered on 203 GRBs that were well-localized by other instruments or by the IPN, with location uncertainties (68% confidence level) smaller than $1°$. These 203 reference locations are listed in Appendix B, Table 9. The ground localization software has been changed several times during the mission. The current version of the code is 4.14g, for both the HitL and the Ground-Auto localizations, and this version is used for comparing the GBM locations with the 203 reference locations, so that the positions are recalculated using the current version rather than using the GRB positions distributed via GCN notices and circulars. It should also be noted that the HitL localizations used in this analysis were redone to ensure the background model and source selection were uninfluenced by the known reference positions. On board localization software has not changed since 2008 October 1 and the FSW locations are assessed using the 192 reference locations from GRBs that occurred after this date.

The main purpose of the FSW locations is to alert the LAT to the occurrence of a GRB. This allows the LAT FSW to adjust its on board algorithm parameters using the temporal and spatial information from GBM. If the GRB is bright or spectrally hard enough, as determined by the GBM FSW, the FSW location is also used to place the GRB near the center of the LAT FoV following an automatic repoint recommendation (ARR) issued by the GBM FSW to the spacecraft. Because the FoV of the LAT is $\sim65°$, the requirements on the FSW localization are loose, $20°$ uncertainty (68% CL) with a goal of $15°$. Figure 2 shows the fraction of FSW localizations within a given offset of the true location for the 192 reference locations. The top panel shows the quality of the initial location, calculated at 1.5 s post-trigger. This can be compared in the bottom panel with the final FSW locations sent out as a GCN notice, a set that includes the initial FSW localizations of GRBs for which only one FSW location was issued. The vertical lines show that 68% of the true positions are contained in a $14°.9$ [$11°.6$] region for the initial [final] FSW locations, with 90% contained within $31°.9$ [$25°.1$]. This is sufficiently accurate for the LAT and the ARR process, and perhaps useful for the follow-up observer on the ground as an alert to begin slewing the telescope a few seconds before the more accurate Ground-Auto locations become available.

Figure 3 shows the true offset from the known source position as a function of the reported statistical uncertainty for both HitL (top) and Ground-Auto (bottom) localizations. Where more than one possible Ground-Auto position exists, we use the last one produced by the BAP that would have been sent out as a notice. Figure 4 shows the fraction of GBM localizations within a given offset of the true location for HitL (top) and Ground-Auto locations. The vertical lines show that 68% of the true positions are contained in a $5°.3$ [$7°.6$] region
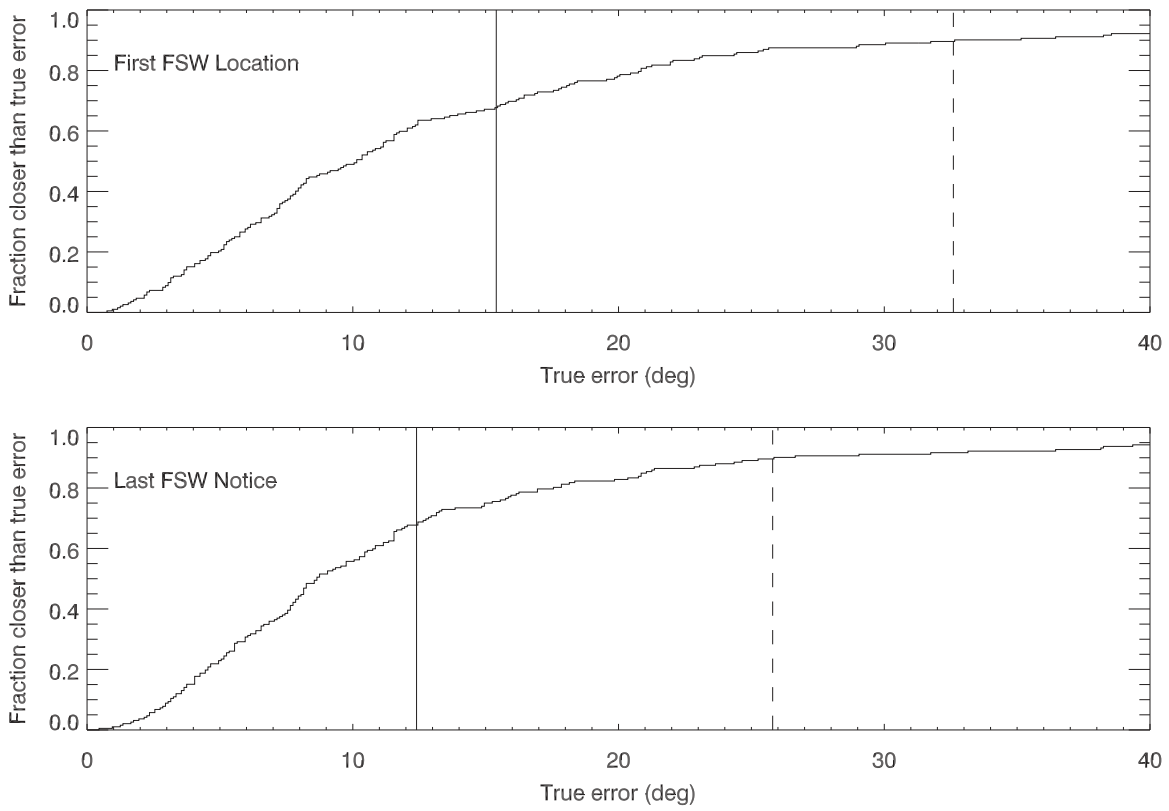
**Figure 2.** Histograms show the fraction of GBM FSW localizations lying within a given offset (degrees) from the true positions for the initial (top) and final (bottom) FSW locations. The solid vertical lines indicate the 68% containment radius of 14.°9 and 11.°6, the dashed vertical lines the 90% containment radius of 31.°9 and 25.°1.
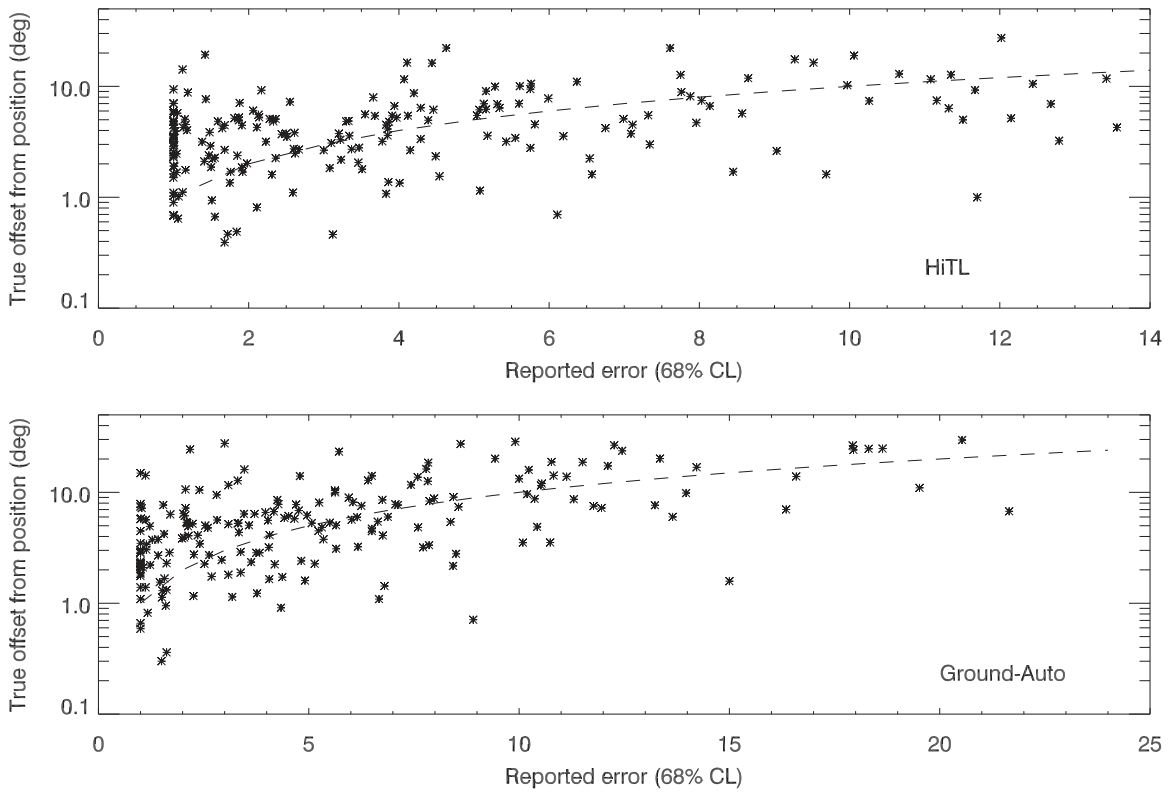


**Figure 3.** True offsets (degrees) from known positions for HitL (top) and Ground-automated (bottom) localizations as a function of the 68% CL statistical uncertainties in the localization. The dashed line shows equality between the quantities. A handful of Ground-Auto positions with uncertainties larger than 30° have been suppressed.
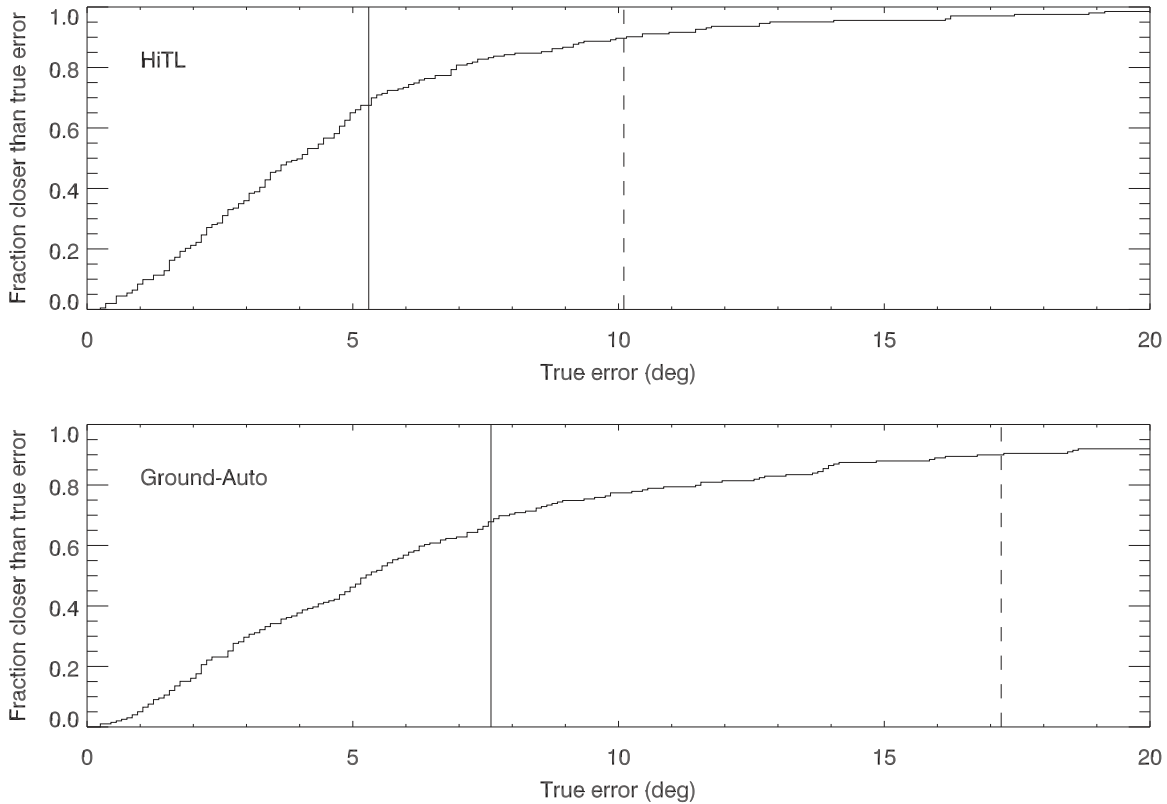
**Figure 4.** Histograms show the fraction of GBM localizations lying within a given offset (degrees) from the true positions for HitL (top) and Ground-automated (bottom) positions. The solid vertical lines indicate a 68% containment radius of $5°\!.3$ [$7°\!.6$], the dashed vertical lines the 90% radius of $10°\!.1$ [$17°\!.2$].

around the HitL [Ground-Auto] locations, with 90% contained within $10°\!.1$ [$17°\!.2$]. Although the Ground-Auto positions appear significantly poorer, it can be seen from Figure 5 that when the offset to the true position is expressed as a multiple of the statistical uncertainty (68% CL), the quality is similar. This reflects the fact that the Ground-Auto locations are peak flux calculations that have fewer source counts than the fluence HitL localizations, resulting in larger statistical uncertainties. The horizontal solid and dashed lines show the fraction of localizations within 1 and $2\sigma$. If the statistical uncertainties reflected the total error, the $1\sigma$ circles should contain 68% of the true source positions but they actually contain 39% [38%] of the true source positions for the HitL and Ground-Auto locations, respectively, increasing to 70% [74%] for the $2\sigma$ regions. This indicates that there is, in addition to the statistical uncertainty, a systematic component to the localization error.

Figure 6 shows the fraction of precisely localized GRBs (statistical uncertainty equal to $1°\!.0$) lying within a given distance of a known position for both HitL and Ground-Auto localizations.

These distributions can serve as a guide to the follow-up observer wishing to concentrate on the brightest, best-localized events without worrying too much about covering the whole uncertainty region, but wanting to know how often they will succeed as a function of how much sky they are willing to tile. A more effective search strategy requires knowledge of the systematic uncertainty in order to probe the larger sky regions that contain most of the probability of the GRB arrival direction. This is of particular interest for archival searches by the multi-messenger community with instruments that do not require pointing a telescope to the source. The sensitivity of such searches, and of any upper limits obtained in the case of a null result, depends on defining a source region narrow enough

to reduce the background but that is still wide enough to capture the source. In view of the connection between GRBs and core-collapse supernovae and the long time interval that can separate the events, it is also essential to define GRB directions in order to connect or reject GRB associations with observed SNe events, as was done, for example, by Soderberg et al. (2010) in the case of SN 2009bb. This will become increasingly important in the era of the Large Synoptic Survey Telescope and the expected discovery of many more optical transients in search of counterparts at other wavelengths.

In the following section, we characterize the systematic uncertainty associated with GBM localizations in order to be able to calculate the probability that any region contains the actual source location. We concentrate on the ground localizations that are most useful for devising a follow-up strategy, although, for completeness, we will briefly characterize the systematic uncertainty associated with the FSW localizations. The reference sample includes the point source locations discussed above and annuli obtained through triangulation by the IPN. For analysis convenience we use only reference locations that may be considered to be points and annuli that may be considered to be lines, with respect to the GBM localization. We include IPN annuli with $3\sigma$ half-widths narrower than $0°\!.8$. For some GRBs the IPN has multiple arcs that intersect to provide an accurate location, with an intersecting region that has a corner-to-corner dimension of less than $1°\!.6$; in these cases we use the intersection closest to the GBM location as a point location. When the IPN has multiple arcs that do not provide an accurate location we use only the narrowest arc in order not to overweight that GRB in the sample. In addition to the 203 point locations described above, 134 GRBs from the IPN-GBM catalog (Hurley et al. 2013) between 2008 July and 2010 July provided 244 annuli, shown in Appendix B, Table 10. After removing annuli that were wider
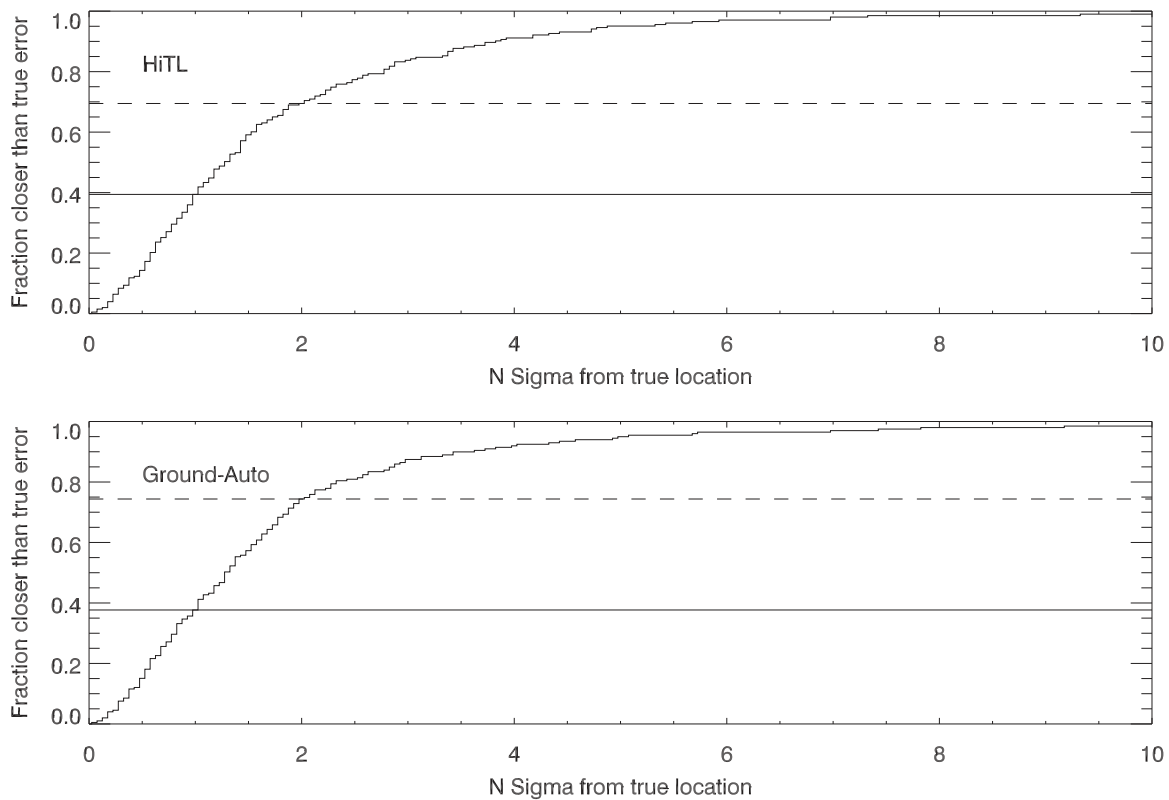
**Figure 5.** Histograms show the fraction of GBM localizations lying within a given offset from the true positions for HitL (top) and Ground-automated (bottom) positions expressed as a multiple of the 68% statistical uncertainties. The solid horizontal lines indicate the reported $1\sigma$ containment radius actually encompasses about 40% of the events, with the dashed lines showing about 70% of events are contained within the $2\sigma$ region.
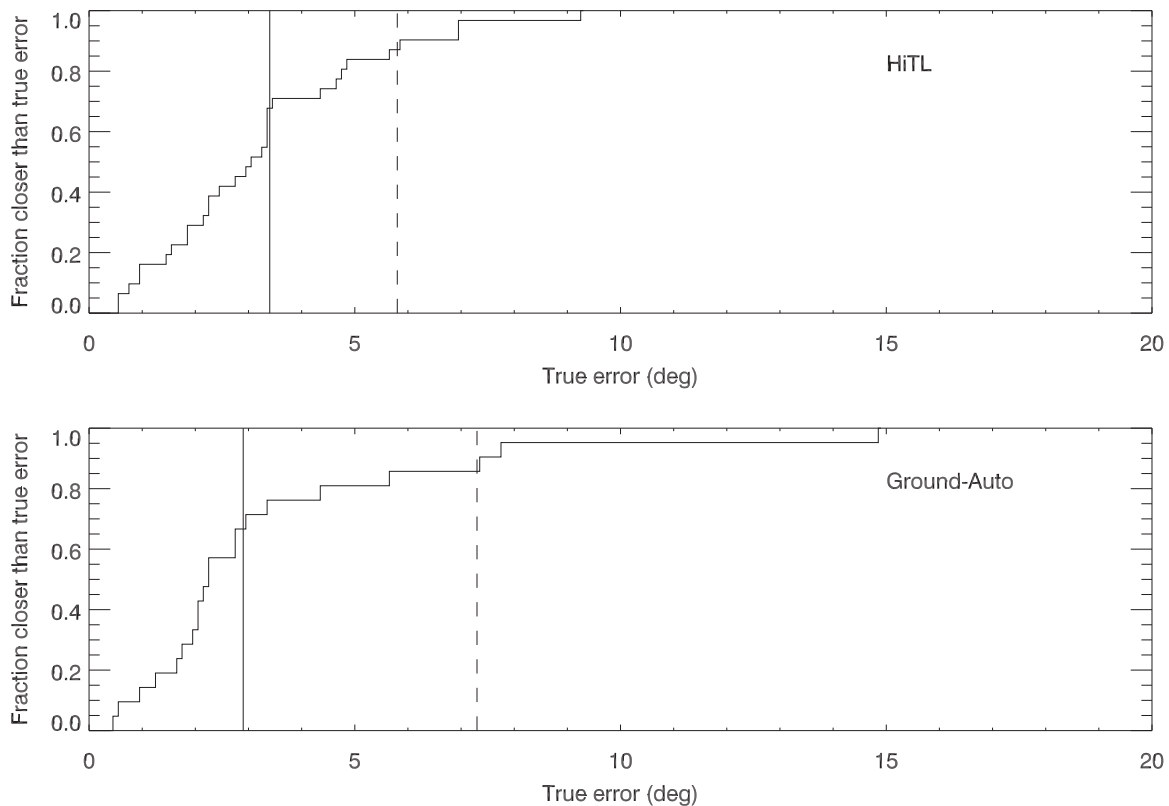


**Figure 6.** Histograms show the fraction of GBM localizations lying within a given offset (degrees) from the true positions for HitL (top) and Ground-automated (bottom) positions with statistical uncertainties of $1°$. The solid vertical lines indicate the 68% containment radius ($3°.4$ or $2°.9$), the dashed vertical lines the 90% radius ($5°.8$ or $7°.3$). There are 31 GRBs in the HitL sample, 21 in the Ground-Auto sample. The 68% containment region for the 68% containment radius for the HiTL sample lies between $3°.3$ and $4°.7$ with the 90% containment radius having a lower limit of $4°.7$ and being unconstrained at the upper end. The 68% containment region for the 68% containment radius for the Ground-Auto sample lies between $2°.2$ and $5°.6$ with the 90% containment radius having a lower limit of $4°.3$ and being unconstrained at the upper end.
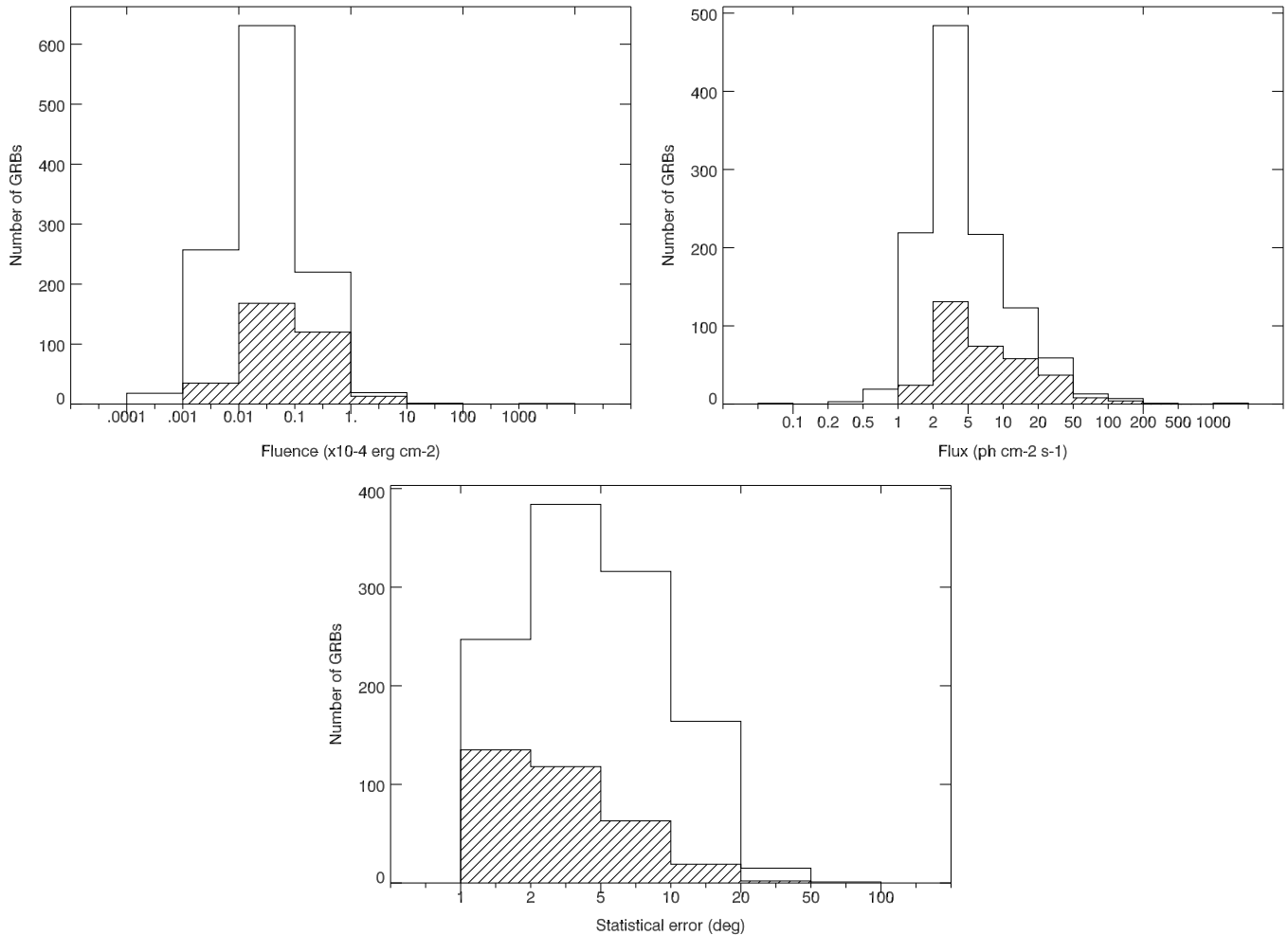
**Figure 7.** Comparison of the properties of GRBs in the reference sample (hashed) to those of the general population of GRBs detected by GBM (solid). The panels show (a) fluence, (b) 1 s peak flux between 10 and 1000 keV, and (c) $1\sigma$ statistical uncertainty on the HitL localization.

than $1°6$ and collapsing intersecting annuli to point sources, this IPN catalog supplied 100 annuli and 9 additional point sources (from 18 intersecting annuli). The $1°6$ acceptance limit for the IPN annuli ensures that only annuli with dimensions smaller than the smallest GBM localization uncertainty are used in the reference sample. Wider annuli would not influence the model fits because their contribution to the constraints on the model parameters would be weighted by the large uncertainty in the dimension (width) that is used to evaluate the best-fit parameters and the goodness-of-fit of the model, but the reference sample would appear larger than the true useful reference sample. These criteria then provide a reference sample with $N_{\text{point}} = 212$ point locations and $N_{\text{arc}} = 100$ arcs.

In Figure 7, we compare the properties of our reference sample to the population of GRBs detected over the same period of time. Although the GRBs in our reference sample are, on average, brighter than other GRBs detected by GBM, with more source counts leading to smaller statistical localization errors, they are more representative of the overall population of GRBs detected by GBM than the reference sample in Briggs et al. (1999) is of the overall GRB population detected by BATSE. The reference GRB population in this work is drawn from experiments with higher fluence thresholds (IPN, *Fermi*-LAT) but also from experiments with equal or lower fluence sensitivity (*Swift*-BAT, *INTEGRAL*), whereas the reference sample in

Briggs et al. (1999) comprised only GRBs bright enough for detection by the IPN.

## 5. INVESTIGATING THE SYSTEMATIC UNCERTAINTY ASSOCIATED WITH GBM LOCALIZATIONS

We use a Bayesian approach to find a model characterizing the systematic uncertainties in GBM localizations. This approach was used by Briggs et al. (1999) to show that the systematic uncertainties in BATSE GRB localizations were better fit using a model that contained most of the probability in a core distribution that peaked at $1°6$, with a larger uncertainty in an extended tail, than by a single component.

The GBM localization program estimates a statistical location uncertainty, $\sigma_{\text{stat}}$. The localization errors are larger due to systematic errors, so we represent the total location uncertainty as $\sigma_{\text{tot}}^2 = \sigma_{\text{stat}}^2 + \sigma_{\text{sys}}^2$. The errors are assumed to be azimuthally symmetric. The models are based on the Fisher probability density function, which has been called the Gaussian distribution on the sphere (Fisher et al. 1987):

$$p_{\text{F}}(\gamma)\, d\Omega = \frac{\kappa}{2\pi(e^{\kappa} - e^{-\kappa})} e^{\kappa \cos \gamma}\, d\Omega, \qquad (1)$$

where $\gamma$ is the angle between the measured and true location, $\kappa$ is termed the concentration parameter, and $d\Omega$ is solid angle.

Considering $\sigma_{\mathrm{tot}}$ to be the radius of the circle containing 68% of the total probability, integrating Equation (1) relates $\kappa$ and $\sigma_{\mathrm{tot}}$ in *radians* (Briggs et al. 1999):

$$\kappa = \frac{1}{(0.66\sigma_{\mathrm{tot}})^2}. \tag{2}$$

We find Equation (2) works well over a broad range of $\sigma_{\mathrm{tot}}$ and use it for all values in our sample.

For comparison with point reference locations, we denote the separation between a GBM localization and the reference location as $\gamma$, while for an arc we denote the separation between the GBM localization and the closest point on the center-line of the annulus as $\rho$. Of course, the true separation might be larger than $\rho$. Our aim is to develop and test models for the GBM localization probability density function $p_\gamma(\gamma)$. We assume the GBM localization probability $p_\gamma(\gamma)$ is a Fisher function or the sum of two Fisher functions:

$$p = f p_F(\gamma_1) + (1 - f) p_F(\gamma_2). \tag{3}$$

For these cases, the probability density function $p_\rho(\rho)$ is known analytically (Briggs et al. 1999).

We use Bayesian model comparison to test models for the systematic error (Loredo 1990; Sivia 1996). Bayesian model comparison is based on the likelihood, which is the product of the probabilities of the observed offsets:

$$\mathcal{L} = \prod_i p_\gamma(\gamma_i) \prod_j p_\rho(\rho_j). \tag{4}$$

The equation shows the dependence of the likelihood $\mathcal{L}$ on the offsets $\gamma_i$, $i = 1, \ldots, N_{\mathrm{point}}$ and $\rho_j$, $j = 1, \ldots, N_{\mathrm{arc}}$; $\mathcal{L}$ also depends on the error model and is a function of the error model parameters through the functions $p_\gamma$ and $p_\rho$. The reference data are of two types, point locations and arcs, disparately testing the quality of the GBM localizations. The Bayesian model comparison naturally handles the difference in evidence since both types of reference data are included in the likelihood via probabilities.

A complicated model with many parameters may have improved likelihood because the model is better or because the additional parameters allow the model to conform to statistical fluctuations. The question is, is the improvement in likelihood sufficient that we should believe in the more complicated model? Bayesian model comparison handles this problem by penalizing models with additional parameters with Occam's factors $F$. Assuming that a reasonable range, or prior, for the parameter $\lambda_k$ is from $\lambda_k^{\min}$ to $\lambda_k^{\max}$, that the model fitting has estimated the parameter uncertainty as $\sigma_{\lambda_k}$ and that the likelihood function is approximately Gaussian, the Occam's factor for parameter $\lambda_k$ is (Sivia 1996):

$$F_k = \frac{\sigma_{\lambda_k}\sqrt{2\pi}}{\lambda_k^{\max} - \lambda_k^{\min}}. \tag{5}$$

We consider all of the models equally plausible (i.e., identical priors), so that the odds ratio $O_{\mathrm{B/A}}$ by which one should favor model B over model A is

$$O_{\mathrm{B/A}} = \frac{P(\mathrm{B})}{P(\mathrm{A})} = \frac{\mathcal{L}(\mathrm{B}) \times \prod F_b^{\mathrm{B}}}{\mathcal{L}(\mathrm{A}) \times \prod F_a^{\mathrm{A}}}. \tag{6}$$

Instead of listing the odds ratios $O_{\mathrm{B/A}}$ for every combination of models A and B we calculate in Tables 2–8 the quantities

$$\log_{10}\left[ \mathcal{L}(\mathrm{M}) \times \prod F_k^M \right]. \tag{7}$$

**Table 2**
Single-component Fits to Systematic Uncertainties on GBM Localizations of Different Types

| Type | Number GRB | | Peak | Error | $\log_{10}$ | $\log_{10}$ |
|---|---|---|---|---|---|---|
| | Point | Annuli | (°) | (°) | Likelihood | Odds Factor |
| Ground-Auto | 208 | 100 | 6.62 | 0.29 | 155.2 | 154.3 |
| HitL 4.14g | 212 | 100 | 5.15 | 0.22 | 224.6 | 223.6 |
| HitL 4.13 | 211 | 100 | 6.23 | 0.26 | 192.6 | 191.7 |

The base-10 logarithm of the odds factor of two models may be obtained by differencing these values.

The following models were tested (where we use the term Gaussian to denote the Fisher function).

1. A single component fit by a Gaussian. This model has a single parameter, the peak position of the Gaussian.
2. A single component modeled by a Gaussian, split into two populations depending on the hemisphere containing the GRB position, in spacecraft coordinates. One model each for the $X$, $Y$ and $Z$ hemispheres splits the GRBs into positive and negative hemispheres. These models have two parameters: the peak of the Gaussian for bursts in each hemisphere.
3. To explore the effects of the symmetry of the *Fermi* spacecraft on the GBM localization accuracy, the samples were also divided according to quadrant, with GRB positions within the $\pm X$ quadrants separated from those localized within the $\pm Y$ quadrants. These models have two parameters: the peak of the Gaussian for bursts in each quadrant set.
4. A core-plus-tail modeled by two Gaussians. This model has three parameters: the peak position of each Gaussian and the fraction in the core.
5. A core-plus-tail modeled by two Gaussians, split into two populations depending on the hemisphere of the GRB position, in spacecraft coordinates (one model each for the $X$, $Y$, and $Z$ hemispheres). Each model has six parameters: the peaks of the two Gaussians and the fraction in the core, for each hemisphere.
6. A core-plus-tail modeled by two Gaussians, split into two sets of quadrants, one containing the GRBs located within the $\pm X$ quadrants, the other within the $\pm Y$ quadrants. This model, like the hemisphere models, has six parameters.

Tables 2 and 3 show the results for the most basic single-component and core-plus-tail fits to the systematic uncertainties on the Ground-Auto, and HitL localizations. In addition to the current version of the localization software, 4.14g, fits for version 4.13 of the HitL localization are included in order to characterize the localizations in the first pair of GRB catalogs and part of the second pair of GRB catalogs (Paciesas et al. 2012; Goldstein et al. 2012; von Kienlin et al. 2014; Gruber et al. 2014), which used this older version. The main change implemented in 4.14g was the selection of a model spectrum based on the $\chi^2$ values of the best-fit location using all three model spectra rather than a priori using three bands of hardness ratio values to classify the GRB as soft, medium, or hard and finding the $\chi^2$ minimum only in the single corresponding model rates table. Looking at the difference between the odds factors between the single-component fits in Table 2 and the core-plus-tail fits in Table 3, it can be seen that a core-plus-tail model is favored over a single component model by factors of $10^{17}$,

**Table 3**
Core-plus-tail Fits to Systematic Uncertainties on GBM Localizations of Different Types

| Type | Number GRB | | Core | Error | Core | Error | Tail | Error | log₁₀ | log₁₀ |
|---|---|---|---|---|---|---|---|---|---|---|
| | Point | Annuli | (°) | (°) | (%) | (%) | (°) | (°) | Likelihood | Odds Factor |
| Ground-Auto | 208 | 100 | 3.72 | 0.34 | 80.4 | 5.3 | 13.7 | 1.7 | 174.1 | 171.8 |
| HitL 4.14g | 212 | 100 | 3.71 | 0.24 | 90.0 | 3.5 | 14.3 | 2.5 | 241.3 | 238.9 |
| HitL 4.13 | 211 | 100 | 3.57 | 0.32 | 79.8 | 5.3 | 12.7 | 1.5 | 213.5 | 211.1 |

Table 3 header note: Core + Tail (2 Gaussians)

**Table 4**
Quadrant-dependent Core-plus-tail Fits to Systematic Uncertainties on GBM Localizations

Core + Tail (2 Gaussians) with Quadrant Dependence

| Type | Quadrants | Number GRB | | Core | Error | Core | Error | Tail | Error | log₁₀ | log₁₀ |
|---|---|---|---|---|---|---|---|---|---|---|---|
| | | Point | Annuli | (°) | (°) | (%) | (%) | (°) | (°) | Likelihood | Odds Factor |
| Ground-Auto | All-sky | 208 | 100 | 3.72 | 0.34 | 80.4 | 5.3 | 13.7 | 1.7 | 174.1 | 171.8 |
| Ground-Auto | ±X | 208 | 100 | 4.10 | 0.48 | 75.4 | 8.2 | 13.1 | 2.1 | | |
| | ±Y | | | 3.06 | 0.61 | 80.6 | 8.9 | 12.9 | 2.9 | 175.0 | 171.7 |
| HitL 4.14g | All-sky | 212 | 100 | 3.71 | 0.24 | 90.0 | 3.5 | 14.3 | 2.5 | 241.3 | 238.9 |
| HitL 4.14g | ±X | 212 | 100 | 4.30 | 0.38 | 90.3 | 5.9 | 15.0 | 4.8 | | |
| | ±Y | | | 3.34 | 0.26 | 92.0 | 3.5 | 14.5 | 3.5 | 242.6 | 238.7 |
| HitL 4.13 | All-sky | 211 | 100 | 3.57 | 0.32 | 79.8 | 5.3 | 12.7 | 1.5 | 213.5 | 211.1 |
| HitL 4.13 | ±X | 211 | 100 | 4.22 | 0.87 | 72.8 | 15.5 | 11.5 | 2.4 | | |
| | ±Y | | | 3.24 | 0.35 | 89.4 | 5.1 | 16.8 | 3.3 | 216.2 | 213.0 |

**Table 5**
Effect of Varying the Quadrant Boundaries when Assessing the Quadrant-dependent Core-plus-tail Fit to the Systematic Uncertainty on GBM Localizations

Core + Tail (2 Gaussians) Varying the Azimuth Boundaries of the Quadrants
Version 4.14g of the HitL Code with 212 Reference Locations and 100 IPN Annuli

| No. | Quadrants | Azimuth Ranges | Core (°) | Error (°) | Core % | Error % | Tail (°) | Error (°) | log₁₀ Likelihood | log₁₀ Odds Factor |
|---|---|---|---|---|---|---|---|---|---|---|
| 1 | All-sky | 0°–360° | 3.71 | 0.24 | 90.0 | 3.5 | 14.3 | 2.5 | 241.3 | 238.9 |
| 2 | ±X | 315°–45° and 135°–225° | 4.30 | 0.38 | 90.3 | 5.9 | 15.0 | 4.8 | | |
| | ±Y | 45°–135° and 225°–315° | 3.34 | 0.26 | 92.0 | 3.5 | 14.5 | 3.5 | 242.6 | 238.7 |
| 3 | ±X | 320°–40° and 140°–220° | 4.23 | 0.52 | 87.2 | 7.7 | 14.1 | 4.8 | | |
| | ±Y | 40°–140° and 220°–320° | 3.47 | 0.25 | 93.6 | 3.3 | 15.5 | 3.6 | 242.6 | 238.8 |
| 4 | ±X | 305°–55° and 125°–235° | 4.25 | 0.32 | 92.6 | 4.6 | 15.9 | 4.7 | | |
| | ±Y | 55°–125° and 235°–305° | 3.16 | 0.45 | 90.2 | 4.8 | 14.8 | 3.6 | 242.6 | 238.8 |
| 5 | ±X | 300°–60° and 120°–240° | 4.32 | 0.29 | 93.4 | 4.0 | 16.2 | 4.9 | | |
| | ±Y | 60°–120° and 240°–300° | 2.59 | 0.40 | 86.6 | 6.1 | 13.5 | 3.2 | 243.9 | 240.1 |
| 6 | ±X | 295°–65° and 115°–245° | 4.17 | 0.28 | 91.3 | 3.9 | 15.5 | 3.6 | | |
| | ±Y | 65°–115° and 245°–295° | 2.42 | 0.38 | 89.3 | 5.7 | 13.2 | 3.9 | 244.2 | 240.2 |
| 7 | ±X | 292.5–67°.5 and 112.5–247°.5 | 4.17 | 0.28 | 91.8 | 3.9 | 15.3 | 3.6 | | |
| | ±Y | 67.5–112°.5 and 247.5–292°.5 | 2.31 | 0.39 | 88.4 | 6.4 | 13.2 | 3.8 | 244.2 | 240.3 |
| 8 | ±X | 290–70° and 110–250° | 4.12 | 0.28 | 91.7 | 3.9 | 14.9 | 3.6 | | |
| | ±Y | 70–110° and 250–290° | 2.35 | 0.43 | 87.0 | 7.0 | 12.7 | 4.0 | 243.7 | 239.9 |
| 9 | ±X | 285–75° and 105–255° | 3.96 | 0.26 | 89.9 | 3.8 | 15.3 | 2.9 | | |
| | ±Y | 75–105° and 255–285° | 2.64 | 0.54 | 90.7 | 10.6 | 9.1 | 4.8 | 243.0 | 239.4 |

$10^{16}$, and $10^{19}$ for the Ground-Auto, HitL 4.14g, and HitL 4.13, respectively. The fraction in the core for the HitL localizations is higher using the more recent code, consistent with Version 4.14g being more robust, although the core values agree within errors, and are in fact slightly lower using the older code.

Results for single-component models exploring the effects of GRB location in spacecraft coordinates on the systematic error are shown in Appendix C. Table 11 shows that parameter values are similar for the systematic errors of GRBs in each of the hemispheres. There is no consistent statistical preference among the three localization types for models based on GRB position in spacecraft coordinates although individual localization types show slight preferences for hemisphere- or quadrant- dependent models. Owing to the placement of the GBM NaI detectors, which maximizes sensitivity in the +Z hemisphere to optimize coverage of GRBs in the LAT FoV, GRBs in the +Z hemisphere

**Table 6**
Estimate of Systematic Uncertainty on the Initial FSW Localizations at 1.9 s Post-trigger

| | FSW Initial Locations: Single Component Models Across Hemispheres | | | | | |
|---|---|---|---|---|---|---|
| Model | Number GRB | | Peak | Error | $\log_{10}$ | $\log_{10}$ |
| | Point | Annuli | (°) | (°) | Likelihood | Odds Factor |
| Single | 187 | 0 | 15.4 | 0.8 | 3.7 | 3.2 |
| Hemisphere $+X$ | 187 | 0 | 12.2 | 1.2 | | |
| $-X$ | | | 17.2 | 1.2 | 5.5 | 4.9 |
| Hemisphere $+Y$ | 187 | 0 | 12.7 | 1.0 | | |
| $-Y$ | | | 18.2 | 1.4 | 6.0 | 5.4 |
| Quadrants $\pm X$ | 187 | 0 | 19.7 | 1.6 | | |
| $\pm Y$ | | | 12.5 | 0.9 | 7.5 | 6.9 |

**Table 7**
Estimate of Systematic Uncertainty on the Last-issued FSW Localizations

| | | Core + Tail Fits to the Systematic Uncertainty on the FSW Final Locations | | | | | | | | |
|---|---|---|---|---|---|---|---|---|---|---|
| Type | Hemisphere | Number GRB | | Core | Error | Core | Error | Tail | Error | $\log_{10}$ | $\log_{10}$ |
| | | Point | Annuli | (°) | (°) | % | (%) | (°) | (°) | Likelihood | Odds Factor |
| | All-sky | 192 | 0 | 7.52 | 0.76 | 89.7 | 2.9 | 55.6 | 9.0 | 39.6 | 38.1 |
| Quadrant | $\pm X$ | 192 | 0 | 8.29 | 1.34 | 85.7 | 6.2 | 59.6 | 12.9 | | |
| | $\pm Y$ | | | 7.35 | 1.03 | 92.9 | 3.7 | 62.6 | 18.5 | 40.1 | 38.5 |
| Hemi | $+X$ | 192 | 0 | 5.99 | 1.12 | 86.3 | 4.6 | 47.2 | 9.0 | | |
| | $-X$ | | | 8.80 | 1.02 | 92.2 | 3.4 | 68.2 | 27.2 | 40.4 | 38.5 |
| Hemi | $+Y$ | 192 | 0 | 7.84 | 1.16 | 92.4 | 4.9 | 35.6 | 12.3 | | |
| | $-Y$ | | | 6.66 | 1.17 | 84.3 | 4.8 | 62.2 | 13.2 | 41.3 | 39.5 |
| | The $Z$-hemisphere Model Failed to Converge. The $Z$-hemisphere-dependent Single Component is Below | | | | | | | | | | |
| Single | $+Z$ | 192 | 0 | 12.18 | 0.7 | | | | | | |
| | $-Z$ | | | 34.09 | 2.71 | | | | | 13.0 | 12.6 |

**Table 8**
Effect of Rocking Angle Change on the Quality of FSW Final Locations

| | | Effect of Rocking Angle Change on FSW Localization Systematic Uncertainty | | | | | | |
|---|---|---|---|---|---|---|---|---|
| Type | Hemisphere | Core | Error | Core | Error | Tail | Error | $\log_{10}$ | $\log_{10}$ |
| | | (°) | (°) | (%) | (%) | (°) | (°) | Likelihood | Odds Factor |
| | | FSW Final Locations for 43 GRBs in Initial Rocking Profile | | | | | | | |
| All-sky | | 5.80 | 0.99 | | | | | 25.3 | 24.9 |
| Hemi | $+Y$ | 4.52 | 1.39 | | | | | | |
| | $-Y$ | 6.98 | 1.58 | | | | | 25.6 | 25.2 |
| Quad | $\pm X$ | 8.10 | 1.79 | | | | | | |
| | $\pm Y$ | 3.82 | 1.26 | | | | | 26.2 | 25.9 |
| | | FSW Final Locations for 149 GRBs Since the Rocking Angle Change | | | | | | | |
| All-sky | | 8.32 | 1.01 | 87.0 | 3.8 | 56.6 | 9.8 | 17.1 | 15.9 |
| Hemi | $+X$ | 7.59 | 1.32 | 84.0 | 5.7 | 48.8 | 10.1 | | |
| | $-X$ | 9.14 | 1.26 | 89.9 | 4.6 | 67.7 | 27.0 | 17.3 | 15.9 |
| Hemi | $+Y$ | 10.21 | 1.46 | 95.1 | 5.4 | 48.2 | 29.6 | | |
| | $-Y$ | 6.18 | 1.77 | 79.9 | 6.3 | 60.1 | 12.6 | 19.0 | 18.0 |
| Hemi | $+Z$ | 7.52 | 1.42 | 93.1 | 5.4 | 42.4 | 15.9 | | |
| | $-Z$ | 10.40 | 2.32 | 67.3 | 9.9 | 63.0 | 14.8 | 21.0 | 20.1 |
| Quad | $\pm X$ | 7.93 | 1.63 | 78.5 | 7.4 | 52.6 | 10.7 | | |
| | $\pm Y$ | 9.26 | 1.09 | 93.3 | 3.8 | 71.9 | 51.7 | 17.8 | 16.8 |

**Notes.** The systematic error for the sample of 43 GRBs before the spacecraft rocking angle increased from 35° to 50° is modeled by a single Gaussian. More complicated models failed to converge, possibly owing to the small sample size. For the 149 GRBs detected after the rocking angle change, only the core-plus-tail models converged, probably because the systematic errors associated with the tail of the population were too large for a single-component model to result in an acceptable fit.

are more plentiful, viewed by more detectors, and might be expected to have more accurate localizations. The weak sensitivity of the systematic error to GRB position along the $Z$ axis suggests that any such effect is encompassed with a larger statistical error for the bursts viewed with fewer detectors in the $-Z$ hemisphere. If we look at the cumulative fraction of GRBs lying within a given offset of the true location, we find that for HitL 4.14g the 68% [90%] containment radius is 5°.1 [9°.9]

for GRBs localized in the $+Z$ hemisphere versus 5°.3 [10°.9] for those in the $-Z$ hemisphere. This difference is larger for version 4.13: 6°.1 [11°.1] in the $+Z$ hemisphere versus 6°.8 [15°.0] in the $-Z$ hemisphere, consistent with the results shown in Table 11. These numbers also suggest the overall quality of the 4.14g locations is higher than the older version and fewer outliers are produced. The odds ratios for all of the single-component models are much lower than the core-plus-tail model in Table 3, which is thus greatly preferred over any of the single-component models.

Results for core-plus-tail models that explore the effect of GRB position in different spacecraft hemispheres are described in Appendix D. Table 12 shows that localizations using HitL 4.14g are fit with lower parameter values for GRBs in the $+Z$ hemisphere, although this model is not preferred statistically over the simpler, all-sky core-plus-tail model in Table 3. Other hemisphere-dependent core-plus-tail models did not yield significantly different parameters in the two hemispheres, nor were they statistically favored.

Table 4 shows the model fit parameters for localizations grouped according to GRB position within the $\pm X$ and $\pm Y$ quadrants. Unlike the grouping into hemispheres, the differences in parameter values for quadrant-dependent models for all three types of localization cannot be explained by juggling events from the core to the tail. Instead, the $\pm Y$ quadrant GRBs are more likely to be localized with a systematic error in the core, and the value of the systematic error in the core is smaller than for events in the $\pm X$ quadrants. The odds factors for these models can be compared with the all-sky core-plus-tail model repeated in line 1 of the table. This six-parameter model is favored only for HitL 4.13, which had a larger population of outliers in the tail than HitL 4.14, but the parameter values are suggestive that this six-parameter model should be favored over the simpler three-parameter core-plus-tail model with a larger sample or more judiciously chosen quadrants.

Table 5 displays the quadrant-dependent core-plus-tail model parameters and odds ratios with sliding quadrant azimuth ranges. A larger sample of reference locations will, in the future, allow the quadrant ranges to vary as free parameters but a model with these extra free parameters is too complicated to converge with the current sample. The core-plus-tail models are significantly preferred over single Gaussians so that optimizing the quadrant azimuth ranges with a single Gaussian model is not explored. Entry 1 is the standard all-sky core-plus-tail model, which was found to represent the data better than any of the single-component models we explored. Entry 2 has equal azimuth ranges in each quadrant. Entry 3 explores the effect of making the $\pm Y$ quadrant bigger. This provides no improvement and moves the quadrant core parameter values closer to each other. Narrowing the $\pm Y$ quadrant produces fits that increasingly differentiate between the quadrants, with increasingly favorable odds factors exceeding the simple three-parameter model. When the $\pm Y$ quadrant becomes too small to contain enough events to constrain the parameters, the odds factor once more decreases. The model that maximizes the odds factor, entry 7, also differentiates the most between the quadrants, with small parameter errors and close to 90% of GRBs in the core in each quadrant set. It is preferred over the all-sky core-plus-tail model by a factor of 16. This set of parameters defines $\pm Y$ quadrants with 45° azimuth in each quadrant and lower systematic errors for GRBs localized in these quadrants than for those in the $135° \pm X$ quadrants. This quadrant definition also produces larger odds factors for the Ground-Auto localizations
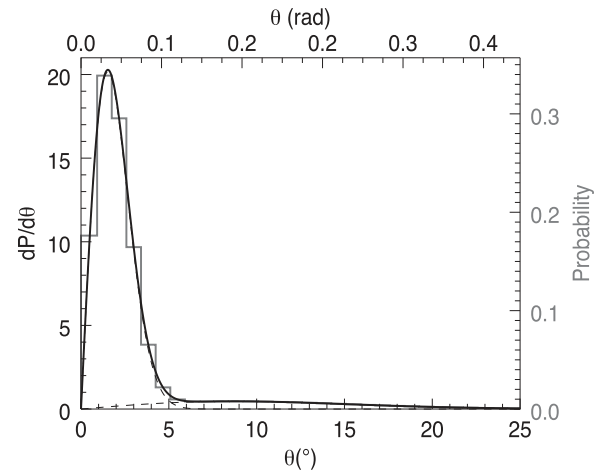


**Figure 8.** Solid curve shows the sum of the two components in the core and tail of a model representing the total 68% confidence level systematic uncertainty for GRBs localized in the $\pm Y$ quadrants in the spacecraft coordinate frame. The dashed curves show the individual components for the core and tail of the model. The histogram shows the probability of a systematic error for a given angular bin.

than the core-plus-tail model that has equal 90° quadrants, with the Ground-Auto providing an independent data set from the same GRB sample. This quadrant-dependent core-plus-tail model for the systematic uncertainty associated with GBM GRB localizations is illustrated in Figure 8. The figure shows how the probability of the systematic uncertainty changes as a function of angular offset from a GBM GRB localization for GRBs localized in the $\pm Y$ quadrants.

### 5.1. Flight Software Systematic Localization Uncertainties

Both the initial and final FSW locations had sufficiently distant outliers ($>90°$) that most single component fits did not converge. Removing the five worst localizations allowed the fitting of several single component models for the Initial locations, shown in Table 6. The IPN annuli were also removed as it could not be determined for these reference locations which were the worst outliers and the fits failed to converge when they were included. The single-component fits for the FSW Initial locations are presented because these were the only fits that converged, and the parameter values may be useful, but it should be noted that these fits omit the five worst localizations.

Fits using the more complex core-plus-tail models converged using the entire FSW Final location sample (omitting the IPN set). These fits and the single component fits with a $Z$ hemisphere dependence for the FSW Final locations, the only single-component model that converged with the entire sample, are reported in Table 7.

In 2009 September, the *Fermi* rocking angle changed from 35° to 50°. The rocking angle change was necessary to keep the spacecraft battery cool, but one unfortunate effect on GBM is that more GRBs are viewed with an unfavorable detector geometry and the GBM localization quality may have suffered. Because of on board hardware limitations, the full atmospheric scattering calculation performed on the ground is replaced by a standard model table for the atmospheric scattering contribution that assumes a zenith-pointed spacecraft. This becomes increasingly unrealistic with the updated rocking angle but the on board limitations do not permit multiple tables that would cover several possible *Fermi* pointings. In order to assess
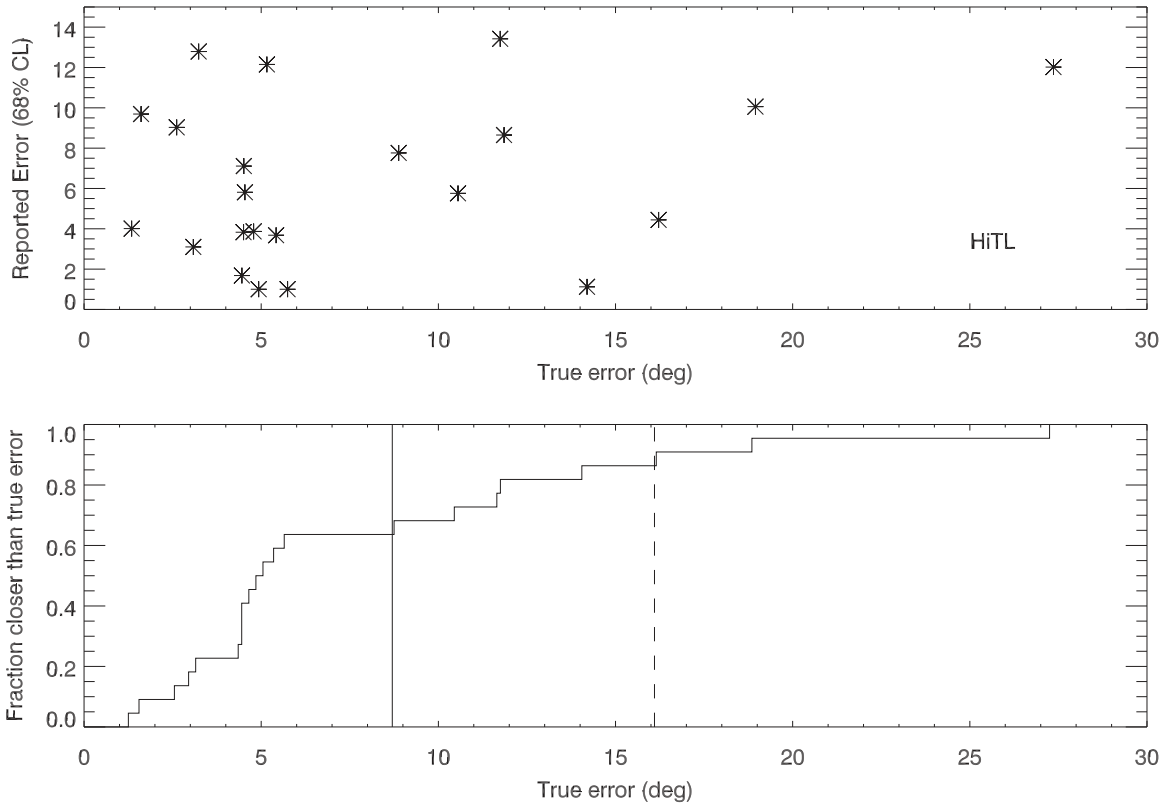
**Figure 9.** Reported 68% CL uncertainty for 22 SGRBs localized by GBM is shown in the top panel as a function of the true offset. The histograms show the fraction of GBM HitL localizations lying within a given offset (degrees) from the true position. The solid vertical line indicates the 68% containment radius 8°.7 and the dashed vertical line the 90% radius of 16°.1. The 68% containment region for the 68% containment radius for the HiTL locations lies between 5°.3 and 11°.7 with the 90% containment radius having a lower limit of 11°.6 and being unconstrained at the upper end.

the effect of this change on the FSW localizations, the FSW Final location sample was split into the 43 GRBs occurring before the change and the 149 since then. Table 8 shows a comparison of the systematic errors on these localizations. Single-component fits were possible with the smaller sample and only core-plus-tail modeling was possible with the larger sample. It appears the worst outliers have been detected since the rocking angle change and the value of the systematic error for the core is higher than the single model that best fits the sample localized before the rocking angle change. This suggests there has been a deterioration in the quality of the FSW localizations since 2009 September.

### 5.2. The Special Case for Short GRBs

SGRBs (duration <2 s) are especially interesting to the follow-up community, both because they are rarer and because their putative association with the merger of a neutron star with either a neutron star (NS–NS) or a black-hole (NS–BH) is less well established than the connection between long GRBs and the collapse of massive stars. It is useful to characterize the systematic errors of the SGRB localizations in order to assess the regions with the maximum probability of containing the source or to calculate the probability that the GRB was in a region observed in another wavelength.

Only 22 of the 203 reference locations in our sample are for SGRBs, and an additional 13 SGRBs have narrow IPN annuli. The top panel of Figure 9 shows the reported 68% CL error on the GBM locations as a function of their offset from the real GRB position for the HitL localizations of the 22 SGRBs in our sample. The cumulative distribution of offsets from the true

position appears in the bottom panel. Owing to the low fluences of SGRBs, they are typically localized with larger statistical uncertainties than long GRBs. The 68% and 90% containment radii of the true positions from the GBM positions are 8°.7 and 16°.1, respectively, but with large uncertainties owing to the small sample size. There is a steep rise in containment of the true source position at just under 6° from the GBM position after which it remains flat, though with 22 events this curve may also result from small statistics. Covering an area 6° around the reported position might be a good strategy, regardless of the reported error on the localization, which is only weakly correlated with the true source offset for these short events. Ground-automated localizations of SGRBs are displayed in the same way in Figure 10. It can be seen that although the containment radii are higher (10°.5 and 26°.5 for the 68% and 90% sample containment), there is a similar steep rise at just under 6° from the position reported by GBM so that with a limited FoV, observers would capture 50% of the true positions using a search radius of 6°.

More SGRBs with known positions are required to characterize the systematic error on these events convincingly. A preliminary analysis of the HitL 4.14g locations for SGRBs using our Bayesian code, which uses 13 IPN annuli in addition to the 22 reference locations, suggests a single-component systematic uncertainty of 7°.0 ± 1°.0. A core-plus-tail model with 4°.7 ± 1°.0, a core fraction of 78% ± 2% and a tail component of 12° ± 5° is mildly preferred and suggests the short burst systematic uncertainties are compatible with those of the GRB population as a whole, with the exception that the fraction in the tail is higher. This could explain the larger systematic uncertainty obtained in the single-component model for the short bursts compared to the

13
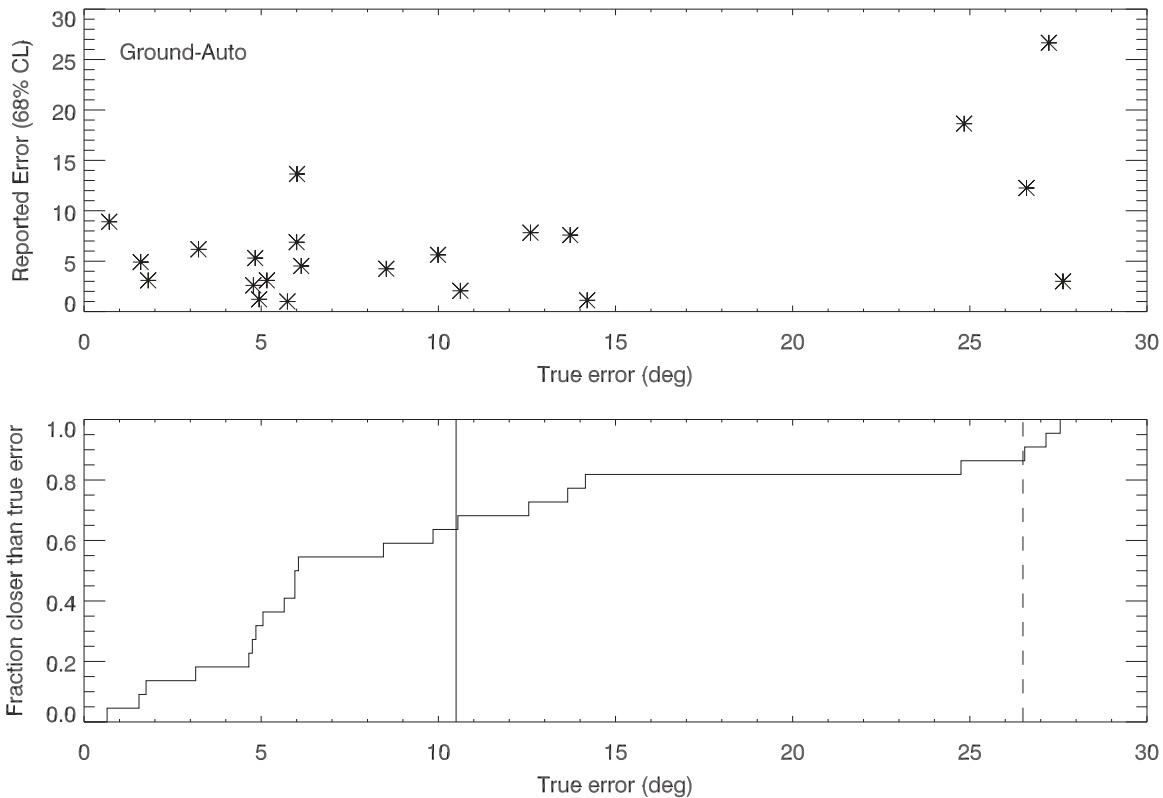
**Figure 10.** Reported 68% CL uncertainty for 22 short GRBs localized by GBM using the ground-automated process is shown in the top panel as a function of the true offset. The histograms show the fraction of GBM Ground-Auto localizations lying within a given offset (degrees) from the true position. The solid vertical line indicates the 68% containment radius $10°.5$ and the dashed vertical line the 90% radius of $26°.5$. The 68% containment region for the 68% containment radius for the Ground-Auto locations lies between $8°.4$ and $14°.1$ with the 90% containment radius having a lower limit of $13°.6$ and being unconstrained at the upper end.

population as a whole ($5°.2 \pm 0°.2$). Attempts to characterize the systematic uncertainty associated with the Ground-Auto localizations fail with this small sample. The sample of SGRBs with IPN annuli can be increased using the large number of SGRBs seen only by GBM and Konus-Wind (Pal'shin et al. 2013).

### 5.3. Applying the Model to the Data

Figure 5 showed that only 39% of the HitL localizations fell within the $1\sigma_{\mathrm{stat}}$ statistical uncertainty region of the true reference location, $\sigma_{\mathrm{stat}}$, with 70% within $2\sigma_{\mathrm{stat}}$. If we convolve the statistical uncertainty, assuming circular uncertainty regions, with the best-fit quadrant-dependent core-plus-tail model of the systematic uncertainty, $\sigma_{\mathrm{sys}}$, explored in Section 5, adding the functions in quadrature $\sigma_{\mathrm{tot}} = \sqrt{(\sigma_{\mathrm{stat}}^2 + \sigma_{\mathrm{sys}}^2)}$, then we find that 67.5% lie within the $1\sigma_{\mathrm{tot}}$ radius and 94.5% within $2\sigma_{\mathrm{tot}}$. If instead of the circular assumption we make for $\sigma_{\mathrm{stat}}$ we convolve the $\chi^2$ map with the model for the systematic uncertainty that was found to be the best fit of those we explored in Section 5, these numbers are 68.7% and 91.4%, respectively. Similar results are found for the Ground-auto localizations. Propagating the uncertainties on the model parameters produces a variation of 1%–2% in these containment percentages.

### 6. SUMMARY AND FUTURE PLANS

Using a reference sample of 203 GRBs with known locations we have found that ground-automated GBM localizations distributed as Ground Position GCN notices between 30 s and about a minute after the trigger time lie within $7°.6$ of the true location 68% of the time and within $17°.2$ 90% of the time (Figure 4). These numbers are for the population as a whole and do not take

into account the reported statistical uncertainty. For GRBs with small statistical localization uncertainties of $1°$ this improves to $2.2$–$5°.6$ for the 68% containment level, with the sample of GRBs with localization errors this small insufficient to determine the 90% containment level (Figure 6). The localizations produced with human intervention (HitL) that are distributed as Final Position GCN notices 30 minutes to hours after the trigger are within $5°.3$ and $10°.1$ of the true position for 68% and 90% of GRBs, respectively. For GRBs with statistical localization uncertainties of $1°$ the 68% containment radius is $3°.3$–$4°.7$ with the sample again too small to determine the 90% containment radius.

An analysis of the systematic uncertainty on GBM localizations that takes into account the reported statistical uncertainty used, in addition to the 203 point locations, 100 IPN annuli and 9 IPN intersecting annuli that are treated as point locations, for a total of 312 reference locations. The model that best represents the systematic uncertainty for both the automated and HitL localizations includes a core component and a tail component. For the Ground-Auto, the core component is a Gaussian that peaks at $3°.7 \pm 0°.3$ and contains about 80% of the GRB locations, with a Gaussian tail peaked at $14° \pm 2°$. The HitL systematic uncertainty has similar values but 90% of the localizations are contained in the core (Table 3). Both localization types show evidence for a dependence of the error on the GRB position in spacecraft coordinates, with bursts incident near the $\pm Y$ axes better localized than those near the $\pm X$ axes (Table 4). With three extra parameters, the size of the reference sample is not large enough for this model to be preferred statistically. Modifying the azimuthal area covered in these $X$ and $Y$ axes produces a model for the HitL localizations that is preferred over

the simpler core-plus-tail model described above (Table 5). Because the parameters in this model are well-constrained and the results are reproduced using the Ground-Auto localizations, we consider this a good model for the systematic uncertainty of GBM-localized GRBs.

Applying this model to the data, using either the circular approximation to $\sigma_{stat}$ that was input to the Bayesian model or the actual $\chi^2$-grid values to define the statistical confidence levels, resulted in the containment percentages of the reference locations within the expected total uncertainty regions.

The quality of our localization depends on the quality of the model rates that we compare with our observed rates. This in turn relies on our knowledge of the detector responses both to the direct flux and to the scattered flux from both the spacecraft and the atmosphere. Systematic effects owing to a poor choice of model spectrum may contribute to a poor localization, as can inaccuracies in our detector response, our mass model of the *Fermi* spacecraft, and our model of scattering from the atmosphere. The dependence of the systematic uncertainty in our localization on the position of the GRB in spacecraft coordinates may offer clues to the major sources of these systematic errors. A systematic error that was dominated by our detector responses or by inaccuracies in our atmospheric scattering modeling is unlikely to exhibit such a dependence on position in spacecraft coordinates, although both of these factors may play a part. The $\pm X$ sides of the spacecraft contain much of the wiring and electronics boxes, with the $-X$ side also housing the star trackers. By contrast, the $\pm Y$ sides, housing the LAT radiators and solar panels, are clearer of material. The quadrant dependence of $\sigma_{sys}$ implies that the bursts incident on parts of the spacecraft with fewer electronics boxes and large cable bundles have better localizations than those arriving on a busier part of the spacecraft. This may imply inaccuracies in our mass model lead to a miscalculation of the observed rates that arise from scattering in the spacecraft. We will explore the possibilities of improving this model in future work.

The localization of SGRBs is poorer than long GRBs, with 68% localized within $5°.3–11°.7$ of the true position when humans are involved and $8°.4–14°.1$ in the automated process. The sample is small so these containment radii have large uncertainties. An analysis of the systematic uncertainty on the HitL locations of short bursts finds it is similar to long bursts, suggesting the difference is owed to the poorer statistics associated with fewer counts. Figures 9 and 10 show that the large values may be attributable to outliers and that 50% of both HitL and Ground-Auto localizations of SGRBs are contained within $6°$ of the true location.

FSW locations suffer larger statistical and systematic uncertainties and are useful mainly to assist the LAT on board science algorithms and to initiate repointings of the spacecraft in response to bright GRBs (Figure 2 and Tables 6 and 7). The quality of FSW localizations has significantly declined following the rocking profile change of *Fermi* in 2009 September (Table 8) and we will endeavor to mitigate this deterioration, with enhancements subject to the limitations of on board processing.

Improving the Ground-Auto localization to approach the quality of the HitL localization is a priority, with the first goal to replace the peak flux localizations, which use MAXRATES packets, with fluence localizations using the entire count-rate time series as it arrives in real-time. This should reduce the statistical component to the localization uncertainty on the Ground-Auto positions. Identifying outliers in the automated
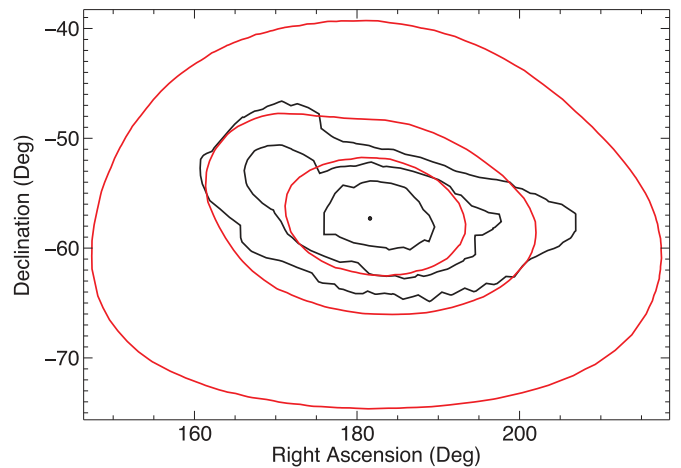


**Figure 11.** $1\sigma$, $2\sigma$, and $3\sigma$ contours for GRB 080714745. The black contours are the statistical uncertainty $\sigma_{stat}$, returned by the localization process. After convolving with the best-fit model for the systematic uncertainty, $\sigma_{sys}$, described in the text as a sum of core-plus-tail Fisher functions with parameters that vary according to the quadrant in which the GRB is localized, the red curves are obtained, $\sigma = \sqrt{(\sigma_{stat}^2 + \sigma_{sys}^2)}$.

process could also help, particularly for the SGRBs, which will not be significantly improved by the implementation of a fluence localization.

The GCN localization notices currently report a 68% confidence-level statistical uncertainty that assumes a circular region around the $\chi^2$ minimum position. In practice, the $\sigma_{stat}$ contours can be elliptical or irregular depending on the $\chi^2$ map returned in the minimization process. We have implemented an algorithm to convolve the $\chi^2$ map with an input systematic uncertainty model to return $1\sigma$, $2\sigma$, and $3\sigma$ contour maps for our localizations. An example is shown in Figure 11. The contours returned by the localization process can be ragged. They are overplotted on the smoothed contours with which the systematic uncertainty, modeled as the sum of two quadrant-dependent Fisher functions described above, has been convolved. As the systematic error is better characterized, and hopefully improved, the model parameters are easily modified to return the contours that best represent the current knowledge of the localization quality. We started delivering these contour maps to the community in 2014 January. They are used regularly by the iPTF team in follow-up observations that have led to the discovery of seven GRB afterglows. The maps are available at the Fermi Science Support Center[14] in ascii, png, and FITS format. Because of the real-time delivery limitations of the GCN and processing and transfer latency to the FSSC, the contours are available at the Fermi Science Support Center from 30 minutes to a couple of hours after the GRB trigger.

---

[14] http://fermi.gsfc.nasa.gov/ssc/data/access/gbm/

## APPENDIX A

### DISTRIBUTIONS OF $\chi^2$ FOR GBM GRB LOCALIZATIONS

A grid of 41,168 possible arrival directions in a spacecraft coordinate system, $1°$ apart, contains the expected count rates in each of the 12 NaI detectors for a burst originating from that direction. The relative count rates in the 12 detectors depend not just on the arrival direction but also on the energy spectrum of the gamma-ray source. Minimizing $\chi^2$ on the grid of 41,168 possible arrival directions based on the observed count rates from a GRB yields the best-fit arrival direction for that assumed spectral shape.

For each of 41,168 positions in the grid, $i$, we find

$$\chi^2(i) = \sum_{j=1}^{12} \frac{[s(j) - b(j) - f(i) * m(j,i)]^2}{b(j) + f(i) * m(j,i)}, \qquad \text{(A1)}$$

where $s(j)$ and $b(j)$ are the total observed and background rates, respectively, observed between 50 and 300 keV in detector $j$; $m(j,i)$ are the model rates in the same energy range for detector $j$ in row $i$; and $f(i)$ is the normalization factor for row $i$ such that

$$f(i) = \frac{\sum_{j=1}^{12} [m(j,i) * (s(j) - b(j))]/s(j)}{\sum_{j=1}^{12} m(j,i)^2/s(j)}. \qquad \text{(A2)}$$

We try three different spectral models representing soft, medium, and hard GRB spectra, as described in Section 2. The direction yielding the lowest $\chi^2$ may vary according to the spectral model, so we obtain up to three possible arrival directions, one for each model. The spectral model returning the lowest $\chi^2$ is assumed to be the better fit to the data and the code therefore selects the position yielding the lowest $\chi^2$ across all three models as the most likely arrival direction for the GRB.

In the reference sample that includes the 203 reference locations from other satellites and the 110 locations from the IPN, the location from the hard spectrum model table is selected 16% of the time, the medium 53% and the soft 31%. The medium and soft GRB spectral models produce the same burst arrival direction for 33% of the sample and only two GRBs are localized to the same grid point under all three spectral models. There are no cases where the hard and soft spectra produce the same $\chi^2$ minimum arrival direction but where those directions are different from those obtained under the assumption of the medium GRB spectrum. The use of three spectral models thus produces different optimal arrival directions for 2/3 of the GRB reference sample. The statistical preference for the soft or medium tables over the hard table or vice versa typically involves tens of units of $\chi^2$ whereas the selection of soft over medium or vice versa typically involves fewer than 20 units of $\chi^2$. Using any of the three models individually for the whole sample results in poorer localizations overall, as determined by both a larger median distance to the true location for the whole sample and a larger value for the systematic error calculated as described in Section 5. This suggests the assumed source spectrum does affect the
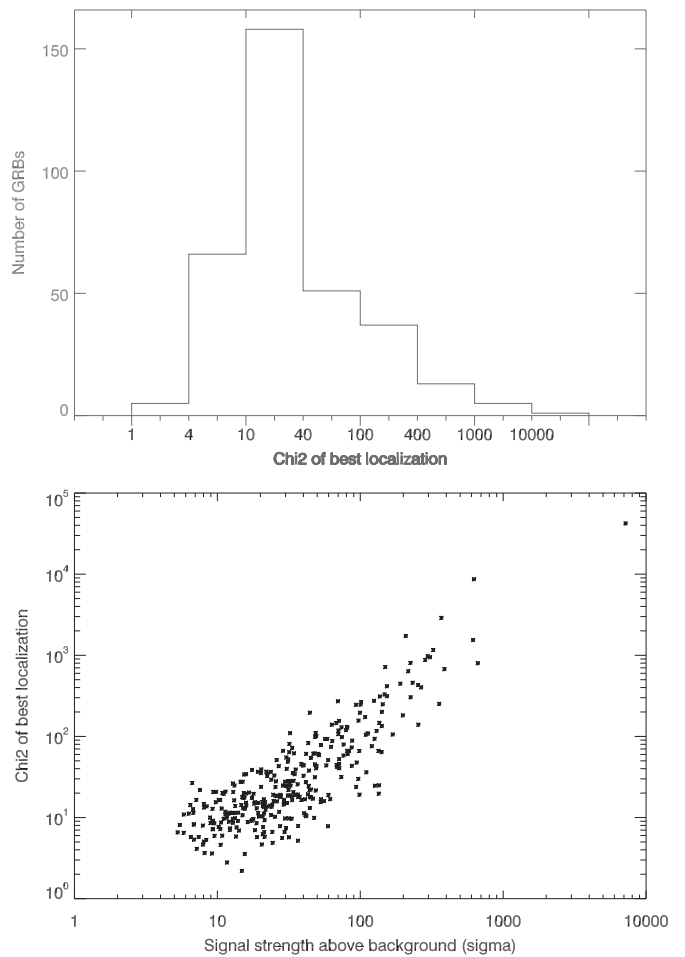


**Figure 12.** Top panel shows the distribution of minimum $\chi^2$ values for the GBM localizations of the sample of GRBs with reference and IPN locations. There is a strong correlation with the intensity of the GRB, as seen in the lower panel which shows the variation of $\chi^2$ with the strength of the data signal used in the minimization.

quality of the localization. We have tried different spectral models, working from the distribution of measured catalog values for Band function parameters (Goldstein et al. 2012; Gruber et al. 2014) but have thus far not obtained a significant improvement relative to the methods and models currently being used that are described in this paper. This was somewhat surprising given that the assumed spectral shapes (particularly the hard spectrum) are extreme compared to the measured spectral shapes. We also expect that because of the scattering of high-energy photons off material in the spacecraft into the 50–300 keV energy range used for the localization process, systematic effects arising from inaccuracies in the spacecraft mass model in our simulations result in spectrally harder bursts being more poorly localized than bursts with a softer spectrum. Quantifying the effect by dividing the GRB sample, for example by hardness ratios or $E_{\text{peak}}$ values, is complicated by the fact that SGRBs are spectrally harder, have lower fluences (and hence larger statistical uncertainties), and are underrepresented in the GRB sample with reference locations. The effects of spectral modeling on source localization are still being explored and will be reported in a future paper.

Localization uncertainties for dim GRBs are dominated by statistics. Bright bursts have low statistical uncertainties and their $\chi^2$ values become larger with increasing intensity as the
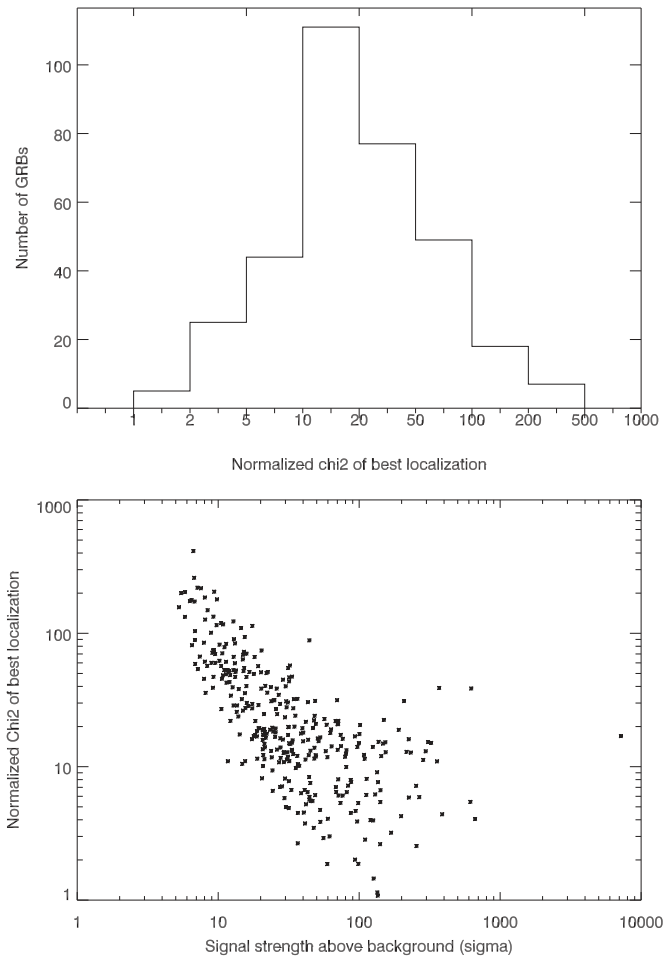
**Figure 13.** Top panel shows the distribution of minimum $\chi^2$ values for the GBM localizations of the sample of GRBs with reference and IPN locations after normalizing the intensity of the GRB (i.e., the observed counts that were used in the minimization) to a fiducial burst of average intensity. The correlation of $\chi^2$ with source signal shown in Figure 12 is reversed (lower panel), with the weaker bursts showing higher values of $\chi^2$, probably because poor fits to the background count rates are magnified in the normalization process and affect the goodness-of-fit of the localization.

goodness of fit is affected by systematics. Figure 12 shows the distribution of minimized $\chi^2$ values for the reference sample and the dependence of this value on the brightness of the GRB, represented by the significance above the background of the data used in the localization. Figure 13 shows the same quantities but with the minimum $\chi^2$ calculated after normalizing the observed data rates to those of a GRB of average intensity (1 photons $cm^{-2}$ $s^{-1}$ between 50 and 300 keV). The dependence of the minimum $\chi^2$ on source intensity disappears for bright GRBs ($>20\sigma$ above background) but the weaker bursts now show higher normalized $\chi^2$ values, probably because the quality of the localization depends more on the quality of the fit to the background data than for brighter GRBs, and systematics due to poor background fitting are magnified by the normalization of the source rates upwards to a GRB of average intensity. In the localization process, we use the normalized $\chi^2$ to assess the goodness-of-fit of the localization, rejecting localizations with normalized $\chi^2$ values above 500 as bad fits. This threshold was found to be efficient in rejecting triggered events due to particle precipitation, which do not have relative detector rates consistent with a point on the sky, without rejecting GRBs with poor localizations. The normalization process does not affect

either the determination of the arrival direction, the spectral model that is selected, or the reported localization uncertainty that is calculated based on observed rather than normalized count rates.

## APPENDIX B

### REFERENCE LOCATIONS

Tables 9–10 show the GRBs that were detected by GBM and by an instrument with localization capability (Table 9) or by the Interplanetary Network (IPN, Table 10). The tables show the GBM localizations that were obtained on board (FSW first and last), in the automated process on the ground (Ground Auto), and in the refined human-in-loop process (HitL). The reference locations and IPN annuli parameters are also given.

## APPENDIX C

### DEPENDENCE OF THE SINGLE-COMPONENT SYSTEMATIC ERROR ON GRB LOCATION IN SPACECRAFT COORDINATE SYSTEM

Results for single-component models exploring the effects of GRB location in the different spacecraft hemispheres and quadrants are shown in Table 11. The first entry in the table repeats the values from Table 2 showing the single Gaussian fits for each localization type. The parameter values and odds ratio for the simplest single component fit can be compared with those for the models that split the GRBs according to position in spacecraft coordinates. GRBs localized with HitL 4.13 in the +Z and +Y hemispheres were found to have a lower systematic error than those in the −Z and −Y hemispheres and separating the sample into hemispheres was slightly preferred over a single component for the whole sky. GRBs in the ±Y quadrants appear to have smaller systematic errors than those in the ±X quadrants, and splitting the GRBs into quadrants is slightly preferred over the all-sky single-component model, but the odds ratio for this model was, however, still much lower than the core-plus-tail model in Table 3. which is thus greatly preferred over any of the single-component models. The odds ratio for these models was, however, still much lower than the core-plus-tail model in Table 3.

## APPENDIX D

### DEPENDENCE OF THE CORE-PLUS-TAIL SYSTEMATIC ERROR MODEL ON GRB SPACECRAFT HEMISPHERE

Results for core-plus-tail models that explore the effect of GRB position in different spacecraft hemispheres are shown in Table 12. The odds ratios for these hemisphere-dependent models should be compared with the simplest all-sky core-plus-tail, repeated from Table 3 as the first entry. Only HitL 4.14g showed a difference from the all-sky core-plus-tail model, with lower parameter values in the +Z hemisphere. By comparing the odds ratios for the two models, we can see that this hemisphere-dependent model is not preferred statistically, but the parameter values are different enough that with a much larger reference sample, this model may become favored over a single core-plus-tail model. HitL 4.13 showed no parameter difference for the core-plus-tail division into Z hemispheres, and the Ground-Auto localization sample failed to converge using this six-parameter model. In general the division into hemispheres produced similar parameters with larger uncertainties; some juggling of events between the core and the tail can account for

**Table 9**
203 Reference Locations for GRBs That Were Also Detected by GBM and Which We Use to Assess the Accuracy of GBM Locations

| Burst Name | Common Name | Trigger Time (UT) | FSW$_{first}$ for Ref. (R.A.) | Decl. | Err) | FSW$_{last}$ for Ref. (R.A.) | Decl. | Err) | Ground Auto for Ref. (R.A.) | Decl. | Err) | HitL for Ref. (R.A.) | Decl. | Err) | Ref. Location (R.A.) | Decl.) | Reference |
|---|---|---|---|---|---|---|---|---|---|---|---|---|---|---|---|---|---|
| 080714745 | GRB 080714A | 17:52:54.03 | ⋯ | ⋯ | ⋯ | ⋯ | ⋯ | ⋯ | 185.3 | −57.7 | 3.8 | 183.5 | −57.5 | 3.9 | 188.1 | −60.2 | Barthelmy et al., GCN 7979 |
| 080723557 | GRB 080723B | 13:22:21.38 | ⋯ | ⋯ | ⋯ | ⋯ | ⋯ | ⋯ | 177.6 | −58.8 | 1.2 | 175.1 | −60.7 | 1.0 | 176.8 | −60.2 | Gotz et al., GCN 8002 |
| 080725435 | GRB 080725A | 10:26:09.06 | ⋯ | ⋯ | ⋯ | ⋯ | ⋯ | ⋯ | 120.2 | −13.4 | 4.1 | 123.1 | −23.1 | 2.2 | 121.7 | −14.0 | Krimm et al., GCN 8014 |
| 080727964 | GRB 080727C | 23:07:46.22 | ⋯ | ⋯ | ⋯ | ⋯ | ⋯ | ⋯ | 43.5 | 59.8 | 4.2 | 40.0 | 62.2 | 2.7 | 32.6 | 64.1 | Fenimore et al., GCN 8044 |
| 080804972 | GRB 080804A | 23:20:14.88 | ⋯ | ⋯ | ⋯ | ⋯ | ⋯ | ⋯ | 324.1 | −52.7 | 3.9 | 320.8 | −52.7 | 2.4 | 328.7 | −53.2 | Markwardt et al., GCN 8067 |
| 080810549 | GRB 080810A | 13:10:12.59 | ⋯ | ⋯ | ⋯ | ⋯ | ⋯ | ⋯ | 358.3 | −5.7 | 5.0 | 355.8 | 5.5 | 2.2 | 356.8 | 0.3 | Sakamoto et al., GCN 8082 |
| 080905499 | GRB 080905A | 11:58:55.04 | ⋯ | ⋯ | ⋯ | ⋯ | ⋯ | ⋯ | 282.5 | −12.0 | 4.3 | 287.0 | −20.0 | 4.1 | 287.7 | −18.9 | Cummings et al., GCN 8187 |
| 080905705 | GRB 080905B | 16:55:46.85 | ⋯ | ⋯ | ⋯ | ⋯ | ⋯ | ⋯ | 291.7 | −56.2 | 6.1 | 307.7 | −62.1 | 5.8 | 301.7 | −62.6 | Barthelmy et al., GCN 8188 |
| 080916009 | GRB 080916C | 00:12:45.62 | ⋯ | ⋯ | ⋯ | ⋯ | ⋯ | ⋯ | 124.3 | −54.3 | 2.5 | 124.4 | −54.7 | 1.4 | 119.8 | −56.6 | Tajima et al., GCN 8246 |
| 080916406 | GRB 080916A | 09:45:18.94 | ⋯ | ⋯ | ⋯ | ⋯ | ⋯ | ⋯ | 334.3 | −57.1 | 3.2 | 335.3 | −56.4 | 2.2 | 336.3 | −57.0 | Baumgartner et al., GCN 8243 |
| 080928628 | GRB 080928A | 15:04:56.05 | ⋯ | ⋯ | ⋯ | ⋯ | ⋯ | ⋯ | 132.3 | −73.7 | 12.5 | 97.8 | −50.0 | 4.0 | 95.1 | −55.2 | Fenimore et al., GCN 8297 |
| 081008832 | GRB 081008A | 19:58:01.80 | 257.9 | −47.6 | 22.8 | 296.9 | −46.2 | 14.4 | 273.1 | −50.9 | 7.2 | 274.4 | −53.8 | 3.4 | 280.0 | −57.5 | Racusin et al., GCN 8344 |
| 081012549 | GRB 081012A | 13:10:23.04 | 22.3 | −32.5 | 17.6 | 28.9 | −25.4 | 11.6 | 36.7 | −12.8 | 7.1 | 27.2 | −11.2 | 5.6 | 30.2 | −17.6 | Sato et al., GCN 8363 |
| 081024245 | GRB 081024A | 05:53:09.01 | 38.4 | 55.2 | 25.3 | 38.4 | 55.2 | 25.3 | 34.3 | 62.5 | 6.2 | 34.3 | 62.5 | 12.8 | 27.9 | 61.3 | Barthelmy et al., GCN 8404 |
| 081024891 | GRB 081024B | 21:22:40.87 | 317.8 | 20.7 | 20.0 | 317.8 | 20.7 | 20.0 | 320.3 | 17.1 | 5.4 | 319.6 | 17.9 | 5.9 | 322.9 | 21.2 | Omodei, GCN 8407 |
| 081025349 | GRB 081025A | 08:23:05.30 | 225.1 | 57.5 | 15.4 | 241.3 | 55.3 | 7.2 | 240.6 | 56.3 | 2.2 | 245.9 | 56.8 | 3.2 | 245.3 | 60.5 | Copete et al., GCN 8409 |
| 081101491 | GRB 081101A | 11:46:32.06 | 93.6 | 10.9 | 14.3 | 93.6 | 10.9 | 14.3 | 89.9 | 0.9 | 13.7 | 80.8 | 11.6 | 10.1 | 95.8 | −0.1 | Barthelmy et al., GCN 8458 |
| 081102739 | GRB 081102A | 17:44:21.60 | 326.8 | 57.8 | 18.9 | 318.8 | 61.6 | 15.8 | 303.6 | 56.1 | 7.8 | 321.3 | 51.9 | 4.5 | 331.2 | 53.0 | Fenimore et al., GCN 8468 |
| 081109293 | GRB 081109A | 07:02:02.42 | 327.6 | −52.4 | 29.3 | 320.8 | −49.6 | 18.0 | 310.7 | −57.3 | 10.6 | 331.5 | −51.9 | 3.5 | 330.8 | −54.7 | Markwardt et al., GCN 8507 |
| 081121858 | GRB 081121A | 20:35:27.76 | 106.9 | −67.4 | 18.1 | 101.4 | −62.4 | 5.8 | 78.1 | −53.3 | 2.9 | 97.2 | −59.9 | 1.1 | 89.3 | −60.6 | Sakamoto et al., GCN 8539 |
| 081126899 | GRB 081126A | 21:34:09.07 | 331.7 | 43.0 | 6.4 | 331.9 | 43.0 | 6.5 | 327.3 | 47.8 | 1.5 | 326.9 | 50.3 | 2.7 | 323.5 | 48.7 | Sato et al., GCN 8557 |
| 081221681 | GRB 081221A | 16:21:12.22 | 21.7 | −19.6 | 11.9 | 18.3 | −21.7 | 4.2 | 14.6 | −23.9 | 1.6 | 14.1 | −25.2 | 1.2 | 15.8 | −24.5 | Cummings et al., GCN 8708 |
| 081222204 | GRB 081222A | 04:54:00.26 | 34.1 | −26.4 | 7.0 | 29.4 | −30.6 | 5.0 | 18.6 | −32.4 | 2.0 | 18.6 | −32.4 | 1.5 | 22.7 | −34.1 | Fenimore et al., GCN 8709 |
| 081226044 | GRB 081226A | 01:03:37.53 | 90.4 | −59.5 | 15.2 | 90.4 | −59.5 | 15.2 | 121.2 | −68.3 | 9.0 | 124.2 | −68.0 | 9.7 | 120.5 | −69.0 | Krimm et al., GCN 8735 |
| 081226509 | GRB 081226B | 12:13:10.71 | 49.4 | −46.2 | 18.5 | 49.4 | −46.2 | 18.5 | 26.4 | −53.3 | 6.9 | 13.5 | −51.6 | 7.8 | 25.5 | −47.4 | Mereghetti et al., GCN 8734 |
| 090102122 | GRB 090102A | 02:55:30.85 | 122.9 | 26.4 | 9.5 | 133.6 | 28.6 | 5.2 | 130.1 | 29.8 | 1.5 | 128.5 | 30.3 | 1.5 | 128.2 | 33.1 | Sakamoto et al., GCN 8769 |
| 090107681 | GRB 090107B | 16:20:42.77 | 161.0 | 86.0 | 26.1 | 288.8 | 47.1 | 9.0 | 287.9 | 51.3 | 6.8 | 285.9 | 53.3 | 11.4 | 284.8 | 59.6 | Gotz et al., GCN 8786 |
| 090113778 | GRB 090113A | 18:40:40.85 | 31.2 | 35.1 | 8.2 | 31.2 | 35.1 | 8.2 | 26.4 | 32.7 | 7.6 | 29.0 | 38.5 | 8.6 | 32.1 | 33.4 | Tueller et al., GCN 8808 |
| 090117640 | GRB 090117A | 15:22:01.06 | 173.9 | −62.7 | 9.1 | 173.9 | −62.7 | 9.1 | 175.0 | −65.3 | 8.0 | 165.1 | −63.2 | 7.0 | 164.0 | −58.2 | Donnarumma et al., GCN 8817 |
| 090129880 | GRB 090129A | 21:07:15.43 | 264.6 | −37.4 | 7.1 | 264.7 | −37.4 | 6.8 | 268.7 | −32.6 | 1.5 | 270.6 | −33.8 | 1.8 | 269.1 | −32.8 | Barthelmy et al., GCN 8862 |
| 090217206 | GRB 090217A | 04:56:42.56 | 210.3 | −2.6 | 8.2 | 207.5 | 1.1 | 4.8 | 207.8 | −5.3 | 1.6 | 211.3 | −11.6 | 1.0 | 204.9 | −8.4 | Ohno et al., GCN 8903 |
| 090323002 | GRB 090323A | 00:02:42.63 | 190.7 | 20.8 | 5.2 | 184.2 | 21.4 | 5.8 | 190.0 | 20.8 | 1.3 | 190.1 | 21.1 | 1.2 | 190.7 | 17.1 | Ohno et al., GCN 9021 |
| 090328401 | GRB 090328A | 09:36:46.52 | 79.3 | −46.7 | 26.3 | 80.0 | −45.6 | 5.3 | 95.0 | −44.5 | 2.1 | 95.9 | −45.1 | 1.0 | 90.9 | −42.0 | McEnery et al., GCN 9044 |
| 090422150 | GRB 090422A | 03:35:17.07 | 296.9 | 36.1 | 18.4 | 296.9 | 36.1 | 18.4 | 297.7 | 42.1 | 8.5 | 296.3 | 33.2 | 10.3 | 294.7 | 40.4 | Markwardt et al., GCN 9195 |
| 090423330 | GRB 090423A | 07:55:25.40 | 151.3 | 11.0 | 31.9 | 151.3 | 11.0 | 31.9 | 144.5 | 9.1 | 50.0 | 154.9 | 13.5 | 11.2 | 148.9 | 18.2 | Palmer et al., GCN 9204 |
| 090424592 | GRB 090424A | 14:12:08.67 | 177.4 | 8.0 | 3.5 | 177.3 | 7.8 | 3.6 | 191.4 | 18.0 | 1.0 | 191.5 | 18.1 | 1.6 | 189.5 | 16.8 | Sakamoto et al., GCN 9231 |
| 090509215 | GRB 090509A | 05:10:05.72 | 220.2 | −36.7 | 26.0 | 241.9 | −28.8 | 15.5 | 237.5 | −27.7 | 10.1 | 230.1 | −27.7 | 5.7 | 241.4 | −28.4 | Tueller et al., GCN 9335 |
| 090510016 | GRB 090510A | 00:22:59.98 | 340.8 | −33.3 | 4.0 | 340.8 | −33.3 | 4.0 | 335.1 | −31.3 | 1.3 | 335.0 | −31.3 | 1.0 | 333.6 | −26.6 | Ukwatta et al., GCN 9337 |
| 090516353 | GRB 090516A | 08:27:58.35 | 139.4 | −10.7 | 24.9 | 139.5 | −0.5 | 15.0 | 141.6 | −12.8 | 7.9 | 138.5 | −14.8 | 1.1 | 138.2 | −11.9 | Baumgartner et al., GCN 9384 |
| 090518080 | GRB 090518A | 01:54:44.52 | 122.5 | 13.6 | 14.9 | 122.5 | 13.6 | 14.9 | 123.5 | 4.2 | 10.5 | 112.5 | 1.2 | 8.1 | 119.9 | 0.8 | Cummings et al., GCN 9393 |
| 090519881 | GRB 090519A | 21:08:45.88 | 142.2 | 3.1 | 20.6 | 142.2 | 3.1 | 20.6 | 140.3 | 0.9 | 8.5 | 139.8 | −5.4 | 5.2 | 142.3 | 0.2 | Krimm et al., GCN 9406 |
| 090531775 | GRB 090531B | 18:35:56.50 | 250.0 | −43.8 | 7.3 | 250.0 | −43.8 | 7.3 | 254.0 | −35.4 | 5.0 | 252.9 | −31.5 | 7.2 | 252.1 | −36.0 | Cummings et al., GCN 9461 |
| 090618353 | GRB 090618A | 08:28:26.66 | 304.6 | 52.9 | 7.0 | 296.2 | 77.1 | 3.5 | 295.1 | 80.8 | 1.0 | 288.4 | 80.0 | 1.0 | 294. | 78.4 | Baumgartner et al., GCN 9530 |
| 090621185 | GRB 090621A | 04:26:34.49 | 12.7 | 44.1 | 21.1 | 3.4 | 61.2 | 14.3 | 3.6 | 60.8 | 5.4 | 8.7 | 60.8 | 2.4 | 11.0 | 61.9 | Cummings et al., GCN 9546 |

**Table 9**
(Continued)

| Burst Name | Common Name | Trigger Time | FSW$_{first}$ for Ref. | | | FSW$_{last}$ for Ref. | | | Ground Auto for Ref. | | | HitL for Ref. | | | Ref. Location | | Reference |
|---|---|---|---|---|---|---|---|---|---|---|---|---|---|---|---|---|---|
| | | (UT) | (R.A. | Decl. | Err) | (R.A. | Decl. | Err) | (R.A. | Decl. | Err) | (R.A. | Decl. | Err) | (R.A. | Decl.) | |
| 090621922 | GRB 090621B | 22:07:25.71 | 341.4 | 63.9 | 14.7 | 341.4 | 63.9 | 14.7 | 348.1 | 67.9 | 7.9 | 320.7 | 68.9 | 9.1 | 313.4 | 69.0 | Krimm et al., GCN 9551 |
| 090625560 | GRB 090625B | 13:26:22.52 | 19.4 | −64.6 | 29.1 | 16.3 | −59.8 | 13.5 | 0.1 | −65.1 | 6.7 | 359.8 | −69.2 | 5.2 | 2.3 | −65.8 | Gotz et al., GCN 9572 |
| 090626189 | GRB 090626A | 04:32:08.89 | 170.0 | −36.6 | 4.8 | 170.6 | −35.5 | 3.9 | 169.9 | −35.3 | 1.0 | 169.6 | −35.8 | 1.0 | 170.0 | −33.5 | Piron et al., GCN 9584 |
| 090704242 | GRB 090704A | 05:47:48.19 | 211.4 | 4.5 | 22.9 | 214.8 | 17.7 | 11.9 | 213.6 | 25.3 | 6.7 | 207.9 | 25.3 | 2.7 | 208.2 | 22.8 | Mereghetti et al., GCN 9620 |
| 090708152 | GRB 090708A | 03:38:18.46 | 150.5 | 22.8 | 27.0 | 150.5 | 22.8 | 27.0 | 140.8 | 21.0 | 16.6 | 150.8 | 24.2 | 13.6 | 154.6 | 26.6 | Palmer et al., GCN 9623 |
| 090709630 | GRB 090709B | 15:07:41.14 | 76.6 | 64.3 | 19.4 | 65.4 | 66.8 | 9.9 | 60.4 | 65.7 | 4.8 | 88.5 | 63.8 | 6.6 | 93.5 | 64.1 | Ukwatta et al., GCN 9641 |
| 090712160 | GRB 090712A | 03:51:00.35 | 79.9 | 14.1 | 34.8 | 79.9 | 14.1 | 34.8 | 55.0 | 22.4 | 26.2 | 72.8 | 20.2 | 5.6 | 70.1 | 22.5 | Barthelmy et al., GCN 9660 |
| 090813174 | GRB 090813A | 04:10:42.60 | 247.2 | 82.7 | 4.7 | 246.9 | 82.7 | 6.3 | 91.4 | 84.7 | 2.1 | 40.2 | 86.0 | 5.1 | 225.1 | 88.6 | Cummings et al., GCN 9788 |
| 090817036 | GRB 090817A | 00:51:26.21 | 88.2 | 53.3 | 9.7 | 67.2 | 45.8 | 8.1 | 65.1 | 39.2 | 3.6 | 64.0 | 40.8 | 3.3 | 64.0 | 44.1 | Evans et al., GCN 9819 |
| 090902462 | GRB 090902B | 11:05:08.32 | 262.6 | 29.7 | 4.8 | 266.4 | 33.9 | 3.5 | 261.4 | 26.0 | 1.0 | 261.4 | 26.1 | 1.0 | 264.9 | 27.3 | De Palma et al., GCN 9867 |
| 090904058 | GRB 090904B | 01:24:13.94 | 257.4 | −24.1 | 26.4 | 266.8 | −17.9 | 10.1 | 266.6 | −27.5 | 4.1 | 265.9 | −30.1 | 1.9 | 264.2 | −25.2 | Sakamoto et al., GCN 9890 |
| 090912660 | GRB 090912A | 15:50:29.11 | 236.2 | 27.5 | 20.0 | 212.7 | 32.3 | 25.6 | 212.8 | 41.8 | 18.4 | 178.5 | 66.0 | 5.1 | 188.0 | 61.5 | Ukwatta et al., GCN 9909 |
| 090915650 | GRB 090915A | 15:35:35.66 | 237.7 | 33.1 | 15.4 | 237.7 | 33.1 | 15.4 | 250.1 | 23.8 | 6.5 | 243.8 | 9.9 | 3.7 | 238.0 | 15.5 | Cummings et al., GCN 9912 |
| 090926181 | GRB 090926A | 04:20:26.99 | 1.3 | −66.1 | 6.2 | 350.0 | −63.3 | 3.5 | 354.4 | −64.3 | 1.0 | 350.1 | −63.5 | 1.0 | 353.4 | −66.3 | Uehara et al., GCN 9934 |
| 090926914 | GRB 090926B | 21:55:28.53 | 38.2 | −31.0 | 30.7 | 26.2 | −31.7 | 9.5 | 28.2 | −32.5 | 3.5 | 44.3 | −43.9 | 2.4 | 46.3 | −39.0 | Grupe et al., GCN 9935 |
| 090927422 | GRB 090927A | 10:07:17.22 | 61.7 | −68.2 | 18.7 | 61.7 | −68.2 | 18.7 | 60.5 | −65.9 | 12.3 | 67.6 | −67.6 | 12.1 | 344.0 | −71.0 | Grupe et al., GCN 9945 |
| 091003191 | GRB 091003A | 04:35:45.59 | 253.1 | 39.6 | 5.1 | 247.7 | 38.2 | 3.7 | 251.6 | 37.3 | 1.0 | 251.2 | 37.3 | 1.0 | 251.5 | 36.6 | McEnery et al., GCN 9985 |
| 091010113 | GRB 091010A | 02:43:09.33 | 299.9 | −21.2 | 3.6 | 300.0 | −21.3 | 3.5 | 291.1 | −23.9 | 1.1 | 293.4 | −23.8 | 1.2 | 298.7 | −22.5 | Donnarumma et al., GCN 10004 |
| 091020900 | GRB 091020A | 21:36:43.82 | 138.1 | 67.2 | 14.8 | 149.6 | 75.7 | 5.8 | 172.3 | 63.7 | 3.4 | 174.4 | 52.7 | 3.1 | 175.7 | 51.0 | Palmer et al., GCN 10051 |
| 091024372 | GRB 091024A | 08:55:58.48 | 337.8 | 27.9 | 25.0 | 78.8 | 46.0 | 8.3 | 356.9 | 56.7 | 10.2 | 340.5 | 55.1 | 2.0 | 339.2 | 56.9 | Sakamoto et al., GCN 10072 |
| 091024380 | GRB 091024A | 09:06:29.36 | 338.8 | 55.5 | 19.8 | 28.7 | 70.5 | 14.6 | 346.7 | 53.8 | 3.4 | 336.4 | 55.9 | 1.0 | 339.2 | 56.9 | Sakamoto et al., GCN 10072 |
| 091026550 | GRB 091026A | 13:11:33.02 | 34.8 | −83.7 | 17.7 | 34.8 | −83.7 | 17.7 | 26.3 | −84.7 | 6.3 | 116.3 | −88.3 | 7.4 | 276.6 | −86.1 | Ukwatta et al., GCN 10089 |
| 091031500 | GRB 091031A | 12:00:28.85 | 71.2 | −56.2 | 10.7 | 76.3 | −63.3 | 5.6 | 69.7 | −57.6 | 1.6 | 70.5 | −59.0 | 1.1 | 71.7 | −57.5 | de Palma et al., GCN 10163 |
| 091102607 | GRB 091102A | 14:34:38.37 | 349.9 | −68.7 | 16.8 | 49.7 | −63.8 | 15.0 | 62.7 | −68.3 | 5.5 | 67.0 | −73.4 | 1.5 | 72.6 | −72.5 | Baumgartner et al., GCN 10121 |
| 091112737 | GRB 091112A | 17:41:15.83 | 249.7 | −42.5 | 21.1 | 252.7 | −47.8 | 10.0 | 258.3 | −41.3 | 6.5 | 258.3 | −36.7 | 3.2 | 257.7 | −36.7 | Palmer et al., GCN 10165 |
| 091120191 | GRB 091120A | 04:34:40.23 | 225.1 | −19.9 | 11.4 | 225.1 | −19.9 | 11.4 | 224.3 | −26.9 | 2.9 | 225.4 | −26.1 | 1.2 | 226.8 | −21.8 | Nakajima et al., GCN 10188 |
| 091127976 | GRB 091127A | 23:25:45.49 | 41.4 | −27.6 | 3.8 | 36.8 | −32.2 | 4.6 | 36.0 | −21.9 | 1.2 | 38.1 | −21.0 | 1.1 | 36.6 | −19.0 | Stamatikos et al., GCN 10197 |
| 091208410 | GRB 091208B | 09:49:57.96 | 28.6 | 24.9 | 8.7 | 28.5 | 25.2 | 4.7 | 29.3 | 14.2 | 2.7 | 30.1 | 13.5 | 2.6 | 29.4 | 16.9 | Baumgartner et al., GCN 10265 |
| 091221870 | GRB 091221A | 20:52:57.22 | 39.1 | 26.6 | 30.6 | 39.8 | 20.6 | 7.4 | 60.8 | 20.4 | 2.1 | 54.5 | 27.3 | 1.2 | 55.8 | 23.2 | Cummings et al., GCN 10291 |
| 100111176 | GRB 100111A | 04:12:49.70 | 239.7 | 12.3 | 12.3 | 239.7 | 12.3 | 12.3 | 239.9 | 12.0 | 4.3 | 246.0 | 16.0 | 3.9 | 247. | 15.5 | Krimm et al., GCN 10322 |
| 100116897 | GRB 100116A | 21:31:00.25 | 300.0 | 12.3 | 13.5 | 300.0 | 12.3 | 13.5 | 307.0 | 26.0 | 3.1 | 308.4 | 22.7 | 1.2 | 305.0 | 14.5 | McEnery et al., GCN 10333 |
| 100117879 | GRB 100117A | 21:06:19.67 | 6.1 | −6.2 | 11.9 | 6.1 | −6.2 | 11.9 | 9.9 | 8.3 | 5.7 | 11.2 | 9.0 | 5.8 | 11.3 | −1.6 | Markwardt et al., GCN 10338 |
| 100206563 | GRB 100206A | 13:30:05.40 | 44.7 | 17.6 | 11.5 | 44.7 | 17.6 | 11.5 | 74.6 | 22.7 | 3.0 | 63.9 | 13.9 | 4.5 | 47.2 | 13.2 | Sakamoto et al., GCN 10379 |
| 100212588 | GRB 100212A | 14:07:22.30 | 7.3 | 48.7 | 10.6 | 7.3 | 48.7 | 10.6 | 4.7 | 45.5 | 4.8 | 2.9 | 44.8 | 4.3 | 356.4 | 49.5 | Ukwatta et al., GCN 10404 |
| 100216422 | GRB 100216A | 10:07:00.19 | 148.9 | 46.4 | 17.0 | 148.9 | 46.4 | 17.0 | 157.7 | 49.0 | 7.6 | 155.5 | 47.4 | 8.7 | 154.3 | 35.5 | Cummings et al., GCN 10428 |
| 100225115 | GRB 100225A | 02:45:31.15 | 310.2 | −60.7 | 21.3 | 302.3 | −67.9 | 10.4 | 319.8 | −56.3 | 4.5 | 312.4 | −54.7 | 3.3 | 310.3 | −59.4 | Piron et al., GCN 10450 |
| 100325275 | GRB 100325A | 06:36:08.03 | 327.2 | −23.9 | 6.5 | 327.2 | −23.9 | 6.9 | 329.1 | −27.3 | 1.7 | 331.3 | −28.1 | 2.0 | 330.2 | −26.5 | de Palma et al., GCN 10548 |
| 100401297 | GRB 100401A | 07:07:32.25 | 284.6 | −25.8 | 19.0 | 284.6 | −25.8 | 19.0 | 282.8 | −26.9 | 9.5 | 290.0 | −16.3 | 7.9 | 290.8 | −8.3 | Cummings et al., GCN 10567 |
| 100413732 | GRB 100413A | 17:33:31.93 | 237.9 | −7.6 | 25.6 | 237.9 | −7.6 | 25.6 | 245.9 | −1.4 | 18.0 | 273.3 | 17.2 | 5.4 | 266.2 | 15.8 | Stamatikos et al., GCN 10585 |
| 100414097 | GRB 100414A | 02:20:21.99 | 183.6 | 20.5 | 11.2 | 186.2 | 15.4 | 4.2 | 194.0 | 9.8 | 1.1 | 185.7 | 15.7 | 1.0 | 192.1 | 8.7 | Page et al., GCN 10601 |
| 100427356 | GRB 100427A | 08:32:08.71 | 95.3 | −4.0 | 10.2 | 95.4 | −3.9 | 7.8 | 94.5 | −3.5 | 3.4 | 91.0 | −1.4 | 2.6 | 89.2 | −3.5 | Cummings et al., GCN 10699 |
| 100504806 | GRB 100504A | 19:20:55.54 | 250.4 | −18.3 | 28.0 | 250.9 | −33.6 | 20.3 | 246.2 | −31.7 | 10.4 | 254.8 | −34.7 | 5.1 | 255.6 | −35.6 | Palmer et al., GCN 10716 |
| 100510810 | GRB 100510A | 19:27:06.97 | 74.5 | −35.8 | 15.6 | 345.1 | −20.0 | 18.4 | 30.1 | −28.6 | 20.6 | 347.1 | −21.1 | 4.2 | 355.8 | −35.6 | Morii et al., GCN 10739 |
| 100522157 | GRB 100522A | 03:45:52.30 | 10.2 | 10.2 | 5.6 | 10.2 | 10.2 | 5.6 | 13.1 | 11.5 | 1.8 | 8.0 | 10.5 | 3.9 | 7.0 | 9.4 | Barthelmy et al., GCN 10788 |

**Table 9**
(Continued)

| Burst Name | Common Name | Trigger Time (UT) | FSW_first for Ref. (R.A.) | (Decl.) | (Err) | FSW_last for Ref. (R.A.) | (Decl.) | (Err) | Ground Auto for Ref. (R.A.) | (Decl.) | (Err) | HitL for Ref. (R.A.) | (Decl.) | (Err) | Ref. Location (R.A.) | (Decl.) | Reference |
|---|---|---|---|---|---|---|---|---|---|---|---|---|---|---|---|---|---|
| 100528075 | GRB 100528A | 01:48:01.11 | 315.5 | 37.8 | 15.5 | 307.1 | 30.1 | 5.4 | 326.8 | 34.3 | 1.0 | 310.7 | 26.8 | 1.2 | 311.1 | 27.8 | Del Monte et al., GCN 10810 |
| 100615083 | GRB 100615A | 01:59:04.38 | 165.4 | −23.7 | 7.4 | 165.5 | −23.7 | 7.6 | 176.7 | −20.6 | 3.8 | 175.6 | −21.1 | 2.4 | 177.2 | −19.5 | Palmer et al., GCN 10850 |
| 100619015 | GRB 100619A | 00:21:07.03 | 81.3 | −20.2 | 16.5 | 86.6 | −22.3 | 9.9 | 86.3 | −25.3 | 4.2 | 84.0 | −25.5 | 6.6 | 84.6 | −27.0 | Stamatikos et al., GCN 10864 |
| 100625773 | GRB 100625A | 18:32:28.48 | 16.3 | −50.0 | 4.8 | 16.3 | −50.0 | 4.8 | 21.9 | −38.1 | 2.6 | 21.9 | −38.1 | 3.9 | 15.8 | −39.1 | Barthelmy et al., GCN 10891 |
| 100701490 | GRB 100701B | 11:45:23.07 | 13.4 | −35.3 | 4.9 | 19.1 | −33.1 | 3.8 | 45.1 | 2.6 | 2.3 | 47.2 | −3.5 | 1.1 | 43.1 | −2.2 | Golenetskii et al., GCN 10938 |
| 100704149 | GRB 100704A | 03:35:06.11 | 139.6 | −23.5 | 11.2 | 152.4 | −12.2 | 6.4 | 136.6 | −19.7 | 2.2 | 133.2 | −23.6 | 1.6 | 133.6 | −24.2 | Cummings et al., GCN 10932 |
| 100724029 | GRB 100724A | 00:42:06.00 | 154.4 | 84.5 | 16.2 | 131.6 | 85.0 | 4.4 | 128.8 | 70.9 | 1.2 | 116.8 | 73.5 | 1.0 | 120.0 | 76.7 | Tanaka et al., GCN 10978 |
| 100725475 | GRB 100725B | 11:24:34.90 | 297.1 | 74.3 | 17.0 | 248.4 | 76.2 | 10.0 | 285.4 | 77.6 | 2.3 | 280.5 | 73.5 | 2.2 | 290.0 | 77.0 | Sakamoto et al., GCN 10993 |
| 100727238 | GRB 100727A | 05:42:22.00 | 142.6 | −10.1 | 34.6 | 142.6 | −10.1 | 34.6 | 142.6 | −8.2 | 12.2 | 154.6 | −9.8 | 11.1 | 154.2 | −21.4 | Stamatikos et al., GCN 11001 |
| 100728095 | GRB 100728A | 02:17:30.62 | 77.1 | −14.3 | 35.1 | 78.1 | −23.4 | 8.6 | 91.3 | −16.9 | 1.7 | 88.3 | −13.7 | 1.0 | 88.8 | −15.3 | Ukwatta et al., GCN 11018 |
| 100728439 | GRB 100728B | 10:31:54.98 | 55.3 | 0.3 | 12.9 | 51.6 | 3.2 | 9.5 | 42.5 | 2.1 | 4.9 | 41.5 | 0.2 | 4.2 | 44.1 | 0.3 | Barthelmy et al., GCN 11023 |
| 100802240 | GRB 100802A | 05:45:35.68 | 5.2 | 43.0 | 18.0 | 5.2 | 43.0 | 18.0 | 0.7 | 44.9 | 7.8 | 4.6 | 43.9 | 6.8 | 2.5 | 47.8 | Baumgartner et al., GCN 11035 |
| 100814160 | GRB 100814A | 03:50:08.81 | 25.1 | −1.2 | 12.0 | 19.1 | −10.4 | 7.5 | 20.0 | −16.4 | 3.4 | 19.8 | −15.4 | 2.5 | 22.5 | −18.0 | Krimm et al., GCN 11094 |
| 100816026 | GRB 100816A | 00:37:50.95 | ⋯ | ⋯ | ⋯ | 90.3 | −23.0 | 11.1 | 347.5 | 25.4 | 2.2 | 346.4 | 25.5 | 1.9 | 351.7 | 26.6 | Markwardt et al., GCN 11111 |
| 100906576 | GRB 100906A | 13:49:27.63 | 129.7 | 53.3 | 4.2 | 30.3 | 51.9 | 5.6 | 27.3 | 57.1 | 1.6 | 28.0 | 55.2 | 1.1 | 28.7 | 55.6 | Mereghetti et al., GCN 11233 |
| 100915243 | GRB 100915B | 05:49:39.62 | 84.7 | 22.9 | 25.4 | 84.7 | 22.9 | 25.4 | 86.8 | 18.3 | 16.4 | 86.8 | 18.3 | 12.7 | 85.4 | 25.1 | Mereghetti et al., GCN 11278 |
| 100924165 | GRB 100924A | 03:58:08.32 | 3.5 | 28.2 | 9.9 | 3.5 | 28.2 | 9.9 | 7.2 | 8.7 | 4.0 | 6.9 | 9.7 | 4.0 | 0.7 | 7.0 | Barthelmy et al., GCN 11295 |
| 101008697 | GRB 101008A | 16:43:15.61 | 324.8 | 34.0 | 13.2 | 324.8 | 34.0 | 13.2 | 335.0 | 31.7 | 8.6 | 326.9 | 36.7 | 8.5 | 328.9 | 37.1 | Barthelmy et al., GCN 11327 |
| 101011707 | GRB 101011A | 16:58:36.54 | 17.7 | −78.2 | 9.7 | 17.7 | −78.2 | 9.7 | 31.1 | −61.7 | 11.3 | 33.4 | −75.9 | 6.4 | 48.3 | −66.0 | Markwardt et al., GCN 11332 |
| 101023951 | GRB 101023A | 22:50:04.73 | 15.5 | −67.7 | 22.4 | 354.7 | −60.6 | 3.7 | 320.6 | −67.3 | 1.0 | 315.5 | −66.5 | 1.0 | 318.0 | −65.4 | Stamatikos et al., GCN 11367 |
| 101024486 | GRB 101024A | 11:39:33.61 | 157.5 | −70.9 | 19.2 | 157.5 | −70.9 | 19.2 | 144.5 | −84.0 | 6.5 | 147.1 | −77.2 | 9.6 | 66.5 | −77.3 | Ukwatta et al., GCN 11374 |
| 101030664 | GRB 101030A | 15:56:30.72 | 177.1 | −35.3 | 31.3 | 177.1 | −35.3 | 31.3 | 166.9 | −23.1 | 21.7 | 169.5 | −16.0 | 7.4 | 166.4 | −16.4 | Barthelmy et al., GCN 11388 |
| 101112924 | GRB 101112A | 22:10:32.45 | 299.7 | 42.8 | 8.2 | 299.7 | 42.8 | 8.2 | 300.5 | 39.8 | 3.5 | 299.3 | 39.4 | 4.2 | 292.2 | 39.3 | Gotz et al., GCN 11396 |
| 101201418 | GRB 101201A | 10:01:49.75 | 1.6 | −2.4 | 14.4 | 358.2 | −6.2 | 7.2 | 0.3 | −15.3 | 2.7 | 3.9 | −14.7 | 1.6 | 1.9 | −16.1 | Cummings et al., GCN 11429 |
| 101213451 | GRB 101213A | 10:49:20.80 | 246.9 | 10.9 | 19.6 | 237.7 | 19.3 | 11.1 | 238.7 | 16.8 | 6.1 | 247.3 | 21.2 | 3.6 | 241.3 | 21.9 | Cummings et al., GCN 11453 |
| 101219686 | GRB 101219B | 16:28:13.13 | 9.3 | −39.2 | 23.8 | 9.3 | −39.2 | 23.8 | 17.2 | −31.0 | 8.4 | 11.1 | −31.1 | 3.4 | 12.3 | −34.6 | Cummings et al., GCN 11475 |
| 101224227 | GRB 101224A | 05:27:13.87 | 303.9 | 1.6 | 21.6 | 303.9 | 1.6 | 21.6 | 306.8 | 27.2 | 18.7 | 300.3 | 40.4 | 13.5 | 285.9 | 45.7 | Markwardt et al., GCN 11486 |
| 110102788 | GRB 110102A | 18:54:36.01 | 249.3 | −3.5 | 10.1 | 249.2 | −3.7 | 5.6 | 245.2 | 5.5 | 1.7 | 246.2 | 6.0 | 2.0 | 245.9 | 7.6 | Sakamoto et al., GCN 11511 |
| 110106893 | GRB 110106B | 21:26:16.08 | 197.9 | 31.8 | 27.3 | 197.9 | 31.8 | 27.3 | 171.3 | 37.7 | 10.0 | 155.3 | 38.6 | 9.3 | 134.2 | 47.0 | Ukwatta et al., GCN 11533 |
| 110112934 | GRB 110112B | 22:24:55.30 | 21.6 | 44.5 | 9.7 | 21.6 | 44.5 | 9.7 | 25.8 | 42.8 | 5.8 | 25.9 | 44.0 | 4.7 | 10.6 | 64.4 | Mereghetti et al., GCN 11562 |
| 110119931 | GRB 110119A | 22:21:00.17 | ⋯ | ⋯ | ⋯ | 359.6 | −1.6 | 9.8 | 349.6 | 6.0 | 4.4 | 345.4 | 8.0 | 2.5 | 348.6 | 6.0 | Baumgartner et al., GCN 11584 |
| 110120666 | GRB 110120A | 15:59:39.23 | 65.1 | −22.6 | 5.3 | 65.6 | −23.0 | 4.9 | 65.7 | −18.3 | 1.0 | 64.8 | −16.8 | 1.1 | 61.6 | −12.0 | Omodei et al., GCN 11597 |
| 110128073 | GRB 110128A | 01:44:36.44 | 207.5 | 7.3 | 27.5 | 207.5 | 7.3 | 27.5 | 202.7 | 22.3 | 14.0 | 204.4 | 19.7 | 11.4 | 193.9 | 28.1 | Cummings et al., GCN 11614 |
| 110201399 | GRB 110201A | 09:35:10.26 | 177.3 | 59.8 | 11.3 | 177.3 | 59.8 | 11.3 | 164.8 | 84.4 | 6.5 | 166.3 | 87.4 | 4.6 | 137.6 | 88.6 | Krimm et al., GCN 11624 |
| 110207470 | GRB 110207A | 11:17:20.29 | 14.3 | −12.3 | 13.4 | 14.3 | −12.3 | 13.4 | 359.5 | 4.7 | 13.4 | 15.7 | −10.0 | 5.5 | 12.5 | −10.8 | Palmer et al., GCN 11664 |
| 110213220 | GRB 110213A | 05:17:11.28 | 46.0 | 49.3 | 28.9 | 39.2 | 39.3 | 7.2 | 49.2 | 52.5 | 2.6 | 49.0 | 52.8 | 2.3 | 43.0 | 49.3 | Barthelmy et al., GCN 11714 |
| 110318552 | GRB 110318A | 13:14:16.71 | 327.6 | −35.1 | 30.0 | 343.7 | −27.8 | 5.9 | 336.3 | −16.4 | 2.6 | 335.9 | −14.9 | 1.9 | 338.3 | −15.3 | Barthelmy et al., GCN 11802 |
| 110402009 | GRB 110402A | 00:12:58.55 | 189.0 | 65.0 | 19.8 | 182.1 | 54.5 | 4.5 | 190.2 | 57.2 | 4.1 | 187.7 | 58.7 | 2.2 | 197.4 | 61.3 | Stamatikos et al., GCN 11866 |
| 110412315 | GRB 110412A | 07:33:35.71 | 110.5 | 21.3 | 28.4 | 130.4 | 14.4 | 14.6 | 114.6 | 16.6 | 7.9 | 135.9 | 11.4 | 3.8 | 133.5 | 13.5 | Baumgartner et al., GCN 11929 |
| 110420946 | GRB 110420B | 22:42:11.74 | 311.3 | −44.9 | 16.6 | 311.3 | −44.9 | 16.6 | 350.0 | −28.8 | 26.7 | 326.4 | −39.3 | 12.2 | 320.1 | −41.3 | Markwardt et al., GCN 11946 |
| 110428388 | GRB 110428A | 09:18:30.41 | ⋯ | ⋯ | ⋯ | 128.9 | 12.8 | 6.1 | 0.5 | 62.4 | 1.0 | 2.1 | 61.7 | 1.0 | 5.3 | 64.8 | Vasileiou et al., GCN 11982 |
| 110610640 | GRB 110610A | 15:21:32.55 | 313.8 | 76.6 | 17.4 | 317.2 | 78.9 | 6.4 | 310.0 | 77.6 | 2.3 | 306.5 | 75.9 | 2.6 | 308.2 | 74.8 | Marshall et al., GCN 12065 |
| 110625881 | GRB 110625A | 21:08:18.24 | 298.0 | 6.7 | 14.1 | 348.4 | 54.6 | 3.4 | 287.8 | 6.9 | 1.0 | 287.7 | 6.7 | 1.0 | 286.8 | 6.8 | Page et al., GCN 12088 |
| 110709642 | GRB 110709A | 15:24:27.37 | 239.9 | 44.6 | 5.4 | 239.9 | 44.6 | 5.2 | 240.4 | 39.9 | 1.5 | 241.2 | 41.8 | 1.1 | 238.9 | 40.9 | Holland et al., GCN 12118 |

**Table 9**
(Continued)

| Burst Name | Common Name | Trigger Time (UT) | FSW_first for Ref. (R.A.) | Decl. | Err) | FSW_last for Ref. (R.A.) | Decl. | Err) | Ground Auto for Ref. (R.A.) | Decl. | Err) | HitL for Ref. (R.A.) | Decl. | Err) | Ref. Location (R.A.) | Decl.) | Reference |
|---|---|---|---|---|---|---|---|---|---|---|---|---|---|---|---|---|---|
| 110721200 | GRB 110721A | 04:47:43.77 | 327.6 | −37.9 | 3.9 | 323.6 | −33.4 | 3.8 | 331.4 | −36.6 | 1.0 | 331.4 | −36.6 | 1.0 | 333.4 | −39.0 | Vasileiou et al., GCN 12188 |
| 110731465 | GRB 110731A | 11:09:29.96 | 281.8 | −38.9 | 4.3 | 282.0 | −39.0 | 4.4 | 281.1 | −26.6 | 3.4 | 283.1 | −34.0 | 1.0 | 280.5 | −28.5 | Oates et al., GCN 12215 |
| 110818860 | GRB 110818A | 20:37:54.23 | 140.4 | −73.3 | 28.4 | 140.4 | −73.3 | 28.4 | 338.4 | −55.7 | 10.0 | 329.6 | −54.1 | 4.1 | 317.4 | −64.0 | Markwardt et al., GCN 12279 |
| 110825102 | GRB 110825A | 02:26:50.94 | 42.4 | 6.5 | 26.9 | 48.8 | 17.3 | 3.7 | 47.1 | 14.6 | 1.0 | 47.1 | 14.6 | 1.0 | 44.8 | 15.4 | Zhang et al., GCN 12308 |
| 110903111 | GRB 110903A | 02:39:34.43 | 195.7 | 63.3 | 8.8 | 208.1 | 65.5 | 6.5 | 199.1 | 52.7 | 3.8 | 196.0 | 51.8 | 2.6 | 197.1 | 59.0 | Mereghetti et al., GCN 12322 |
| 110921577 | GRB 110921A | 13:51:22.58 | 296.6 | 47.9 | 18.5 | 296.6 | 47.9 | 18.5 | 297.1 | 41.9 | 6.2 | 297.9 | 33.7 | 3.9 | 294.1 | 36.4 | Baumgartner et al., GCN 12373 |
| 111103441 | GRB 111103A | 10:35:13.40 | 330.7 | −3.6 | 9.1 | 330.7 | −3.6 | 9.1 | 331.2 | −9.7 | 4.1 | 327.0 | −10.0 | 1.8 | 327.1 | −10.5 | Stroh et al., GCN 12518 |
| 111107035 | GRB 111107A | 00:50:25.49 | 152.3 | −63.3 | 17.9 | 152.3 | −63.3 | 17.9 | 141.6 | −65.3 | 5.7 | 149.0 | −66.0 | 6.0 | 129.5 | −66.5 | Siegel et al., GCN 12534 |
| 111117510 | GRB 111117A | 12:13:42.03 | 13.2 | 26.8 | 4.8 | 13.2 | 26.8 | 4.8 | 14.4 | 24.0 | 3.1 | 13.8 | 26.0 | 3.1 | 12.7 | 23.0 | Mangano et al., GCN 12559 |
| 111222619 | GRB 111222A | 14:51:55.03 | 207.6 | 59.1 | 3.4 | 207.6 | 59.1 | 3.4 | 189.6 | 65.8 | 3.1 | 173.4 | 65.2 | 1.7 | 179.2 | 69.0 | Hurley et al., GCN 12714 |
| 111228657 | GRB 111228A | 15:45:30.81 | 148.5 | 22.2 | 6.7 | 148.5 | 22.2 | 6.7 | 147.3 | 15.2 | 2.4 | 146.6 | 14.6 | 2.4 | 150.1 | 18.3 | Guver, GCN 12741 |
| 120102095 | GRB 120102A | 02:16:23.24 | 281.8 | 19.6 | 12.4 | 286.4 | 16.5 | 5.2 | 272.6 | 17.4 | 5.3 | 277.1 | 20.4 | 2.0 | 276.2 | 24.7 | Marshall et al., GCN 12794 |
| 120114681 | GRB 120114A | 16:20:05.68 | 307.7 | 58.3 | 14.3 | 307.7 | 58.3 | 14.3 | 311.7 | 49.6 | 7.9 | 311.0 | 52.1 | 5.4 | 317.9 | 57.0 | Sakamoto et al., GCN 12833 |
| 120118709 | GRB 120118B | 17:00:22.95 | 115.3 | −24.9 | 29.4 | 115.3 | −24.9 | 29.4 | 128.6 | −13.9 | 13.3 | 131.2 | −9.6 | 8.2 | 124.9 | −7.2 | Littlejohns et al., GCN 12852 |
| 120119170 | GRB 120119A | 04:04:25.07 | 113.6 | −4.9 | 5.9 | 113.5 | −4.8 | 4.5 | 119.2 | −7.0 | 1.3 | 119.0 | −9.0 | 1.1 | 120.0 | −9.1 | Beardmore et al., GCN 859 |
| 120212383 | GRB 120212A | 09:11:23.50 | 40.8 | −13.2 | 21.8 | 40.8 | −13.2 | 21.8 | 26.9 | −22.5 | 10.3 | 32.9 | −15.1 | 10.0 | 43.1 | −18.0 | Sonbas et al., GCN 12930 |
| 120302080 | GRB 120302A | 01:55:34.01 | 146.8 | 31.1 | 26.1 | 146.8 | 31.1 | 26.1 | 148.3 | 22.4 | 18.0 | 147.0 | 25.2 | 7.7 | 122.5 | 29.7 | Sakamoto et al., GCN 13000 |
| 120312671 | GRB 120312A | 16:06:29.67 | 261.9 | −6.4 | 18.8 | 261.9 | −6.4 | 18.8 | 259.4 | −2.3 | 8.7 | 254.3 | 11.5 | 7.8 | 251.8 | 23.9 | Stamatikos et al., GCN 13049 |
| 120323507 | GRB 120323A | 12:10:19.73 | 335.3 | 35.6 | 3.3 | 335.3 | 35.6 | 3.3 | 345.8 | 26.5 | 1.0 | 345.8 | 26.5 | 1.0 | 340.4 | 29.7 | Golenetskii et al., GCN 13102 |
| 120326056 | GRB 120326A | 01:20:31.52 | 255.8 | 68.0 | 11.9 | 243.6 | 70.7 | 8.8 | 274.1 | 64.8 | 5.3 | 262.2 | 62.1 | 4.2 | 273.9 | 69.3 | Siegel et al., GCN 13105 |
| 120403857 | GRB 120403B | 20:33:58.50 | 291.5 | −82.9 | 21.3 | 291.5 | −82.9 | 21.3 | 268.8 | −76.9 | 11.2 | 241.5 | −80.4 | 12.5 | 55.3 | −89.0 | Goad et al., GCN 13205 |
| 120512112 | GRB 120512A | 02:41:44.34 | 324.4 | 17.1 | 14.0 | 327.5 | 11.8 | 6.6 | 326.3 | 13.3 | 1.2 | 324.7 | 14.7 | 1.8 | 325.6 | 13.6 | Mereghetti et al., GCN 13300 |
| 120521380 | GRB 120521B | 09:07:52.39 | 167.1 | −45.7 | 21.0 | 216.0 | −48.2 | 25.9 | 192.7 | −38.8 | 10.9 | 208.1 | −47.1 | 5.2 | 197.0 | −52.7 | Cummings et al., GCN 13305 |
| 120624309 | GRB 120624A | 07:24:25.34 | 314.0 | 60.3 | 3.3 | 314.0 | 60.3 | 3.3 | 0.7 | −6.3 | 1.2 | 0.7 | −6.3 | 1.2 | 4.8 | 7.2 | Golenetskii et al., GCN 13376 |
| 120624933 | GRB 120624B | 22:23:54.94 | 178.2 | 47.1 | 22.0 | 174.3 | 22.5 | 4.2 | 171.9 | 5.7 | 1.2 | 171.8 | 5.6 | 1.0 | 170.9 | 8.9 | Sakamoto et al., GCN 13384 |
| 120703726 | GRB 120703A | 17:25:17.04 | 325.3 | −32.6 | 17.6 | 345.2 | −27.8 | 4.4 | 340.2 | −29.1 | 1.6 | 339.8 | −29.5 | 1.7 | 339.4 | −29.7 | Stamatikos et al., GCN 13414 |
| 120709883 | GRB 120709A | 21:11:40.37 | 338.5 | −57.8 | 6.0 | 319.8 | −68.0 | 5.0 | 327.0 | −52.2 | 1.1 | 319.9 | −50.0 | 1.6 | 318.4 | −50.0 | Kocevski et al., GCN 13423 |
| 120711115 | GRB 120711A | 02:44:53.30 | 69.6 | −62.9 | 8.5 | 56.5 | −63.7 | 5.7 | 77.2 | −66.3 | 1.0 | 79.4 | −66.6 | 1.0 | 94.7 | −71.0 | Gotz et al., GCN 13434 |
| 120712571 | GRB 120712A | 13:42:25.61 | 175.4 | −23.2 | 11.8 | 165.7 | −28.0 | 8.6 | 172.0 | −20.8 | 3.7 | 175.2 | −19.8 | 1.9 | 169.6 | −20.1 | Barthelmy et al., GCN 13455 |
| 120728934 | GRB 120728A | 22:25:12.74 | 167.1 | −45.7 | 21.0 | 167.1 | −45.7 | 21.0 | 131.5 | −57.0 | 6.8 | 138.2 | −54.0 | 6.2 | 137.1 | −54.4 | Cummings et al., GCN 13525 |
| 120729456 | GRB 120729A | 10:56:12.67 | ⋯ | ⋯ | ⋯ | 16.5 | 51.5 | 10.8 | 17.5 | 60.2 | 2.4 | 17.0 | 49.2 | 3.0 | 13.1 | 49.9 | Ukwatta et al., GCN 13530 |
| 120811649 | GRB 120811C | 15:34:55.09 | 215.3 | 56.6 | 20.4 | 215.3 | 56.4 | 17.2 | 225.9 | 50.1 | 10.8 | 214.4 | 55.8 | 5.3 | 199.7 | 62.3 | Barlow et al., GCN 13622 |
| 120817168 | GRB 120817B | 04:02:29.72 | ⋯ | ⋯ | ⋯ | 233.5 | −38.2 | 3.3 | 12.5 | −21.6 | 4.6 | 12.3 | −23.8 | 3.9 | 8.3 | −26.5 | Golenetskii et al., GCN 13670 |
| 120907017 | GRB 120907A | 00:24:24.51 | 80.9 | 0.6 | 14.6 | 80.9 | 0.6 | 14.6 | 77.3 | −2.5 | 12.0 | 74.1 | −8.5 | 11.7 | 74.7 | −9.3 | Racusin et al., GCN 13716 |
| 120908938 | GRB 120908A | 22:31:00.02 | 238.5 | −26.3 | 12.0 | 231.6 | −28.7 | 26.5 | 239.4 | −17.3 | 7.5 | 233.3 | −21.1 | 4.0 | 230.6 | −25.8 | Morii et al., GCN 13731 |
| 120909070 | GRB 120909A | 01:41:22.40 | 281.1 | −51.3 | 15.4 | 284.7 | −56.5 | 11.7 | 275.2 | −64.7 | 5.1 | 280.0 | −59.4 | 3.3 | 275.7 | −59.4 | Osborne et al., GCN 13732 |
| 120911298 | GRB 120911A | 07:08:33.99 | 336.9 | 61.6 | 19.7 | 336.9 | 61.6 | 19.7 | 355.1 | 62.6 | 6.8 | 351.8 | 61.5 | 4.3 | 358.0 | 63.1 | Cannizzo et al., GCN 13744 |
| 120913846 | GRB 120913A | 20:18:22.89 | 140.0 | 21.0 | 33.6 | 140.0 | 21.0 | 33.6 | 142.0 | 20.7 | 11.8 | 132.6 | 31.7 | 10.7 | 146.4 | 27.0 | Helder et al., GCN 13762 |
| 120913997 | GRB 120913B | 23:55:58.77 | 234.7 | −7.0 | 19.8 | 218.9 | 24.6 | 13.5 | 215.4 | −14.2 | 4.4 | 214.8 | −16.6 | 1.5 | 213.6 | −14.5 | Helder et al., GCN 13763 |
| 120916173 | GRB 120916A | 04:08:40.75 | 201.7 | 34.3 | 13.4 | 201.7 | 34.3 | 13.4 | 196.0 | 32.9 | 6.0 | 209.7 | 39.6 | 1.7 | 205.8 | 36.7 | Vianello et al., GCN 13777 |
| 120922939 | GRB 120922A | 22:32:09.47 | 308.3 | −41.7 | 21.0 | 308.3 | −41.7 | 21.0 | 231.1 | −20.6 | 10.8 | 235.1 | −23.9 | 7.1 | 234.8 | −20.2 | Yershov et al., GCN 13793 |
| 121011469 | GRB 121011A | 11:15:25.70 | 215.5 | 73.1 | 25.8 | 277.3 | 45.9 | 11.4 | 261.2 | 44.2 | 5.7 | 261.1 | 39.5 | 3.6 | 260.2 | 41.1 | Racusin et al., GCN 13845 |
| 121031949 | GRB 121031A | 22:47:15.27 | 184.0 | −6.8 | 26.2 | 176.4 | 6.3 | 11.7 | 162.9 | −10.3 | 5.7 | 173.1 | −1.9 | 3.4 | 170.8 | −3.5 | D'Elia et al., GCN 13934 |
| 121123421 | GRB 121123A | 10:06:00.59 | 316.9 | −27.7 | 25.0 | 307.3 | −8.9 | 8.8 | 306.7 | −14.0 | 5.2 | 307.8 | −14.5 | 1.7 | 307.4 | −11.9 | Helder et al., GCN 13982 |

**Table 9**
(Continued)

| Burst Name | Common Name | Trigger Time | FSW$_{first}$ for Ref. | | | FSW$_{last}$ for Ref. | | | Ground Auto for Ref. | | | HitL for Ref. | | | Ref. Location | | Reference |
|---|---|---|---|---|---|---|---|---|---|---|---|---|---|---|---|---|---|
| | | (UT) | (R.A. | Decl. | Err) | (R.A. | Decl. | Err) | (R.A. | Decl. | Err) | (R.A. | Decl. | Err) | (R.A. | Decl.) | |
| 121125356 | GRB 121125A | 08:32:29.63 | 203.7 | 43.0 | 19.6 | 209.9 | 53.4 | 13.2 | 235.7 | 57.1 | 3.4 | 229.1 | 55.0 | 1.9 | 228.5 | 55.3 | Barlow et al., GCN 13993 |
| 121128212 | GRB 121128A | 05:05:50.96 | 278.7 | 28.7 | 16.7 | 278.3 | 33.6 | 5.7 | 272.6 | 38.9 | 2.2 | 278.8 | 41.6 | 1.5 | 300.6 | 54.3 | Oates et al., GCN 14007 |
| 121202181 | GRB 121202A | 04:20:09.17 | 257.9 | 30.4 | 34.9 | 257.9 | 30.4 | 34.9 | 249.7 | 41.8 | 11.6 | 246.5 | 24.4 | 5.8 | 256.8 | 24.0 | Oates et al., GCN 14032 |
| 121211574 | GRB 121211A | 13:47:03.59 | 190.0 | 46.7 | 15.7 | 190.0 | 46.7 | 15.7 | 208.4 | 35.6 | 10.6 | 206.2 | 30.0 | 11.7 | 195.5 | 30.2 | Mangano et al., GCN 14057 |
| 121217313 | GRB 121217A | 07:30:01.58 | 178.1 | −75.3 | 17.6 | 157.6 | −70.8 | 15.9 | 149.5 | −51.5 | 19.6 | 160.1 | −68.7 | 5.2 | 153.7 | −62.3 | Siegel et al., GCN 14089 |
| 130206817 | GRB 130206A | 19:36:30.45 | 149.4 | −58.5 | 17.6 | 149.4 | −58.5 | 17.6 | 0.9 | 20.4 | 50.5 | 140.4 | −60.5 | 4.5 | 140.4 | −58.2 | De Pasquale et al., GCN 14181 |
| 130215063 | GRB 130215A | 01:31:26.02 | 37.7 | 35.9 | 14.3 | 37.7 | 35.9 | 14.3 | 37.6 | 18.7 | 4.7 | 38.5 | 17.0 | 2.1 | 43.5 | 13.4 | D'Elia et al., GCN 14204 |
| 130216790 | GRB 130216B | 18:58:11.70 | 66.1 | −2.2 | 9.4 | 64.0 | 7.7 | 6.8 | 60.4 | 4.0 | 3.0 | 61.7 | 3.5 | 2.3 | 58.9 | 2.0 | Cummings et al., GCN 14232 |
| 130216927 | GRB 130216A | 22:15:21.42 | 68.1 | 16.1 | 8.5 | 64.8 | 20.2 | 7.2 | 69.4 | 16.3 | 1.7 | 69.4 | 16.3 | 1.5 | 67.9 | 14.7 | Melandri et al., GCN 14223 |
| 130305486 | GRB 130305A | 11:39:11.37 | 110.0 | 48.1 | 4.2 | 110.6 | 48.0 | 10.0 | 120.1 | 50.1 | 1.0 | 119.7 | 49.0 | 1.0 | 116.8 | 52.0 | Cummings et al., GCN 14257 |
| 130306991 | GRB 130306A | 23:47:25.57 | 279.0 | −12.6 | 50.0 | 279.0 | −12.6 | 50.0 | 278.0 | −12.6 | 1.0 | 276.9 | −11.5 | 1.0 | 279.5 | −11.7 | Barthelmy et al., GCN 14279 |
| 130310840 | GRB 130310A | 20:09:41.50 | 154.8 | −21.4 | 26.8 | 127.3 | 1.4 | 3.4 | 158.2 | −25.2 | 14.3 | 142.0 | −22.0 | 1.6 | 142.3 | −17.2 | Guiriec et al., GCN 14282 |
| 130325203 | GRB 130325A | 04:51:54.30 | 133.8 | −18.4 | 10.4 | 127.7 | −19.5 | 5.6 | 130.9 | −19.7 | 1.6 | 130.7 | −21.0 | 1.5 | 122.8 | −18.9 | Vianello et al., GCN 14332 |
| 130327350 | GRB 130327B | 08:24:04.05 | 218.9 | −67.2 | 7.2 | 219.4 | −67.1 | 4.8 | 208.0 | −74.8 | 2.1 | 207.6 | −72.3 | 1.0 | 218.1 | −69.5 | Ohno et al., GCN 14347 |
| 130420313 | GRB 130420A | 07:30:19.92 | 188.0 | 55.2 | 15.9 | 188.0 | 55.2 | 15.9 | 202.4 | 54.7 | 4.7 | 205.7 | 58.8 | 4.4 | 196.1 | 59.4 | Page et al., GCN 14406 |
| 130420539 | GRB 130420B | 12:56:32.99 | 176.4 | 56.5 | 28.9 | 176.4 | 56.5 | 28.9 | 184.1 | 53.0 | 15.0 | 184.8 | 51.0 | 6.2 | 183.1 | 54.4 | Oates et al., GCN 14411 |
| 130427324 | GRB 130427A | 07:47:06.42 | 170.6 | 47.7 | 3.4 | 170.7 | 48.1 | 3.2 | 169.9 | 24.3 | 1.0 | 172.5 | 25.5 | 1.0 | 173.1 | 27.7 | Maselli et al., GCN 14448 |
| 130502327 | GRB 130502B | 07:51:11.76 | 57.8 | 59.8 | 14.9 | 52.7 | 64.7 | 4.0 | 72.5 | 69.8 | 1.0 | 77.0 | 70.3 | 1.0 | 66.8 | 71.1 | Kocevski et al., GCN 14532 |
| 130502743 | GRB 130502A | 17:50:30.74 | 130.9 | 14.3 | 12.3 | 130.9 | 14.3 | 12.3 | 134.1 | 7.8 | 8.5 | 133.7 | −0.5 | 11.6 | 138.6 | −0.1 | Troja et al., GCN 14527 |
| 130504978 | GRB 130504C | 23:28:57.52 | 93.3 | 0.9 | 27.1 | 87.4 | 9.3 | 3.9 | 90.3 | 4.1 | 1.0 | 90.7 | 4.3 | 1.0 | 91.6 | 3.8 | Kocevski et al., GCN 14574 |
| 130515056 | GRB 130515A | 01:21:17.88 | 296.7 | −51.8 | 11.1 | 296.7 | −51.8 | 11.1 | 297.7 | −48.4 | 2.1 | 291.5 | −51.8 | 3.7 | 283.4 | −54.3 | Malesani et al., GCN 14650 |
| 130518580 | GRB 130518A | 13:54:37.53 | 354.7 | 43.7 | 10.3 | 354.5 | 44.2 | 3.8 | 356.3 | 47.1 | 1.0 | 356.3 | 47.0 | 1.0 | 355.7 | 47.5 | Cummings et al., GCN 14676 |
| 130528695 | GRB 130528A | 16:41:24.41 | 245.5 | 83.0 | 11.1 | 197.1 | 86.2 | 6.7 | 84.2 | 81.6 | 2.1 | 68.1 | 82.6 | 1.9 | 139.5 | 87.3 | D'Elia et al., GCN 14711 |
| 130606497 | GRB 130606B | 11:55:33.63 | 203.2 | 45.9 | 7.3 | 197.0 | 50.0 | 3.5 | 222.3 | −18.8 | 1.0 | 222.3 | −18.8 | 1.0 | 218.5 | −22.1 | Vianello et al., GCN 14795 |
| 130609129 | GRB 130609A | 03:05:10.69 | 146.4 | 15.2 | 16.0 | 146.4 | 15.2 | 16.0 | 150.3 | 28.3 | 12.7 | 148.3 | 26.7 | 8.0 | 152.7 | 24.1 | Cummings et al., GCN 14828 |
| 130609902 | GRB 130609B | 21:38:35.61 | 95.5 | −67.0 | 10.3 | 105.9 | −64.5 | 4.0 | 55.5 | −33.0 | 1.8 | 51.9 | −42.9 | 1.0 | 53.8 | −40.2 | Krimm et al., GCN 14841 |
| 130610133 | GRB 130610A | 03:12:10.50 | 217.8 | 29.0 | 23.9 | 223.4 | 27.0 | 11.9 | 216.7 | 28.0 | 5.8 | 226.5 | 29.3 | 3.5 | 224.4 | 28.2 | Cummings et al., GCN 14842 |

**Notes.** These locations come from *Swift* BAT, *Swift* XRT, *Fermi*-LAT, *INTEGRAL*, MAXI, Super-*AGILE*, and the IPN. All R.A., decl., and Err are in units of degree.

(This table is available in its entirety in a machine-readable form.)

**Table 10**
134 Locations for GRBs That Were Also Triangulated by IPN

| Burst Name | Common Name | Trigger Time (UT) | IPN Annulus (R.A.) | Decl. | Err | Width[a] | FSW_first for IPN (R.A.) | Decl. | Err | FSW_last for IPN (R.A.) | Decl. | Err | Ground Auto for IPN (R.A.) | Decl. | Err | HitL for IPN (R.A.) | Decl. | Err |
|---|---|---|---|---|---|---|---|---|---|---|---|---|---|---|---|---|---|---|
| 080715950 | GRB 080715A | 22:48:40.17 | 148.6 | 14.5 | 60.5 | 0.3 | ... | ... | ... | ... | ... | ... | 210.6 | 12.8 | 3.3 | 213.3 | 12.2 | 2.5 |
| 080723985 | GRB 080723D | 23:37:42.71 | 158.4 | 10.2 | 70.9 | 0.1 | ... | ... | ... | ... | ... | ... | 57.7 | 78.7 | 1.3 | 52.9 | 79.1 | 1.0 |
| 080724401 | GRB 080724A | 09:37:40.61 | ... | ... | ... | ... | ... | ... | ... | ... | ... | ... | 356.2 | 32.6 | 1.6 | 357.1 | 32.0 | 1.1 |
| 080730520 | GRB 080730A | 12:29:15.41 | ... | ... | ... | ... | ... | ... | ... | ... | ... | ... | 246.3 | 5.5 | 4.1 | 246.3 | 5.5 | 2.5 |
| 080730786 | GRB 080730B | 18:51:38.19 | 165.9 | 6.5 | 79.0 | 0.1 | ... | ... | ... | ... | ... | ... | 246.6 | 27.7 | 2.0 | 246.6 | 27.7 | 1.9 |
| 080802386 | GRB 080802A | 09:15:10.53 | ... | ... | ... | ... | ... | ... | ... | ... | ... | ... | 185.9 | 22.0 | 7.9 | 157.5 | 40.4 | 14.2 |
| 080803772 | GRB 080803A | 18:31:22.05 | 169.9 | 4.4 | 84.5 | 0.5 | ... | ... | ... | ... | ... | ... | 145.8 | 75.5 | 8.1 | 322.6 | 65.6 | 6.4 |
| 080806896 | GRB 080806B | 21:29:40.83 | 173.0 | 2.8 | 74.1 | 0.3 | ... | ... | ... | ... | ... | ... | 239.2 | 43.5 | 2.7 | 243.1 | 47.3 | 2.0 |
| 080807993 | GRB 080807A | 23:50:32.64 | ... | ... | ... | ... | ... | ... | ... | ... | ... | ... | 100.9 | −14.2 | 3.6 | 101.6 | −16.0 | 2.7 |
| 080816503 | GRB 080816A | 12:04:18.18 | 181.3 | −1.9 | 56.1 | 0.2 | ... | ... | ... | ... | ... | ... | 152.8 | 43.0 | 4.2 | 155.2 | 42.0 | 2.6 |
| 080816989 | GRB 080816B | 23:43:54.70 | 2.1 | 2.4 | 82.4 | 0.3 | ... | ... | ... | ... | ... | ... | 290.8 | −6.0 | 8.5 | 290.7 | −6.0 | 5.0 |
| 080817161 | GRB 080817A | 03:52:10.54 | 182.2 | −2.4 | 38.9 | 0.2 | ... | ... | ... | ... | ... | ... | 150.7 | −17.7 | 2.1 | 149.0 | −17.8 | 1.3 |
| 080817720 | GRB 080817B | 17:17:07.52 | 2.3 | 2.6 | 83.6 | 0.2 | ... | ... | ... | ... | ... | ... | 80.8 | −30.5 | 9.5 | 85.8 | −28.0 | 6.9 |
| 080821332 | GRB 080821A | 07:57:26.48 | 185.7 | −4.3 | 73.2 | 0.3 | ... | ... | ... | ... | ... | ... | 233.8 | 33.2 | 3.0 | 238.5 | 33.5 | 3.9 |
| 080824909 | GRB 080824A | 21:48:54.73 | ... | ... | ... | ... | ... | ... | ... | ... | ... | ... | 122.7 | −1.2 | 1.3 | 122.4 | −2.7 | 1.3 |
| 080825593 | GRB 080825C | 14:13:48.11 | 189.1 | −6.2 | 45.7 | 0.1 | ... | ... | ... | ... | ... | ... | 231.0 | −2.1 | 1.1 | 231.3 | −3.1 | 1.0 |
| 080830368 | GRB 080830A | 08:50:16.34 | 192.7 | −8.2 | 50.6 | 0.2 | ... | ... | ... | ... | ... | ... | 158.0 | 31.9 | 4.3 | 158.7 | 30.4 | 2.6 |
| 080906212 | GRB 080906B | 05:05:11.55 | 197.3 | −10.8 | 13.7 | 0.4 | ... | ... | ... | ... | ... | ... | 187.7 | −7.4 | 2.3 | 190.6 | −8.5 | 2.2 |
| 080925775 | GRB 080925A | 18:35:56.00 | 21.9 | 13.7 | 71.3 | 0.2 | ... | ... | ... | ... | ... | ... | 95.1 | 18.7 | 1.6 | 95.1 | 17.6 | 1.2 |
| 081003644 | GRB 081003C | 15:27:17.94 | ... | ... | ... | ... | ... | ... | ... | ... | ... | ... | 267.2 | 26.1 | 5.2 | 254.5 | 40.3 | 5.6 |
| 081009140 | GRB 081009A | 03:20:58.07 | 189.3 | −5.2 | 65.9 | 0.5 | 252.2 | 19.8 | 5.1 | 252.2 | 14.7 | 3.7 | 250.4 | 20.6 | 1.0 | 250.4 | 20.6 | 1.0 |
| 081009690 | GRB 081009B | 16:33:37.34 | 8.8 | 4.9 | 58.8 | 0.6 | 53.0 | 24.8 | 9.2 | 71.5 | 16.4 | 6.8 | 67.5 | 13.6 | 2.8 | 65.2 | 14.5 | 1.7 |
| 081021398 | GRB 081021A | 09:33:28.02 | 189.7 | −2.0 | 23.7 | 0.5 | 212.9 | −16.3 | 13.8 | 203.6 | −26.0 | 8.8 | 197.2 | −28.2 | 4.0 | 197.1 | −26.2 | 3.3 |
| 081101532 | GRB 081101B | 12:45:24.09 | 202.0 | −6.8 | 24.7 | 0.3 | 219.5 | −29.5 | 10.5 | 220.2 | −29.5 | 5.2 | 212.3 | −28.0 | 2.3 | 211.0 | −28.0 | 1.8 |
| 081102365 | GRB 081102B | 08:45:00.51 | 203.3 | −7.4 | 38.6 | 0.1 | 247.1 | 35.8 | 13.6 | 247.1 | 35.8 | 13.6 | 242.8 | 31.0 | 8.6 | 212.4 | 31.2 | 8.4 |
| 081110601 | GRB 081110A | 14:25:43.04 | 33.5 | 11.8 | 74.3 | 0.2 | 116.9 | 24.9 | 4.9 | 116.9 | 24.9 | 5.2 | 112.6 | 21.8 | 2.1 | 111.7 | 21.5 | 2.2 |
| 081122520 | GRB 081122A | 12:28:12.22 | ... | ... | ... | ... | 339.2 | 33.9 | 4.2 | 339.3 | 33.9 | 5.9 | 336.9 | 40.1 | 1.0 | 338.3 | 39.8 | 1.0 |
| 081125496 | GRB 081125A | 11:53:39.01 | 64.5 | 21.8 | 46.1 | 0.1 | 45.8 | −24.6 | 6.8 | 41.0 | −22.7 | 4.3 | 45.5 | −20.1 | 1.1 | 45.5 | −20.1 | 1.0 |
| 081129161 | GRB 081129A | 03:52:04.27 | ... | ... | ... | ... | 58.0 | −64.7 | 4.3 | 58.0 | −64.7 | 4.3 | 59.8 | −60.3 | 2.6 | 60.9 | −56.3 | 3.4 |
| 081207680 | GRB 081207A | 16:18:46.94 | ... | ... | ... | ... | 106.4 | 75.0 | 12.9 | 123.4 | 66.0 | 6.5 | 110.2 | 70.2 | 1.9 | 114.0 | 69.6 | 1.6 |
| 081215784 | GRB 081215A | 18:48:36.85 | 78.7 | 17.7 | 51.6 | 0.5 | 10.6 | 44.1 | 3.4 | 10.6 | 44.1 | 3.4 | 124.0 | 50.7 | 1.3 | 137.4 | 50.1 | 1.0 |
| 081215880 | GRB 081215B | 21:06:53.04 | ... | ... | ... | ... | 235.5 | −51.2 | 19.0 | 227.8 | −52.6 | 14.8 | 231.4 | −49.7 | 6.1 | 232.9 | −49.2 | 6.8 |
| 081224887 | GRB 081224A | 21:17:55.42 | ... | ... | ... | ... | 214.2 | 77.3 | 4.2 | 212.5 | 72.2 | 3.9 | 201.7 | 75.2 | 1.0 | 202.1 | 75.1 | 1.0 |
| 081231140 | GRB 081231A | 03:21:01.94 | 273.1 | −24.1 | 54.2 | 0.1 | 214.3 | −35.4 | 9.3 | 215.2 | −36.6 | 4.7 | 212.3 | −39.7 | 2.1 | 211.8 | −37.3 | 1.1 |
| 090108020 | GRB 090108A | 00:29:02.37 | 268.1 | −20.2 | 70.7 | 0.5 | 258.6 | 53.9 | 5.5 | 258.6 | 53.9 | 5.5 | 259.8 | 44.9 | 4.2 | 257.4 | 44.0 | 4.0 |
| 090112729 | GRB 090112B | 17:30:15.46 | 103.5 | 23.7 | 86.5 | 0.1 | 194.1 | 19.3 | 8.4 | 194.1 | 19.3 | 8.4 | 193.8 | 24.9 | 2.1 | 193.3 | 25.9 | 1.2 |
| 090131090[a] | GRB 090131A | 02:09:21.15 | 349.21[a] | 18.47[a] | 0.0245[a] | 0.0612[a] | 33.4 | 28.1 | 29.4 | 353.3 | 16.1 | 3.9 | 352.9 | 20.5 | 1.6 | 352.4 | 20.9 | 1.2 |
| 090202347 | GRB 090202A | 08:19:30.41 | 332.2 | −12.3 | 56.9 | 0.4 | 260.3 | −15.9 | 22.4 | 260.4 | −15.9 | 7.4 | 280.7 | −9.6 | 4.7 | 276.4 | −4.8 | 3.3 |
| 090207777 | GRB 090207A | 18:39:10.84 | 158.7 | 8.7 | 78.3 | 0.2 | 244.5 | 14.7 | 9.8 | 243.5 | 34.9 | 9.8 | 242.3 | 38.0 | 4.2 | 243.5 | 36.9 | 4.2 |
| 090227310 | GRB 090227A | 07:25:57.01 | 320.3 | −16.6 | 46.8 | 0.2 | 9.1 | −42.5 | 9.2 | 4.2 | −45.9 | 7.3 | 2.5 | −42.2 | 2.2 | 2.5 | −42.1 | 1.2 |
| 090228204[a] | GRB 090228A | 04:53:20.92 | 98.52[a] | −28.61[a] | 0.1158[a] | 0.0074[a] | 108.8 | −36.1 | 3.3 | 108.8 | −36.1 | 3.3 | 103.3 | −26.7 | 1.6 | 103.3 | −26.7 | 1.4 |
| 090304216 | GRB 090304A | 05:10:48.16 | 332.5 | −6.4 | 82.7 | 0.2 | 276.8 | −77.9 | 25.3 | 204.5 | −73.3 | 21.0 | 223.4 | −71.9 | 9.1 | 244.2 | −77.7 | 22.2 |
| 090305052 | GRB 090305B | 01:14:35.73 | 151.6 | 6.7 | 63.5 | 0.2 | 168.5 | 77.5 | 7.0 | 168.5 | 77.5 | 7.0 | 144.6 | 65.9 | 3.3 | 141.5 | 62.4 | 6.8 |
| 090308734 | GRB 090308B | 17:36:24.70 | 329.3 | −8.0 | 62.1 | 0.3 | 22.4 | −58.1 | 5.1 | 22.4 | −58.1 | 5.1 | 32.3 | −54.0 | 2.1 | 18.6 | −55.1 | 3.2 |
| 090328713 | GRB 090328B | 17:07:04.94 | 207.5 | −7.8 | 64.6 | 0.5 | 157.4 | 52.8 | 8.2 | 157.4 | 52.8 | 8.2 | 162.7 | 34.0 | 5.3 | 155.5 | 29.2 | 9.7 |
| 090330279 | GRB 090330A | 06:42:22.10 | 154.3 | 11.1 | 21.9 | 0.6 | 142.0 | −4.6 | 29.7 | 142.0 | −4.6 | 29.7 | 159.9 | −8.8 | 2.5 | 158.9 | −8.4 | 2.6 |

**Table 10**
(Continued)

| Burst Name | Common Name | Trigger Time | IPN Annulus | | | | FSW_first for IPN | | | FSW_last for IPN | | | Ground Auto for IPN | | | HitL for IPN | | |
|---|---|---|---|---|---|---|---|---|---|---|---|---|---|---|---|---|---|---|
| | | (UT) | (R.A. | Decl. | Err | Width)[a] | (R.A. | Decl. | Err) | (R.A. | Decl. | Err) | (R.A. | Decl. | Err) | (R.A. | Decl. | Err) |
| 090411838 | GRB 090411A | 20:06:36.89 | 164.7 | 9.1 | 79.1 | 0.2 | 159.9 | −63.8 | 6.9 | 162.8 | −64.8 | 6.5 | 152.8 | −68.3 | 2.4 | 159.2 | −67.2 | 3.9 |
| 090411991 | GRB 090411B | 23:47:44.88 | 352.8 | −4.3 | 53.4 | 0.1 | 9.4 | −28.2 | 30.8 | 47.1 | 7.7 | 8.9 | 30.9 | −0.8 | 6.9 | 38.8 | 4.9 | 2.4 |
| 090413122 | GRB 090413A | 02:55:57.25 | 346.7 | −8.3 | 77.0 | 0.3 | · · · | · · · | · · · | · · · | · · · | · · · | 253.2 | −25.1 | 10.0 | 285.3 | −4.1 | 6.5 |
| 090425377 | GRB 090425A | 09:03:30.57 | · · · | · · · | · · · | · · · | 127.3 | 58.1 | 14.7 | 109.1 | 68.8 | 6.9 | 100.3 | 71.7 | 2.2 | 103.7 | 71.2 | 1.4 |
| 090429753 | GRB 090429D | 18:03:57.52 | · · · | · · · | · · · | · · · | 128.2 | 13.8 | 8.3 | 128.2 | 13.8 | 8.3 | 124.6 | 6.7 | 8.5 | 124.4 | 7.9 | 4.9 |
| 090514006 | GRB 090514A | 00:08:39.16 | 25.9 | 7.4 | 19.2 | 0.3 | 8.9 | −14.3 | 5.8 | 8.7 | −14.3 | 6.7 | 8.8 | −12.3 | 5.3 | 8.8 | −12.3 | 3.6 |
| 090514726 | GRB 090514B | 17:26:07.34 | 26.7 | 7.6 | 74.7 | 0.2 | 304.3 | −24.4 | 5.5 | 304.3 | −24.4 | 5.5 | 304.5 | −22.3 | 1.9 | 303.2 | −23.1 | 2.6 |
| 090516137 | GRB 090516B | 03:17:20.17 | 208.9 | −8.5 | 85.1 | 0.8 | 122.3 | −67.7 | 34.3 | 133.7 | −55.5 | 25.9 | 105.2 | −68.8 | 5.9 | 104.7 | −70.3 | 2.5 |
| 090516853 | GRB 090516C | 20:28:40.05 | 30.0 | 9.1 | 27.8 | 0.6 | 16.9 | −14.4 | 6.5 | 16.9 | −14.4 | 6.3 | 23.8 | −18.9 | 3.9 | 24.0 | −19.0 | 3.7 |
| 090518244 | GRB 090518B | 05:51:04.67 | · · · | · · · | · · · | · · · | 210.4 | −18.6 | 8.7 | 210.4 | −18.6 | 8.7 | 206.7 | −16.8 | 5.1 | 210.4 | −15.9 | 4.5 |
| 090520850 | GRB 090520C | 20:23:19.31 | 37.0 | 12.1 | 82.4 | 0.3 | 110.2 | −19.4 | 7.0 | 110.5 | −19.0 | 6.8 | 118.5 | −17.6 | 2.5 | 117.2 | −17.9 | 1.6 |
| 090524346 | GRB 090524A | 08:17:56.24 | 223.2 | −14.4 | 83.4 | 0.1 | 309.7 | −64.4 | 10.9 | 319.2 | −68.0 | 5.3 | 332.4 | −67.5 | 1.9 | 329.2 | −67.7 | 1.9 |
| 090528516 | GRB 090528B | 12:22:31.29 | 51.2 | 17.3 | 90.0 | 0.1 | 301.4 | 39.4 | 14.1 | 313.1 | 33.1 | 4.9 | 311.5 | 31.0 | 1.0 | 312.7 | 30.8 | 1.0 |
| 090529564 | GRB 090529C | 13:32:00.49 | 206.3 | −9.7 | 69.3 | 0.1 | 168.0 | 40.8 | 4.4 | 164.3 | 36.8 | 3.9 | 162.0 | 45.5 | 2.1 | 162.4 | 47.4 | 2.1 |
| 090530760 | GRB 090530B | 18:14:24.44 | 56.0 | 18.9 | 14.6 | 0.6 | 75.4 | 8.8 | 12.1 | 77.3 | 13.4 | 4.9 | 73.5 | 14.8 | 1.2 | 72.1 | 14.3 | 1.3 |
| 090606471 | GRB 090606A | 11:18:08.01 | 251.4 | −22.7 | 73.1 | 0.3 | 5.4 | −77.4 | 15.5 | 85.4 | −77.4 | 15.5 | 150.2 | −71.7 | 8.6 | 135.4 | −74.2 | 5.7 |
| 090610648 | GRB 090610A | 15:33:25.94 | 81.6 | 24.4 | 17.4 | 0.3 | 82.6 | 32.9 | 13.5 | 82.6 | 32.9 | 13.5 | 87.7 | 36.1 | 11.0 | 86.6 | 36.6 | 11.7 |
| 090612619 | GRB 090612A | 14:50:50.50 | 86.4 | 24.8 | 19.3 | 0.3 | 80.3 | 14.4 | 7.8 | 76.4 | 17.5 | 7.3 | 71.9 | 13.3 | 5.0 | 67.8 | 11.1 | 3.5 |
| 090617208 | GRB 090617A | 04:59:58.58 | 97.4 | 25.2 | 12.5 | 0.3 | 86.8 | 53.0 | 11.3 | 86.8 | 53.0 | 11.3 | 79.6 | 26.8 | 7.0 | 79.4 | 22.7 | 7.6 |
| 090620400[a] | GRB 090620A | 09:36:23.47 | 234.25[a] | 64.70[a] | 0.0338[a] | 0.0422[a] | 228.6 | 60.9 | 6.9 | 243.1 | 68.0 | 4.6 | 238.6 | 61.8 | 1.4 | 237.4 | 61.2 | 1.1 |
| 090623107 | GRB 090623A | 02:34:17.57 | 223.9 | −15.8 | 77.9 | 0.1 | 312.3 | −52.0 | 7.3 | 313.2 | −47.6 | 6.6 | 307.3 | −47.6 | 3.4 | 312.0 | −44.9 | 1.5 |
| 090717034 | GRB 090717A | 00:49:32.11 | 61.3 | 20.3 | 87.3 | 0.1 | 95.0 | −66.3 | 9.2 | 97.2 | −62.0 | 4.8 | 92.0 | −63.7 | 3.0 | 87.1 | −63.7 | 1.2 |
| 090718762 | GRB 090718B | 18:17:42.85 | 242.5 | −20.5 | 32.5 | 0.1 | 267.5 | −43.5 | 16.5 | 273.5 | −37.3 | 4.3 | 271.9 | −35.9 | 1.6 | 273.9 | −35.0 | 1.1 |
| 090719063 | GRB 090719A | 01:31:26.62 | 242.7 | −20.5 | 74.6 | 0.1 | 200.8 | −41.0 | 4.3 | 0.6 | −52.3 | 3.8 | 340.4 | −70.0 | 1.0 | 338.1 | −69.4 | 1.0 |
| 090720710 | GRB 090720B | 17:02:56.91 | 274.5 | −23.9 | 61.1 | 0.7 | 204.5 | −55.4 | 4.5 | 204.5 | −55.4 | 4.5 | 203.7 | −57.5 | 1.8 | 224.2 | −56.2 | 4.7 |
| 090802235 | GRB 090802A | 05:39:03.09 | · · · | · · · | · · · | · · · | 84.1 | 30.9 | 5.1 | 84.1 | 30.9 | 5.1 | 84.3 | 34.1 | 3.6 | 84.3 | 34.1 | 4.2 |
| 090804940 | GRB 090804A | 22:33:20.02 | 170.6 | 2.4 | 44.3 | 0.1 | 127.2 | −9.4 | 4.3 | 129.5 | −14.0 | 4.2 | 129.5 | −11.8 | 1.0 | 128.6 | −12.2 | 1.0 |
| 090809978 | GRB 090809B | 23:28:14.62 | 175.0 | −0.2 | 76.2 | 0.3 | 87.9 | 8.8 | 9.3 | 88.0 | 8.7 | 4.2 | 97.1 | 0.1 | 1.1 | 97.7 | −0.7 | 1.0 |
| 090811696 | GRB 090811A | 16:41:50.04 | 355.9 | 1.0 | 85.8 | 0.1 | 278.4 | 22.3 | 10.1 | 278.4 | 22.3 | 10.1 | 278.1 | 19.7 | 7.7 | 285.7 | 30.7 | 8.9 |
| 090814368 | GRB 090814C | 08:49:41.23 | 358.4 | 2.4 | 70.5 | 0.1 | 303.8 | 74.8 | 8.6 | 303.8 | 74.8 | 8.6 | 348.6 | 66.1 | 11.3 | 349.7 | 67.0 | 9.9 |
| 090814950 | GRB 090814D | 22:47:28.78 | 358.8 | 2.7 | 61.5 | 0.3 | 330.0 | 42.2 | 31.7 | 326.4 | 37.9 | 8.6 | 309.0 | 45.7 | 4.0 | 299.6 | 43.1 | 2.7 |
| 090820027 | GRB 090820A | 00:38:16.19 | · · · | · · · | · · · | · · · | 84.6 | 47.1 | 23.2 | 86.0 | 17.4 | 3.4 | 89.8 | 25.8 | 1.0 | 90.0 | 26.9 | 1.0 |
| 090828099 | GRB 090828A | 02:22:48.20 | 185.9 | −7.4 | 57.9 | 0.3 | 129.0 | −35.3 | 23.8 | 124.5 | −26.1 | 5.4 | 123.5 | −25.5 | 3.4 | 124.3 | −26.2 | 1.0 |
| 090829672[a] | GRB 090829A | 16:07:38.87 | 323.06[a] | −37.46[a] | 0.0170[a] | 0.0375[a] | 326.1 | −47.7 | 23.3 | 323.8 | −41.2 | 4.5 | 327.3 | −33.1 | 1.1 | 327.2 | −33.1 | 1.0 |
| 090829702 | GRB 090829B | 16:50:40.14 | · · · | · · · | · · · | · · · | 7.1 | −15.7 | 21.9 | 354.1 | −17.5 | 9.3 | 351.6 | −11.8 | 4.9 | 354.7 | −4.3 | 2.4 |
| 090831317 | GRB 090831A | 07:36:36.59 | · · · | · · · | · · · | · · · | 87.8 | 55.9 | 9.7 | 87.8 | 55.9 | 9.7 | 148.0 | 50.2 | 6.3 | 145.3 | 49.5 | 2.2 |
| 090907808 | GRB 090907B | 19:23:47.48 | · · · | · · · | · · · | · · · | 88.8 | 16.3 | 6.1 | 88.8 | 16.3 | 6.1 | 80.7 | 16.5 | 5.2 | 84.3 | 23.2 | 4.8 |
| 090908341 | GRB 090908B | 08:10:39.82 | 185.8 | −8.1 | 31.0 | 0.3 | 163.1 | −12.8 | 30.3 | 165.0 | −23.8 | 21.9 | 168.3 | −26.6 | 9.2 | 161.8 | −22.1 | 6.5 |
| 090910812 | GRB 090910A | 19:29:48.81 | 4.9 | 7.7 | 74.8 | 0.2 | 23.7 | 56.4 | 9.8 | 7.3 | 53.9 | 7.9 | 284.1 | 67.3 | 2.9 | 284.9 | 70.6 | 1.1 |
| 090922539 | GRB 090922A | 12:56:42.14 | 355.2 | 0.7 | 75.1 | 0.2 | 354.3 | 75.5 | 4.5 | 354.2 | 75.6 | 4.9 | 17.1 | 74.2 | 1.2 | 17.1 | 74.4 | 1.0 |
| 090922605 | GRB 090922B | 14:30:41.53 | 355.1 | 0.7 | 55.6 | 0.2 | 22.9 | −22.8 | 21.0 | 52.4 | −75.7 | 6.5 | 33.5 | −35.5 | 8.7 | 16.4 | −24.4 | 5.3 |
| 090925389 | GRB 090925A | 09:20:33.68 | · · · | · · · | · · · | · · · | 315.7 | 24.6 | 11.7 | 313.7 | 19.9 | 8.6 | 326.2 | 16.8 | 3.6 | 334.0 | 13.6 | 3.9 |
| 090928646 | GRB 090928A | 15:29:44.67 | 172.2 | 3.0 | 78.5 | 0.2 | 98.2 | −54.2 | 10.2 | 98.1 | −59.4 | 9.4 | 92.7 | −53.8 | 9.9 | 94.4 | −53.6 | 8.2 |
| 091012783 | GRB 091012A | 18:47:02.77 | 41.4 | 15.7 | 68.7 | 0.4 | 239.4 | 58.0 | 4.4 | 239.4 | 58.0 | 4.4 | 131.3 | 87.4 | 1.5 | 131.5 | 87.4 | 1.4 |
| 091020977 | GRB 091020B | 23:26:34.45 | 124.6 | 21.0 | 75.3 | 0.1 | 176.3 | 28.4 | 5.7 | 173.4 | 2.2 | 6.6 | 190.3 | 0.2 | 3.3 | 191.3 | −4.7 | 2.9 |
| 091030828 | GRB 091030A | 19:52:26.87 | · · · | · · · | · · · | · · · | 40.8 | 22.1 | 6.2 | 40.9 | 22.4 | 4.7 | 42.1 | 24.1 | 1.8 | 42.1 | 23.9 | 1.6 |

**Table 10**
(Continued)

| Burst Name | Common Name | Trigger Time (UT) | IPN Annulus (R.A.) | Decl. | Err | Width[a] | FSW_first for IPN (R.A.) | Decl. | Err | FSW_last for IPN (R.A.) | Decl. | Err | Ground Auto for IPN (R.A.) | Decl. | Err | HitL for IPN (R.A.) | Decl. | Err |
|---|---|---|---|---|---|---|---|---|---|---|---|---|---|---|---|---|---|---|
| 091101143 | GRB 091101A | 03:26:32.49 | 56.2 | 16.4 | 55.9 | 0.6 | 31.6 | −26.8 | 9.5 | 26.8 | −35.2 | 6.0 | 24.7 | −33.8 | 4.1 | 30.2 | −33.4 | 3.3 |
| 091120191 | GRB 091120A | 04:34:40.23 | 316.9 | −18.6 | 83.3 | 0.1 | 225.1 | −19.9 | 11.4 | 225.1 | −19.9 | 11.4 | 224.3 | −26.9 | 2.9 | 224.3 | −26.9 | 1.3 |
| 091126333 | GRB 091126A | 07:59:24.77 | 65.9 | 16.0 | 41.7 | 0.7 | 53.6 | −80.0 | 5.9 | 53.6 | −80.0 | 5.9 | 82.7 | −16.1 | 4.8 | 82.1 | −17.0 | 4.9 |
| 091128285 | GRB 091128A | 06:50:34.65 | ⋯ | ⋯ | ⋯ | ⋯ | 135.9 | −11.9 | 18.0 | 131.3 | −3.0 | 5.1 | 128.1 | 4.4 | 1.4 | 128.1 | 1.9 | 1.4 |
| 091227294 | GRB 091227A | 07:03:13.39 | 294.5 | −23.9 | 23.7 | 0.4 | 305.0 | 10.0 | 15.8 | 305.4 | 9.9 | 9.8 | 298.3 | 1.9 | 4.2 | 297.0 | 3.4 | 3.3 |
| 091231206 | GRB 091231A | 04:56:33.49 | 300.2 | −22.7 | 80.4 | 0.2 | 196.3 | −64.1 | 15.0 | 187.5 | −54.3 | 8.0 | 196.9 | −57.9 | 2.6 | 195.6 | −54.0 | 2.1 |
| 100101988 | GRB 100101B | 23:42:15.19 | 142.2 | 18.9 | 46.7 | 0.2 | 65.2 | 17.1 | 19.6 | 65.2 | 17.1 | 19.6 | 83.0 | 9.2 | 12.9 | 81.8 | 19.5 | 23.7 |
| 100118100 | GRB 100118A | 02:23:33.70 | 313.8 | −15.7 | 57.4 | 0.1 | 71.5 | −81.3 | 14.4 | 71.4 | −81.3 | 11.4 | 359.6 | −60.6 | 13.3 | 359.2 | −63.7 | 3.0 |
| 100122616 | GRB 100122A | 14:47:37.32 | 135.9 | 21.5 | 65.8 | 0.2 | 49.0 | 0.2 | 20.7 | 76.7 | −11.0 | 4.2 | 88.7 | −6.8 | 2.1 | 78.5 | −2.1 | 1.6 |
| 100130777 | GRB 100130B | 18:38:35.47 | ⋯ | ⋯ | ⋯ | ⋯ | 144.7 | 31.2 | 16.0 | 69.0 | 25.1 | 17.8 | 78.0 | 19.0 | 5.6 | 79.7 | 23.2 | 2.5 |
| 100131730 | GRB 100131A | 17:30:57.68 | 132.4 | 22.5 | 16.4 | 0.3 | 117.0 | 26.2 | 3.9 | 117.0 | 26.2 | 3.9 | 131.2 | 24.8 | 1.3 | 117.5 | 13.8 | 1.5 |
| 100205490 | GRB 100205B | 11:45:38.26 | 115.9 | 18.2 | 41.0 | 0.6 | 126.6 | −33.4 | 21.3 | 134.7 | −20.0 | 19.2 | 133.3 | −21.4 | 8.6 | 132.6 | −22.2 | 7.1 |
| 100211440 | GRB 100211A | 10:33:35.17 | ⋯ | ⋯ | ⋯ | ⋯ | 120.9 | 31.8 | 5.4 | 120.9 | 31.8 | 5.4 | 138.4 | 30.2 | 3.8 | 133.3 | 29.0 | 2.3 |
| 100212550 | GRB 100212B | 13:11:45.47 | 117.1 | 19.3 | 21.6 | 0.3 | 138.7 | 33.9 | 7.3 | 131.4 | 34.1 | 6.6 | 136.0 | 33.8 | 2.0 | 134.3 | 32.3 | 1.9 |
| 100223110 | GRB 100223A | 02:38:09.31 | 125.4 | 23.8 | 25.0 | 0.1 | 105.9 | −7.5 | 5.3 | 105.9 | −7.5 | 5.3 | 94.2 | 3.0 | 6.0 | 102.1 | 5.6 | 7.7 |
| 100224112 | GRB 100224B | 02:40:55.48 | 306.0 | −19.3 | 38.2 | 0.2 | 269.8 | −28.6 | 15.3 | 266.2 | −9.5 | 6.2 | 271.2 | −20.8 | 1.9 | 270.0 | −18.7 | 2.2 |
| 100225580 | GRB 100225C | 13:55:31.35 | 307.5 | −19.2 | 21.3 | 0.3 | 312.8 | −0.5 | 19.0 | 312.8 | −0.5 | 4.8 | 317.0 | 6.3 | 4.1 | 311.7 | 3.4 | 1.2 |
| 100225703 | GRB 100225D | 16:52:18.12 | 127.9 | 19.2 | 26.1 | 0.3 | 94.5 | −61.6 | 9.3 | 137.2 | 43.9 | 12.1 | 142.0 | 26.6 | 5.4 | 153.2 | 30.9 | 7.5 |
| 100313288 | GRB 100313A | 06:54:23.23 | 145.7 | 15.9 | 74.4 | 0.2 | 157.0 | −58.7 | 7.7 | 166.8 | −58.8 | 6.5 | 173.4 | −54.4 | 3.7 | 169.3 | −52.4 | 3.0 |
| 100322045 | GRB 100322A | 01:05:09.65 | 337.1 | −12.2 | 45.7 | 0.1 | 24.7 | −10.2 | 6.8 | 28.7 | −5.8 | 4.4 | 22.1 | −12.0 | 1.0 | 21.0 | −13.4 | 1.0 |
| 100324172[a] | GRB 100324B | 04:07:36.49 | 39.67[a] | −19.29[a] | 0.0253[a] | 0.0431[a] | 326.0 | −37.1 | 3.6 | 61.3 | −12.2 | 4.1 | 25.5 | −16.7 | 1.2 | 44.7 | −17.3 | 1.0 |
| 100326402 | GRB 100326B | 09:38:20.05 | 343.3 | −9.9 | 28.2 | 0.3 | 303.0 | 12.1 | 23.3 | 308.3 | 13.3 | 18.8 | 312.8 | −16.5 | 9.0 | 310.8 | −4.6 | 2.1 |
| 100330309 | GRB 100330A | 07:24:51.73 | 168.8 | 7.8 | 32.8 | 0.2 | 213.8 | −1.5 | 11.6 | 208.3 | −0.7 | 7.5 | 195.4 | −0.1 | 3.2 | 202.8 | 1.8 | 2.9 |
| 100410740[a] | GRB 100410B | 17:45:46.67 | 351.92[a] | 62.90[a] | 0.0810[a] | 0.1473[a] | 293.9 | 25.6 | 25.5 | 319.3 | 37.4 | 11.8 | 4.0 | 61.8 | 2.9 | 3.1 | 60.8 | 1.6 |
| 100421917 | GRB 100421A | 21:59:48.40 | 24.8 | 9.1 | 49.6 | 0.4 | 324.6 | 18.0 | 23.2 | 345.4 | −19.4 | 14.3 | 343.9 | −19.3 | 4.9 | 344.9 | −21.1 | 3.2 |
| 100423244 | GRB 100423B | 05:51:25.76 | 27.3 | 10.3 | 89.4 | 0.1 | 120.6 | 5.2 | 31.9 | 120.9 | 0.0 | 7.9 | 120.6 | 4.5 | 2.6 | 119.7 | 5.8 | 1.6 |
| 100424876 | GRB 100424C | 21:01:52.60 | 30.5 | 11.7 | 36.9 | 0.2 | 39.5 | 32.8 | 22.4 | 39.5 | 32.8 | 22.4 | 44.9 | 30.8 | 14.7 | 17.6 | 46.5 | 2.5 |
| 100502356 | GRB 100502A | 08:33:02.95 | 45.9 | 18.0 | 76.6 | 0.1 | 133.3 | 16.8 | 23.8 | 129.6 | 19.9 | 7.9 | 125.7 | 27.1 | 2.8 | 127.7 | 23.9 | 1.6 |
| 100503554 | GRB 100503A | 13:18:03.89 | 228.5 | −18.8 | 79.2 | 0.1 | 145.7 | −14.1 | 22.8 | 146.8 | 5.4 | 7.6 | 144.5 | 5.6 | 2.7 | 149.3 | 5.5 | 1.9 |
| 100511035 | GRB 100511A | 00:49:56.24 | 64.3 | 23.4 | 51.9 | 0.1 | 107.8 | −0.9 | 8.1 | 108.3 | −8.1 | 4.7 | 111.5 | −0.9 | 1.3 | 110.5 | −3.2 | 1.0 |
| 100515467 | GRB 100515A | 11:13:09.04 | 322.1 | −16.7 | 61.4 | 0.1 | 279.1 | 30.0 | 4.6 | 279.1 | 30.0 | 5.4 | 271.1 | 24.3 | 2.1 | 276.4 | 26.7 | 2.3 |
| 100517154 | GRB 100517D | 03:42:08.06 | 255.9 | −25.2 | 25.0 | 0.2 | 236.9 | −12.9 | 8.1 | 236.9 | −12.9 | 8.1 | 242.1 | −12.0 | 4.7 | 246.5 | −9.2 | 4.1 |
| 100519204 | GRB 100519A | 04:53:22.71 | 79.4 | 25.6 | 75.1 | 0.5 | 191.0 | 58.8 | 12.8 | 182.0 | 56.5 | 8.1 | 191.2 | 56.8 | 2.2 | 197.7 | 57.9 | 1.5 |
| 100527795 | GRB 100527A | 19:04:37.25 | 272.8 | −25.5 | 54.1 | 0.5 | 212.5 | 40.2 | 26.9 | 214.2 | 26.8 | 12.3 | 229.5 | 17.0 | 3.1 | 232.4 | 14.5 | 4.9 |
| 100604287 | GRB 100604A | 06:53:34.82 | 281.0 | −24.1 | 51.0 | 0.3 | 271.1 | −79.5 | 14.3 | 240.0 | −72.6 | 6.6 | 255.5 | −75.5 | 2.7 | 245.5 | −69.9 | 2.3 |
| 100609783 | GRB 100609A | 18:48:11.33 | 153.7 | 12.3 | 57.2 | 0.7 | 100.0 | 33.8 | 28.2 | 95.4 | 36.5 | 13.4 | 89.9 | 42.0 | 5.4 | 98.1 | 36.1 | 1.5 |
| 100612545 | GRB 100612A | 13:04:21.66 | ⋯ | ⋯ | ⋯ | ⋯ | 61.6 | 10.1 | 7.4 | 61.6 | 10.1 | 7.4 | 68.7 | 18.7 | 5.8 | 65.2 | 17.5 | 4.2 |
| 100612726 | GRB 100612B | 17:26:06.13 | 288.2 | −21.5 | 66.0 | 0.3 | 351.9 | 1.1 | 7.4 | 346.5 | 2.6 | 4.1 | 352.1 | −3.1 | 1.2 | 352.1 | −3.0 | 1.1 |
| 100620119[a] | GRB 100620A | 02:51:29.12 | 88.99[a] | −50.72[a] | 0.1593[a] | 0.2504[a] | 79.6 | −52.6 | 8.4 | 79.7 | −52.5 | 8.2 | 91.4 | −51.8 | 3.6 | 93.0 | −52.3 | 2.1 |
| 100629801[a] | GRB 100629A | 19:14:03.36 | 227.62[a] | 29.55[a] | 0.0196[a] | 0.1297[a] | 212.2 | 33.1 | 4.7 | 212.2 | 33.1 | 4.7 | 221.7 | 27.1 | 6.5 | 222.2 | 30.0 | 2.7 |
| 100707032[a] | GRB 100707A | 00:46:38.99 | 357.60[a] | −6.96[a] | 0.1594[a] | 0.0679[a] | 52.9 | −47.4 | 3.4 | 3.2 | −10.6 | 3.6 | 351.3 | −7.3 | 1.0 | 351.3 | −7.5 | 1.0 |
| 100709602 | GRB 100709A | 14:27:32.99 | 169.1 | 5.6 | 23.7 | 0.2 | 143.6 | 3.1 | 13.6 | 155.3 | −8.1 | 12.0 | 152.5 | −3.8 | 8.7 | 142.3 | 20.7 | 4.2 |

**Notes.** All R.A., decl., Err, and width are in units of degree.

[a] These nine bursts have two intersecting arcs, in which the columns are as follows: R.A., decl., box side 1, box side 2.

(This table is available in its entirety in a machine-readable form.)

**Table 11**
Geometry-dependent Single-component Fits to Systematic Uncertainties on GBM Localizations

| | | Single-component Gaussian with Hemisphere Dependence | | | | | |
|---|---|---|---|---|---|---|---|
| Type | Hemisphere | Number GRB | | Peak | Error | log$_{10}$ | log$_{10}$ |
| | | Point | Annuli | (°) | (°) | Likelihood | Odds Factor |
| Ground-Auto | All-sky | 208 | 100 | 6.62 | 0.29 | 155.2 | 154.3 |
| Ground-Auto | +X | 208 | 100 | 6.95 | 0.42 | | |
| | −X | | | 6.25 | 0.41 | 155.5 | 154.0 |
| Ground-Auto | +Y | 208 | 100 | 7.02 | 0.44 | | |
| | −Y | | | 6.21 | 0.39 | 155.7 | 154.2 |
| Ground-Auto | +Z | 208 | 100 | 6.48 | 0.33 | | |
| | −Z | | | 7.10 | 0.64 | 155.4 | 154.0 |
| Ground-Auto | ±X | 208 | 100 | 7.27 | 0.45 | | |
| | ±Y | | | 5.96 | 0.38 | 156.3 | 154.8 |
| HitL 4.14g | All-sky | 212 | 100 | 5.15 | 0.22 | 224.6 | 223.6 |
| HitL 4.14g | +X | 212 | 100 | 5.19 | 0.31 | | |
| | −X | | | 5.06 | 0.32 | 224.6 | 222.9 |
| HitL 4.14g | +Y | 212 | 100 | 5.26 | 0.32 | | |
| | −Y | | | 5.02 | 0.31 | 224.7 | 222.9 |
| HitL 4.14g | +Z | 212 | 100 | 4.98 | 0.24 | | |
| | −Z | | | 5.68 | 0.53 | 225.0 | 223.3 |
| HitL 4.14g | ±X | 212 | 100 | 5.41 | 0.35 | | |
| | ±Y | | | 4.93 | 0.29 | 224.9 | 223.2 |
| HitL 4.13 | All-sky | 211 | 100 | 6.23 | 0.26 | 192.6 | 191.7 |
| HitL 4.13 | +X | 211 | 100 | 6.04 | 0.35 | | |
| | −X | | | 6.41 | 0.37 | 192.7 | 191.1 |
| HitL 4.13 | +Y | 211 | 100 | 6.84 | 0.39 | | |
| | −Y | | | 5.57 | 0.34 | 194.0 | 192.4 |
| HitL 4.13 | +Z | 211 | 100 | 5.90 | 0.27 | | |
| | −Z | | | 7.57 | 0.66 | 194.0 | 192.5 |
| HitL 4.13 | ±X | 211 | 100 | 6.74 | 0.39 | | |
| | ±Y | | | 5.75 | 0.33 | 193.5 | 191.8 |

**Table 12**
Hemisphere-dependent Core-plus-tail Fits to Systematic Uncertainties on GBM Localizations

| | | Core + Tail (2 Gaussians) with Hemisphere Dependence | | | | | | | | | |
|---|---|---|---|---|---|---|---|---|---|---|---|
| Type | Hemisphere | Number GRB | | Core | Error | Core | Error | Tail | Error | log$_{10}$ | log$_{10}$ |
| | | Point | Annuli | (°) | (°) | (%) | (%) | (°) | (°) | Likelihood | Odds Factor |
| Ground-Auto | All-sky | 208 | 100 | 3.72 | 0.34 | 80.4 | 5.3 | 13.7 | 1.7 | 174.1 | 171.8 |
| Ground-Auto | +X | 208 | 100 | 3.95 | 0.52 | 82.2 | 7.7 | 14.1 | 2.6 | | |
| | −X | | | 3.55 | 0.44 | 79.3 | 7.4 | 13.4 | 2.5 | 174.1 | 170.6 |
| Ground-Auto | +Y | 208 | 100 | 3.80 | 0.44 | 77.7 | 7.1 | 14.5 | 2.3 | | |
| | −Y | | | 3.58 | 0.56 | 82.6 | 9.0 | 12.3 | 2.6 | 174.5 | 171.0 |
| Ground-Auto | | | The Z-hemisphere model failed to produce values for the −Z parameters | | | | | | | | |
| HitL 4.14g | All-sky | 212 | 100 | 3.71 | 0.24 | 90.0 | 3.5 | 14.3 | 2.5 | 241.3 | 238.9 |
| HitL 4.14g | +X | 212 | 100 | 3.76 | 0.32 | 90.7 | 4.8 | 13.8 | 3.6 | | |
| | −X | | | 3.68 | 0.33 | 89.7 | 5.0 | 15.4 | 3.7 | 241.3 | 237.4 |
| HitL 4.14g | +Y | 212 | 100 | 3.89 | 0.33 | 89.3 | 5.2 | 13.9 | 3.6 | | |
| | −Y | | | 3.53 | 0.30 | 90.5 | 4.5 | 14.9 | 3.7 | 241.5 | 237.5 |
| HitL 4.14g | +Z | 212 | 100 | 3.43 | 0.27 | 88.3 | 4.7 | 12.7 | 2.4 | | |
| | −Z | | | 4.36 | 0.52 | 90.4 | 6.0 | 16.2 | 8.2 | 242.5 | 238.5 |
| HitL 4.13 | All-sky | 211 | 100 | 3.57 | 0.32 | 79.8 | 5.3 | 12.7 | 1.5 | 213.5 | 211.1 |
| HitL 4.13 | +X | 211 | 100 | 3.48 | 0.39 | 83.1 | 6.3 | 12.9 | 2.2 | | |
| | −X | | | 3.64 | 0.52 | 75.9 | 8.8 | 12.3 | 2.2 | 213.8 | 210.1 |
| HitL 4.13 | +Y | 211 | 100 | 3.63 | 0.48 | 77.1 | 7.6 | 13.1 | 2.0 | | |
| | −Y | | | 3.50 | 0.42 | 81.9 | 7.8 | 11.8 | 2.4 | 213.8 | 210.1 |
| HitL 4.13 | +Z | 211 | 100 | 3.40 | 0.37 | 79.6 | 6.4 | 11.4 | 1.5 | | |
| | −Z | | | 3.94 | 0.61 | 76.0 | 9.2 | 15.4 | 3.5 | 214.4 | 210.8 |

the slight differences in parameter values, with the exception of HitL 4.14g and the $Z$ hemisphere division that appears promising when a larger sample becomes available.

## REFERENCES

Aasi, J., Abadie, J., Abbott, B. P., et al. 2013, arXiv:1304.0670
Abadie, J., Abbott, B. P., Abbott, R., et al. 2012, ApJ, 760, 12
Abadie, J., Abbott, R., Abernathy, M., et al. 2010, CQGra, 27, 17
Abdo, A. A., Ackermann, M., Ajello, M., et al. 2009, ApJL, 706, L138
Ackermann, M., Ajello, M., Asano, K., et al. 2013, ApJS, 209, 11
Atwood, W. S., Abdo, A. A., Ackermann, M., et al. 2009, ApJ, 697, 1071
Band, D. L., Matteson, J., Ford, L., et al. 1993, ApJ, 413, 281
Bissaldi, E., von Kienlin, A., Lichti, G., et al. 2009, ExA, 24, 47
Briggs, M. S., Connaughton, V., Meegan, C. A., et al. 2009, in AIP Conf. Proc. 1133, GAMMA-RAY BURST: Sixth Huntsville Symposium, ed. C. Meegan, C. Gehrels, & N. Kouveliotou (Melville, NY: AIP), 40
Briggs, M. S., Pendleton, G. F., Kippen, R. M., et al. 1999, ApJS, 122, 503
Bromberg, O., Nakar, E., Piran, T., & Sari, R. 2013, ApJ, 764, 179
Connaughton, V., Pelassa, V., Briggs, M. S., et al. 2013, in EAS Publications Series, 61, Gamma-ray Bursts: 15 years of GRB Afterglows, ed. A. J. Castro-Tirado, J.. Gorosabel, & I. H. Park (Cedex: EDP Sciences), 657
de Ugarte Postigo, A., Xu, D., Malesani, D., et al. 2013, GCN Circular, 15187
Fisher, N. I., Lewis, T., & Embleton, J. J. 1987, Statistical Analysis of Spherical Data (Cambridge: Cambridge Univ. Press)
Goldstein, A. M., Burgess, J. M., Preece, R. D., et al. 2012, ApJS, 199, 19

Graziani, C., & Lamb, D. Q. 1996, in AIP Conf. Proc. 384, ed. Kouveliotou, Briggs & Fishman (Melville, NY: AIP), 382
Gruber, D., Goldstein, A., Weller von Ahlefeld, V., et al. 2014, ApJS, 211, 12
Hurley, K., Pal'shin, V. D., Aptekar, R. L., et al. 2013, ApJS, 207, 39
Kippen, R. M., Hoover, A. S., Wallace, M. S., et al. 2007, in AIP Conf.Proc. 921, The First Glast Symposium, ed. S. Ritz & P. Michelson (Melville, NY: AIP), 590
Leloudas, G., Fynbo, J. P. U., Schulze, S., et al. 2013, GCN Circular, 14983
Levan, A. J., Cenko, S. B., Perley, D. A., & Tanvir, N. R. 2013, GCN Circular, 14455
Loredo, T. J. 1990, in Maximum Entropy and Bayesian Methods, ed. P. F. Fougère (Dordrecht: Kluwer), 81
Meegan, C., Lichti, G., Bhat, P. N., et al. 2009, ApJ, 702, 791
Paciesas, W. S., Meegan, C. A., von Kienlin, A., et al. 2012, ApJS, 199, 18
Pal'shin, V. D., Hurley, K., Svinkin, D. S., et al. 2013, ApJS, 207, 38
Pandey, S., Swenson, C. A., Perley, D. A., et al. 2010, ApJ, 714, 799
Pendleton, G. N., Briggs, M. S., Kippen, R. M., et al. 1999, ApJ, 512, 362
Sánchez-Ramírez, R., Gorosabel, J., Castro-Tirado, A. J., et al. 2013, GCN Circular, 14685
Singer, L., Cenko, S. B., Kasliwal, M. M., et al. 2013, ApJL, 776, 34
Singer, L., Kasliwal, M. M., Cenko, S. B., et al. 2015, ApJ, submitted (arXiv:1501.00495)
Sivia, D. S. 1996, Data Analysis: A Bayesian Tutorial (Oxford, UK: Oxford Univ. Press)
Soderberg, A. M., Chakraborti, S., Pignata, G., et al. 2010, Natur, 463, 513
von Kienlin, A., Meegan, C. A., Paciesas, W. S., et al. 2014, ApJS, 211, 13